

## ABSTRACT

# CONFORMATIONAL STUDIES OF HUMAN APOLIPOPROTEIN E3 AS REVEALED BY FLUORESCENCE POLARIZATION AND MASS SPECTROMETRY

By

Roy Valentine Hernandez

January 2015

Apolipoprotein E3 (apoE3) is an important anti-atherogenic protein that helps maintain cholesterol levels in the brain and plasma. It is responsible for binding and cellular uptake of plasma lipoproteins via the low-density lipoprotein receptor family of proteins. Fluorescence intensity measurements demonstrate environmentally sensitive fluorescent probes undergoing bathochromic shift due to an increase in polar environment. Polarization studies indicate that the unfolding is likely initiated at the C-terminal end of the protein, the CT domain unfolds prior to NT domain, and that the NT domain forms a highly stable helix bundle. Hydrogen deuterium exchange mass spectrometry analysis revealed that the amide backbone of the NT domain underwent helix specific exchange where helix 1 and 2 have higher percent deuterium compared to helix 3 and 4. In contrast, the CT domain revealed significantly higher HDX rates. Our studies suggest that the two domains of apoE may undergo independent conformational reorganization.



CONFORMATIONAL STUDIES OF HUMAN APOLIPOPROTEIN E3 AS  
REVEALED BY FLUORESCENCE POLARIZATION AND MASS  
SPECTROMETRY

A THESIS

Presented to the Department of Chemistry and Biochemistry  
California State University Long Beach

In Partial Fulfillment  
of the Requirement for the Degree  
Master of Science in Biochemistry

Committee Members:

Vasanthi Narayanaswami, Ph.D. (Chair)  
Paul M.M. Weers, Ph.D.  
Douglas McAbee, Ph.D.

College Designee:

Christopher Brazier, Ph.D.

By Roy Valentine Hernandez

B.S., B.A., 2010, California State University San Bernardino, San Bernardino

January 2015

UMI Number: 1584727

All rights reserved

INFORMATION TO ALL USERS

The quality of this reproduction is dependent upon the quality of the copy submitted.

In the unlikely event that the author did not send a complete manuscript and there are missing pages, these will be noted. Also, if material had to be removed, a note will indicate the deletion.



UMI 1584727

Published by ProQuest LLC (2015). Copyright in the Dissertation held by the Author.

Microform Edition © ProQuest LLC.

All rights reserved. This work is protected against unauthorized copying under Title 17, United States Code



ProQuest LLC.  
789 East Eisenhower Parkway  
P.O. Box 1346  
Ann Arbor, MI 48106 - 1346

## ACKNOWLEDGMENTS

I express my deep appreciation and thanks to Vasanthi Narayanaswami for being my mentor and friend throughout these great years as an M.S. student. My entire lab that helped me in realizing this goal and without them, it would have been impossible to achieve this milestone of my life. I am grateful to my thesis committee members Dr. Paul Weers and Dr. Douglas McAbee for their encouragement, support and time and efforts, in reviewing this manuscript. I would also like to give my thanks to Dr. Claudia S. Maier for our collaboration on the HDX/MS component of this research as well as Sasidhar Nirudodhi for teaching HDX/MS experiments. I am thankful to Dr. Jason Schwans for helping me analyze HDX/MS data for this manuscript. I express my gratitude to Dr. Cohlberg, Dr. Klig, and Dr. Eldon for helping along this journey and helping me achieve my goals. The last person to thank is my brother Albert Hernandez for helping me to be a stronger person in life. This work was supported by funding from NIH/NHLBI # HL096365 and NIH/NIGMS #GM105561 (V.N) and McAbee Overstreet Research Award by the Department of Chemistry and Biochemistry, CSULB.

## TABLE OF CONTENTS

	Page
ACKNOWLEDGMENTS .....	iii
LIST OF TABLES .....	vii
LIST OF FIGURES .....	viii
LIST OF ABBREVIATIONS.....	x
CHAPTER	
1. INTRODUCTION .....	1
Lipoprotein Biology.....	1
Physiological Role of ApoE.....	2
ApoE and Domain Structure.....	3
ApoE: A Polymorphic Protein .....	6
Defective LDLr Binding in ApoE2.....	7
ApoE4: a Risk Factor for CVD and AD .....	8
X-Ray Crystal Structure of ApoE3 NT Domain.....	9
NMR Solution Structure of ApoE3(1-183) and ApoE3(1-299) .....	10
Structure of ApoE3 from Mass Spectrometric Studies.....	12
Lipid-Associated Conformation of ApoE3 .....	13
Gap in Knowledge and Questions Left Unanswered.....	15
NT and CT Gap in Knowledge.....	15
Hypothesis and Objectives.....	15
Objective 1: Assess Chemical Denaturant-Induced Change in Mobility of Probes Introduced by Site-Specific Fluorescence Labeling to Monitor Defined Sites .....	16
Objective 2: Assess the Solvent Accessibility and Extent of Deuterium Incorporation in the Isolated Domains of ApoE3 by Mass Spectrometry .....	16
2. MATERIALS AND METHODS.....	17
HDX/MS Experiments.....	17
Design of Single Cysteine Constructs.....	18

CHAPTER	Page
Site-Directed Mutagenesis .....	19
Expression, Isolation, and Purification of ApoE Constructs .....	19
IAEDANS Labeling.....	20
Circular Dichroism (CD) Spectroscopy.....	20
GdnHCl-Induced Unfolding.....	21
Fluorescence Spectroscopy.....	23
Fluorescence Polarization.....	23
Statistical Analysis.....	24
 3. RESULTS .....	 25
Objective 1: Determine Order of Helical Unfolding of the ApoE NT and CT Domains .....	 25
Design of Single Cys Constructs .....	28
SDS-PAGE Analysis of ApoE NT Variants.....	30
IAEDANS Labeling and Stoichiometry of Labeling.....	33
Secondary Structural Analysis of AEDANS-Labeled Single Cys ApoEC 112S NT and ApoE CT Variants .....	 36
Chemical Denaturation of AEDANS-Labeled single Cys ApoEC112S NT and CT Variants.....	 37
GdnHCl-Induced Denaturation of AEDANS-Labeled ApoE Variants Followed by CD.....	 38
GdnHCl-Induced Denaturation of AEDANS-Labeled ApoE Variants Followed by Changes in Fluorescence Emission Intensity and $\lambda_{Max}$ .....	 42
GdnHCl-Induced Denaturation of AEDANS-Labeled ApoE Variants Followed by Changes in FP .....	 51
Unfolding of AEDANS-Labeled Single Cys ApoEC112S(1-191) NT Domain Variants .....	 52
Unfolding of AEDANS-Labeled Single Cys ApoE(201-299) CT Domain Variants.....	 54
Objective 2: Determine Backbone Dynamics and Solvent Accessibility with HDX Coupled to MS on ApoE3 NT and ApoE CT Domains..	 57
HDX of ApoE3(1-191) NT Domain.....	57
D Uptake Plots for ApoE3(1-191) .....	60
Protection Plot of ApoE3(1-191) Peptide Fragments .....	65
HDX of ApoE(201-299) CT Domain.....	67
D Uptake Plots for ApoE(201-299) .....	68
Protection Plot of ApoE(201-299) Peptide Fragments .....	71

CHAPTER	Page
4. DISCUSSION .....	73
Fluorescent Tagging of NT and CT Domain.....	78
Unfolding of ApoE3 NT Domain .....	80
Unfolding of ApoE CT Domain.....	82
Accessibility of Amide Backbone of ApoE3 NT from HDX/MS.....	83
ApoE CT HDX/MS.....	87
Summary and Perspectives.....	89
 APPENDIX: LIST OF RESEARCH PUBLICATIONS AND PRESENTATIONS..	 99
 BIBLIOGRAPHY.....	 102

## LIST OF TABLES

TABLE	Page
1. ApoE NT and CT Single Cys Constructs .....	29
2. Calculated and Measured Molecular Masses of Single Cys apoE Variants.....	30
3. Sample Calculation for Stoichiometry of Labeling.....	31
4. Stoichiometry of Labeling of AEDANS Labeled Single Cys apoE Variants...	36
5. $\alpha$ -helical Content of AEDANS-Labeled ApoE NT and CT Variants .....	37
6. Midpoint of Denaturation and Change in Gibbs Free Energy of GdnHCl-Induced Unfolding of AEDANS-Labeled ApoE NT and CT Constructs Measured by CD Spectroscopy.....	42
7. Denaturation of AEDANS-Labeled ApoE Variants Followed by Changes in Fluorescence Intensity.....	48
8. Changes $\lambda_{max}$ by GdnHCl in AEDANS-Labeled ApoE NT and CT Variants ..	48
9. Midpoint of Denaturation and Change in $\Delta G$ for GdnHCl-Induced Unfolding of AEDANS-Labeled ApoE NT Constructs Measured by FP Spectroscopy.....	54
10. Midpoint of Denaturation and Change in $\Delta G$ for GdnHCl-Induced Unfolding of AEDANS-Labeled ApoE CT Constructs Measured by FP Spectroscopy .....	56
11. Peptides Derived from Peptic Digestion of ApoE3(1-191).....	59
12. Kinetic Data and Pf for HDX of ApoE3(1-191) Peptides .....	64
13. Peptides Derived from Peptic Digestion of ApoE(201-299).....	68
14. Kinetic Data and Protection Factor for ApoE(201-299) Peptides .....	70
15. Free Energy of Unfolding of Exchangeable Apolipoproteins .....	74

TABLE	Page
16. Buried H-bonds, Salt Bridges, and Leucine Zipper Residues found in ApoE3 (1-183) NT Domain from PDB 2KC3.....	75
17. D Uptake at Each Time Point ApoE (1-191).....	92
18. D Uptake at Each Time Point ApoE CT (201-299) .....	95

## LIST OF FIGURES

FIGURE	Page
1. Amino acid sequence of apoE3 showing the helix boundaries based on NMR structure of apoE3(1-299) PDB 2L7B .....	4
2. NMR structure using coordinates from mutant monomeric apoE3 (1-299) PDB 2L7B .....	10
3. Free energy of stabilization ( $\Delta G$ ) as a function of [GdnHCl].....	22
4. Contact map of apoE3 NT domain showing residue distances between helices .....	27
5. Structure guided design for single Cys constructs of apoE3 NT domain .....	29
6. SDS-PAGE of unlabeled single cysteine apoE NT and CT variants.....	32
7. Chemical reaction of IAEDANS with free sulfhydryls group on proteins ...	33
8. SDS-PAGE of AEDANS-labeled apoE NT and CT variants.....	34
9. Far-UV CD spectra of AEDANS labeled single Cys apoEC112S NT variants and CT variants .....	39
10. GdnHCl-induced unfolding of AEDANS labeled apoE NT variants as measured by CD spectroscopy .....	41
11. GdnHCl-induced unfolding of AEDANS labeled apoE CT variants as measured by CD spectroscopy .....	43
12. Fluorescence emission spectra of AEDANS-labeled apoE NT and CT variants .....	46
13. Fluorescence emission spectra of AEDANS-labeled apoEC112S/A29C at various GdnHCl concentrations .....	47
14. GdnHCl-induced changes in fluorescence emission characteristics of AEDANS-labeled apoE NT variants .....	49

FIGURE	Page
15. GdnHCl-induced changes in fluorescence emission characteristics of AEDANS-labeled apoE CT variants .....	50
16. GdnHCl-induced denaturation of AEDANS-labeled apoE NT variants as monitored by change in FP values .....	53
17. GdnHCl-induced denaturation of AEDANS-labeled apoE CT variants as monitored by change in FP values.....	56
18. Peptide fragments obtained following on-line pepsin digestion of apoE3 (1-191) at pD 2.5.....	58
19. Uptake plots of apoE3(1-191) peptic digest peptides region 1-78.....	61
20. Uptake plots of apoE3(1-191) peptic digest peptides region 79-137.....	62
21. Uptake plots of apoE3(1-191) peptic digest peptides region 133-187.....	63
22. Protection plot of apoE3(1-191) peptide fragments.....	65
23. % D incorporation superimposed on the NMR structure of apoE3(1-183) (PDB 2KC3).....	66
24. Peptide fragments obtained following on-line pepsin digestion of apoE (201-299) at pD 2.5.....	67
25. Uptake plots of apoE3(201-299) peptic digest peptides region 206-272.....	69
26. Uptake plots of apoE3(201-299) peptic digest peptides region 265-279.....	70
27. Protection plot of apoE(201-299).....	72
28. ApoE3 (1-191) ordered helix unfolding models .....	77
29. Leu zipper and H-bonds in H1/H2 and H3/H4 of apoE3(1-191).....	84
30. Buried hydrophilic residues in apoE3(1-191).....	86
31. 80's loop is the hinge for helix bundle opening of ApoE3 (1-191) .....	86
32. Wild type Human ApoE CT (201-299) bearing a His-tag.....	88

33. % D incorporation on CT helices C1, C2 and C3 superimposed on the NMR structure of apoE3(1-299) (PDB 2L7B) .....	88
---	----

## LIST OF ABBREVIATIONS

AD	Alzheimer's Disease
CD	Circular Dichroism
CNS	Central Nervous System
CT	C-Terminal
CVD	Cardiovascular Diseases
CM	Chylomicron
FP	Fluorescent Polarization
FI	Fluorescent Intensity
$\Delta G$	Free Energy of unfolding
GdnHCl	Guanidine Hydrochloride
HDL	High Density Lipoprotein
HDX	Hydrogen Deuterium Exchange
IDL	Intermediate Density Lipoprotein
IPTG	Isopropyl-P- $\beta$ -thiogalactopyranoside
LDL	Low Density Lipoprotein
LDLr	LDL Receptor
MS	Mass Spectrometry
NT	N-Terminal
NMR	Nuclear Magnetic Resonance

PAGE	Polyacrylamide Gel Electrophoresis
PDB 1NFN	X-ray apoE(1-183) NT domain
PDB 2L7B	NMR apoE(1-299) full length monomer
PDB 2KC3	NMR apoE3(1-191) NT domain
PBS	Phosphate Buffered Saline
SDS	Sodium dodecyl sulphate
TCEP	Tris Carboxy Ethyl Phosphine
TG	Triglycerides
VLDL	Very Low Density Lipoprotein
WT	Wild-Type

## CHAPTER 1

### INTRODUCTION

#### Lipoprotein Biology

Lipoproteins play critical roles for transporting hydrophobic materials such as triglycerides (TG), cholesteryl ester (CE), cholesterol, amphipathic lipids, and other lipids in the blood and central nervous system (CNS). They are an amalgamation of lipids and proteins that serve as water soluble complexes to transport hydrophobic material (1). There are five major classes of lipoproteins that are classified depending on the size and density (depending on the components of lipid and protein): Chylomicron (CM), very low-density lipoproteins (VLDL), intermediate density lipoproteins (IDL), low-density lipoproteins (LDL), and high-density lipoproteins (HDL). Synthesis of lipoproteins can occur in the liver and intestines and can be assembled at the cell membranes from cellular lipids and apolipoproteins. Circulation in blood enables lipoproteins to travel to peripheral tissues and be taken up via receptor-mediated endocytosis, an important mechanism to deliver cholesterol to cells (2). Cholesterol is an essential structural component of cell membranes that helps maintain proper membrane permeability and fluidity. It serves as a precursor for biosynthesis of hormones, bile salt, and vitamins. In the CNS cholesterol is also required for neuronal development, maintenance of synapse connections, and at sites where synaptogenesis occurs which require constant rebuilding of membranes during vesicle budding and fusion (3).

## Physiological Role of ApoE

The field of lipoprotein metabolism seeks to explore research questions that span major biological processes involving cholesterol such as transportation to peripheral tissues for the synthesis of hormones and incorporation into membranes for maintaining fluidity. Arteriosclerosis, a disease of the vascular wall begins with deposition of lipids into the walls of large blood vessels in patients with elevated cholesterol levels. Thickening of arterial walls occurs over time and is the primary factor for heart attack incidents and accounts for over half of deaths in the US (4). A family of proteins that play a crucial role in the metabolism of lipoprotein particles is the amphipathic class of proteins named apolipoproteins. A major player in this class of proteins is apolipoprotein E (apoE), which is involved in cholesterol homeostasis; it is an exchangeable apolipoprotein that can exist in lipid-free form or lipid bound conformation (5). ApoE plays a significant role in cholesterol distribution from liver to peripheral tissues (forward cholesterol transport) and retrograde transportation of cholesterol from macrophages to the liver (reverse cholesterol transport) the latter playing a particularly special role in atherosclerosis (6). This protein has been implicated in cardiovascular (CVD) disease and neurobiological diseases in the CNS (7). ApoE maintains plasma and cellular cholesterol levels by: (i) serving as a ligand for the low-density lipoprotein receptor (LDLr) family of proteins, and, (ii) promoting cholesterol efflux from macrophages during atherosclerosis.

ApoE is rich in basic residues (Arg and Lys), which are especially predominant in the receptor binding region; it was therefore initially dubbed as an “Arg-rich protein” (8). It is found to be associated with CM remnants, VLDL, IDL and a subclass HDL<sub>3</sub> during

atherogenesis (9). It serves as a ligand for the LDLr and helps in clearing lipoproteins from the plasma thereby lowering cholesterol levels (9). The role of apoE in lipoprotein metabolism is illustrated in apoE-deficient patients who display Type III hyperlipoproteinemia characterized by high levels of TG in blood (>300mg/dL), a major risk for CVD. Severe consequences occur in patients whose levels deviate from normal; for example, Type III hyperlipoproteinemia is characterized by a 2x increase in plasma lipoproteins, while individuals with Type V hyperlipoproteinemia display high plasma levels of CM and VLDL, with TG levels elevated to ~1000 mg/dL. Studies in transgenic mice have also demonstrated the importance of apoE in cholesterol and TG metabolism: apoE-null mice exhibit massive accumulation of remnant lipoproteins and develop severe atherosclerosis (10). On the other hand, transgenic mice over expressing human apoE manifest marked resistance to diet-induced hypercholesterolemia (11). Taken together, these early studies exemplify the importance of apoE in regulating plasma cholesterol homeostasis and lipoprotein metabolism.

In the CNS, apoE is the most commonly and widely studied apolipoprotein, and is the most abundant apolipoprotein found in the brain and cerebrospinal fluid. It is synthesized and secreted by astrocytes (12) and by neurons under select conditions (13). It plays an important role in the regulation of synapse formation, plasticity and neuronal repair (2).

### ApoE and Domain Structure

ApoE gene is located at position 19q13.2 on chromosome 19. Its sequence was determined from the cDNA that was obtained from the mRNA product (14). Native apoE is 299 amino acids in length with a mass of 34.2 kDa (Figure 1), the molecular

mass represents the mass in the absence glycosylation at position 194 (15). In the lipid-bound but not in lipid-free state it has the ability to bind to the LDLr. Early studies of protein structure elucidation took advantage of proteolytic susceptibility of apoE to understand its fragmentation patterns (5, 16). Proteolysis studies revealed that apoE is composed of two domains: a 22 kDa N-terminal (NT) domain (residues 1-191) that houses the LDLr-binding site

*MHHHHHGLVPRGSIDPKVEQAVETEPEPELROQTEWQSGQRWELALGRFWDY*  
*LRWVQTLSEQVQEELLSSQVTQELRALMDETMKELKAYKSELEEQLTPVAEETR*  
*ARLSKELQAAQARLGADMEDVCGRLVQYRGEVQAMLGQSTEELRVRLASHLR*  
*KLRKRLRDADDLQKRLAVYQAGAREGAERGLSAIRERLGPLVEQGRVRAATV*  
*GSLAQPLQERAQAWGERLRARMEEMGSRTRDRLDEVKEQVAEVRAKLEEQA*  
*QQIRLQAEAFQARLKSWFEPLVEDMQRQWAGLVEKVQAAVGTSAAPVPSDNH*

FIGURE 1. Amino acid sequence of apoE3 showing the helix boundaries based on NMR structure of apoE3(1-299) PDB 2L7B. The His-tag sequence is italicized. Residues in helices N1(V6-E9), N2 (P12-S22), H1 (W26-V40), H2 (Q55-E79), H3 (T89-M125), and H4 (E131-A164) in the NT domain are underlined. Residues in helices C1 (W210-S223), C2 (V236-E266) and C3 (D271-W276) in the CT domain are double underlined.

(17) and a 10 kDa C-terminal (CT) domain (residues 201-299) that houses high affinity lipid binding sites; the latter also bears the oligomerization sites (18). Each domain can be expressed individually with retention of their respective function. The region connecting the two domains is a protease sensitive segment; its flexibility is thought to facilitate domain-domain interaction although its physiological significance or function is not known at this time. Upon lipid interaction, apoE undergoes a large conformational change about the hinge region, involving unfurling of the CT-domain away from the NT domain and breaking domain-domain interactions. Furthermore, early protein

denaturation studies (19, 19, 20) involving guanidine hydrochloride (GdnHCl), urea and heat monitored apoE unfolding by circular dichroism (CD) spectroscopy; they indicate that the NT and CT domains unfold independent of each other and have distinct roles in binding to lipoprotein particles. The NT domain unfolds with a midpoint of denaturation  $[GdnHCl]_{1/2}$  of  $\sim 2.4$  M GdnHCl ( $\Delta G = 10$  kcal/mol) and the CT unfolds at  $\sim 0.7$  M GdnHCl ( $\Delta G = 4.0$  kcal/mol) showing that these two domains have overall different global stabilities (21).

The NT domain is folded into a four helix-bundle composed of long amphipathic  $\alpha$ -helices (H1, H2, H3 and H4) in an up-and-down topology (22). Sedimentation equilibrium and size exclusion chromatography studies reveal that the NT domain exists as a monomeric unit in solution (23, 24). The sites responsible for LDLr binding are located around residues 130-160 on helix H4. The LDLr binding ability is active upon lipid association of the NT domain. In contrast to the CT domain, which has a high affinity for lipids, the NT domain has a relatively lower affinity. This difference in affinity is likely a key factor in regulating lipoprotein metabolism and in binding to hydrophobic surfaces such as lipoprotein surfaces (25). It is believed that the apolipoprotein stability is inversely related to lipid binding affinity (26): thus the NT domain with its high protein stability ( $[GdnHCl]_{1/2}$  of 2.4 M and  $\Delta G$  of 10 kcal/mol), displays a lower lipid affinity, while the CT domain with its lower protein stability displays a high lipid binding affinity. This correlation has been reported with other apolipoproteins as well such as apoAI and insect apolipophorin III (27, 28).

*In silico* secondary structural studies, biochemical truncation analysis, mutational and biophysical studies have all contributed to our current understanding of the CT

domain. ApoE exists primarily as a tetramer in solution with the oligomerization mediated by residues in the CT domain (5, 16, 29). The oligomerization mediated by the CT domain is noted at concentrations ranging from 50  $\mu\text{g/mL}$  up to 9  $\text{mg/ml}$  (5). Computer-based sequence algorithms predict that the CT domain exists as a series of amphipathic  $\alpha$ -helices. Sedimentation equilibrium, size exclusion chromatography and apoE C-terminal truncation experiments have suggested the terminal helix (266-299) to be involved in self-association and oligomerization in the absence of lipid (18, 30). Mutation studies on the CT domain showed that when residues F257, W264, V269, L279 and V287 were replaced with smaller or polar residues, no oligomerization or cross-linking occurred (31). Recent findings with CD and steady-state fluorescence spectroscopy suggest that the entire CT domain (not just the terminal helix) makes extensive intermolecular helix-helix contacts with neighboring apoE molecules in lipid-free state (32). There are several unanswered mechanistic questions regarding the CT domain. While it is generally acknowledged that the helix-helix interactions are replaced by helix-lipid interactions during lipid association, details regarding the mechanism of this transition, initiation of lipid binding and the steps involved in the dissociation are not understood. More details at the molecular level must therefore be gathered to fully understand this lipid-induced shift and conformational change.

#### ApoE: A Polymorphic Protein

ApoE was first discovered on VLDL in human plasma in 1971; it was later found on several other lipoprotein particles (1, 33). In the 1980s major isoforms of apoE were categorized in terms of their genetic allelic combination found in the human population. Alpha and beta subclasses were named based on allelic pairs for homozygosity or

heterozygosity which was derived based on data from population genetics studies (34). Three major alleles of apoE were discovered: *APOE*  $\epsilon$ 2, *APOE*  $\epsilon$ 3, *APOE*  $\epsilon$ 4, which were found to be part of a stable gene frequency in the population. About 7.3% of the population have the *APOE*  $\epsilon$ 2 allele, 78.3% have *APOE*  $\epsilon$ 3, and 14.3% have *APOE*  $\epsilon$ 4 (1). Of the resulting protein isoforms, apoE3 is considered anti-atherogenic, while apoE2 and apoE4 contribute to diseases of lipid metabolism and CVD due to their specific structure and physiochemical properties (23, 35–38). In addition, individuals homozygous for *APOE*  $\epsilon$ 4 are at a 25-fold higher risk to develop Alzheimer's disease (AD) than those bearing *APOE*  $\epsilon$ 3 (12).

The three isoforms differ in the amino acid at positions 112 and 158. ApoE3, the most common isoform, has Cys112 and Arg158; apoE2 has Cys112 and Cys158, while apoE4 has Arg112 and Arg158. The single amino acid substitution at position 158 to Cys in apoE2 results in impaired binding to the LDLr (39). On the other hand, substitution of Cys at position 112 with Arg in apoE4 isoform appears to lead to a salt bridge interaction (termed domain-domain interaction) between Arg61 in the NT domain and Glu255 in the CT domain (40, 41). Thus, a single amino acid change appears to have major consequences in overall physiological function and disease pathology. Understanding how a subtle one amino acid change could influence cholesterol imbalance is currently an active field of research.

#### Defective LDLr Binding in apoE2

Intermolecular salt-bridges, hydrophobic forces, and hydrogen bonding network influence the overall tertiary structure of apoE. Specific inter-helical residue interactions as well as intra-helical interactions are a significant source for protein stabilization in

several instances; they also contribute to protein specific function in a cell compartment specific manner. The latter aspect is illustrated in apoE2, which displays defective LDLr binding. The receptor binding interaction is mediated by several basic residues located in helix H4 and its vicinity. In apoE3, Arg158 forms a salt bridge with Asp154 one helix turn away. However, in apoE2, which bears Cys158, the Arg158-Asp154 interaction is broken, thus allowing Asp154 to interact with a critical Arg150 needed for effective receptor binding. The defective LDLr binding of apoE2 leads to increased susceptibility to develop type III hyperlipoproteinemia in apoE2-bearing individuals; this condition is characterized by increased CM levels in the plasma, a risk factor for atherosclerosis. The poor LDLr binding ability of apoE2 results in CM remnants remaining in circulation for a longer period of time leading to deposition of TG in the arterial walls of coronary arteries.

#### ApoE4: A Risk Factor for CVD and AD

Many studies have linked apoE4 with high plasma concentrations of cholesterol (35), a risk factor for CVD. However, in contrast to apoE2, apoE4 displays LDLr binding activity that is comparable to that of apoE3. Indeed, studies have indicated that it may have a slightly higher binding affinity to the LDLr compared to apoE3, the implication of which is not currently understood (25). The molecular basis behind the aberrant behavior of apoE4 in lipoprotein metabolism that leads to CVD is not understood. It may be attributed to a combination of factors such as increased plasma clearance and lower plasma levels of apoE4 compared to apoE3, increased susceptibility to proteolysis, or poor intracellular recycling ability (42). Structural, biophysical and biochemical studies on apoE4 suggest that its role in cholesterol imbalance is related to

Arg112. Arg112 forms an intra-helical salt bridge with Glu109; as a result, the neighboring Arg61 on helix H2 is forced to point away from the helix bundle. This orientation allows Arg61 to form a salt bridge with Glu255 in the CT domain (35). The increased propensity to aggregation and proteolysis of apoE4 seems to lead to anomalous biophysical and unfolding behavior that may be due to domain-domain interactions. These studies also suggest that domain-domain interaction is responsible for the lipoprotein binding preference of apoE4 for VLDL compared to HDL (60:40 VLDL: HDL). The domain-domain interaction is less pronounced in apoE3 (and apoE2); apoE3 displays a preference for HDL over VLDL (60:40 HDL: VLDL) (35, 43). The precise role of apoE4 in AD is not understood at present. Although numerous studies have been devoted to this topic, there is no consensus as to why it is linked to AD (44).

#### X-Ray Crystal Structure of apoE3 NT Domain

The X-ray crystal structure apoE3 NT (1-191) at 2.2 Å resolution was solved in 1991 (45). The electron density is missing in the N-terminal region (1-22), 80's loop region (82-91), and the C-terminal region (166-191) in the X-ray structure (45). The structure reveals a four-helix bundle made up of one short (H1) and three long (H2, H3 and H4) amphipathic  $\alpha$ -helices. Helices 1 and 2 are linked by a short helix 1' (H1'), which is perpendicular to the helix bundle. The number of residues in each helix varies: H1 is composed of 19 residues (24-42); H1': 11 residues (44-53); H2: 28 residues (54-81); H3: 36 residues (87-122), and H4: 35 residues (130-164) (22). The most pronounced region in the NT bundle is a span of basic charged residues that form the LDLr binding region present on helix H4 (130-150). Changes in the basic charges in this region can diminish its association with acidic residues in the LDLr and thus impair

function. Other pertinent studies have also suggested that important residues that span beyond residue 164 are important for LDLr binding as can be demonstrated by deleting those regions and seeing an adverse binding affinity to the LDLr. Mutating Arg-172 which lies outside H4 abolishes binding efficiency to LDLr to 2%; interestingly an E3K mutation resulted in a two-fold increase in LDLr binding (46).

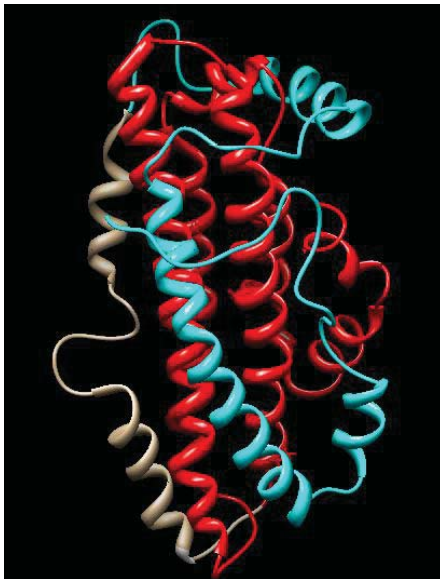


FIGURE 2. NMR structure using coordinates from mutant monomeric apoE3 (1-299) PDB 2L7B. The ribbon diagram was modeled using Chimera. Red ribbon = NT domain, Cyan ribbon = CT domain, Gray ribbon = Hinge domain.

#### NMR Solution Structure of apoE3(1-183) and apoE3(1-299)

In contrast to the X-ray crystal structure that revealed precise spatial organization of residues only between 24 and 164, subsequent NMR studies of apoE3(1-183) provided further information (47). NMR studies revealed the NT domain is 81%  $\alpha$ -helical, which is supported by CD spectroscopy data (48). In addition, they revealed that residues 12-22

and 168-180 formed short flexible helices: helix N and helix C, respectively. Helix C was further delineated as nHelix C (residues 168-172) and cHelix C (residues 174-180) with a break at G173 that allows a 90° bend in helix C. Further, this study highlights the contribution of buried polar and ionizable groups towards the function of apoE. Two buried residues (E59 and E70) are located between H1 and H2, while 6 hydrophilic residues (D107, R114, Y118, D151, R158, Y162) are buried between H3 and H4 (47). In comparison, only two buried polar residues (R145 and Q156) are located between H1 and H4, and three residues (C112, R119 and T57) between H2 and H3. Since buried polar residues tend to destabilize the helix bundle interior, the authors propose that a weaker helix-helix interface exists between H1/H2 and H3/H4 (47).

Subsequent NMR studies on the intact apoE3(1-299) in its monomeric form (24) revealed further information regarding the disposition of the CT (Figure 2). The authors carried out five substitutions in the CT domain replacing aromatic, hydrophobic residues with smaller polar or charged residues (F257A, W264R, V269A, L279Q and V287E) (24, 49, 50). This resulted in a monomeric apoE that retained all the functional features of wild type (WT) tetrameric apoE3 in terms of LDLr and lipid binding. They reported a three-domain structure: NT domain (residues 1-167), hinge domain (residues 168-205) and CT domain (residues 206-299) (Figure 2). No significant structural differences were found between the NT domain of the intact protein (1-299) and the isolated domain (1-183), (only slight alterations due to tertiary intra-helical interactions). The hinge domain encompassing the protease-sensitive loop was comprised of Hinge H1 (residues 168-172) and Hinge H2 (residues 174-180). Hinge H1 is a fully exposed helix that acts as the linker region that separates the NT and CT domains in conformational flexibility. Hinge

H2 is also a fully solvent exposed helix that was proposed to be responsible for the interaction of proteins and lipids (24). The CT domain is comprised of: Helices C1, C2, and C3, which appear to wrap around the NT domain 4-helix bundle with C1 interacting with helix H1', while C2 and C3 interact with H3 and H4. Currently it is unknown if this structure represents the actual structure of the monomeric unit in a tetrameric apoE.

#### Structure of apoE3 from Mass Spectrometric Studies

Mass spectrometry has been used to understand protein backbone dynamics of globular proteins. A recent study has utilized hydrogen deuterium exchange (HDX) coupled to mass spectrometry (MS) and proteolytic cleavage of the protein (51). The monomeric mutant forms of apoE isoforms (E2, E3, and E4) were compared to that of their respective tetrameric WT forms using HDX/MS. The purpose of this experiment was to understand the isoform related structural differences in terms of solvent penetration and conformational states. Their results confirmed that the oligomeric sites are indeed in the C-terminal end with residues 244-272 showing differential HDX between WT protein and the monomeric mutants (51). For the NT domain of apoE they saw no differences between the WT and the monomer mutant forms for each isoform in terms of deuterium uptake, signifying similar helical bundle structural organization. Further, they carried out electron transfer dissociation to extract deuterium uptake information for each amino acid. However, their analysis missed information spanning residues (30-60 and 135-160). My aim in using HDX/MS was to uncover backbone dynamics in helices to better understand the flexibility of each helix in the isolated domains without the confounding influence of domain-domain interactions.

### Lipid-Associated Conformation of apoE3

While we have a fairly good understanding of the high-resolution structure of lipid-free apoE, there is no information on its lipid-associated conformation at a comparable resolution. Several circumstantial evidence obtained from biophysical studies indicates that there is no single discrete conformation of lipid-bound apoE3. This is because there are different types of lipids, and different organization of lipid structures. From a physiological standpoint, apoE3 may be associated with VLDL, which are large spherical lipoproteins (30-80 nm diameter) composed of apoB100, apoE, apoC-I, apoC-II, apoC-III, lipids and a TG core or with a subclass of HDL, which are small spherical lipoproteins (8-11 nm diameter) composed of phospholipids, cholesterol and CE core.

These lipoproteins are not discrete sized particles; rather they undergo dynamic interconversion, facilitated by the structural flexibility of their exchangeable apolipoprotein components. Further, several lines of evidence indicate that apoE likely adopts two different lipid bound conformation in both of which the CT domain is lipid associated. However, in one state the NT domain is in a closed helix bundle lipid-free state, while in the other, the helix bundle is open, and lipid-bound (27, 52). In addition, apoE3 can be found on nascent HDL which are discoidal in geometry (7.9-9.6 nm diameter) (53) composed of a bilayer of phospholipids (with or without unesterified cholesterol) but lacking a CE core.

Studies directed at understanding the lipid-bound conformation of apoE3 have resorted to the use of reconstituted HDL (rHDL) composed of synthetic phospholipids (1,2-dimyristoyl-sn-glycero-3-phosphocholine, 1,2-dipalmitoyl-sn-glycero-3-phosphocholine or 1-palmitoyl,2-oleoyl-sn-glycero-3-phosphocholine) with or without

cholesterol, and recombinant apoE3 (isolated NT or CT domains, or full length) (54–58). The apoE3 on rHDL particles recapitulate the functional features of apoE3 on VLDL and HDL in terms of its ability to bind the LDLr. Thus, the rHDL has served as an excellent model for structural analysis of lipid bound apoE3. Electron microscopy studies show that interaction of apoE with DMPC vesicles causes transformation to rHDL which are discoidal lipoproteins complexes about 15-20 nm in diameter and ~40 Å high, roughly corresponding to a bilayer (59). Fluorescence resonance energy transfer analysis of isolated apoE3 NT domain indicates that upon lipid interaction helices H1-H2 move away from helices H3-H4, while the full length protein suggest that the CT domain unfurls from the NT domain (60). Fourier transform infrared data indicate that upon lipid interaction the helices are aligned perpendicular to the plane of the phospholipid bilayer (61).

When lipid-free apoE interacts with lipids it undergoes a large conformational change involving helix bundle opening to reveal the hydrophobic interior that permits interaction with lipids (37). This is supported by studies conducted by Lu et al. (62) wherein pairs of Cys residues were engineered between helices: H1/H2, H2/H3, H1/H4, H3/H4, H1/H2+H3/H4, and H1/H4+H2/H3 using a structure-guided approach. The rationale was that the engineered Cys pairs were spatially proximal which enabled them to form a disulfide bond, thereby “locking” the helices and prevent helix bundle opening. These authors demonstrated that upon exposure to lipids, the disulfide bonded variants: H2/H3, H1/H4 and H1/H4+H2/H3 had significantly lower rates of binding. Their research suggests separation by paired helices about a hinge between H2 and H3, i.e. H1/H2 moves away from H3/H4. However, results from this study could not exclude

alternate models of helix separation. A similar approach was employed by Narayanaswami et al. to demonstrate helix reorganization in an insect apolipoprotein, apolipoprotein III from *Manduca sexta* (63) and by Soulagest et al. in apolipoprotein III from *Locusta migratoria* (64). Taken together, these studies are indicative of the requirement of helix bundle opening for interactions with lipids.

#### Gap in Knowledge and Questions Left Unanswered

So far our current state of understanding with regard to apoE is that: (i) it is a closed helix bundle in lipid free state; (ii) it adopts an extended helix resembling a “belt” in lipid bound state, and (iii) the helix bundle undergoes a dramatic reorganization involving rupture (or disruption) of tertiary interactions in the helix bundle, movement of helices away from each other, and the hydrophobic face of the amphipathic helices establishing contacts with lipid surfaces. However, neither the mechanism of opening nor the order of opening of helix bundle are known at this point.

#### NT and CT Gap in Knowledge

Information during the initiation process of lipid-induced unfolding of the CT domain leading to intermediate conformational stages and unfurling are poorly understood. Mechanism of lipoprotein binding have been tackled by past researchers and have revealed a two-step kinetic model for apoE binding to VLDL and HDL (25). More studies must be obtained in order to gather crucial information about intermediate stages of helical unfolding intermediates to better understand apoE in biology and disease.

#### Hypothesis and Objectives

While several studies are devoted to understanding the structural organization of lipid-free apoE and lipoprotein-associated conformation adopted by apoE, very little is

known regarding mechanistic details of the transition from one state to the other. The current study seeks to understand the thermodynamics of unfolding and solvent accessibility of the isolated domains of apoE3 using fluorescence polarization spectroscopy and HDX/MS. We hypothesize that chemical denaturation induces an ordered and sequential helix unfolding process initiated in the NT domain of apoE3. We also propose that the C-terminal helix (C3) of the isolated CT domain would unfold prior to the C1 and C2.

#### Objective 1

The first objective was to assess chemical denaturant-induced change in mobility of probes introduced by site-specific fluorescence labeling to monitor defined sites. By introducing an extrinsic fluorescent probe at defined sites to monitor specific segments on apoE, we were able to follow unfolding and the accompanying changes in probe mobility by changes in fluorescence polarization. The rationale is that the ease of unfolding (as revealed by the change in free energy of unfolding) will be a reflection of ease of helix bundle opening. This involves opening of both the intra- molecular helix bundle (at the NT domain) and inter-molecular helix bundle opening (mediated by the CT domain, which facilitates protein tetramerization).

#### Objective 2

The second objective was to assess the solvent accessibility and extent of deuterium incorporation in the isolated domains of apoE3 by mass spectrometry to determine the segments of the protein that are structurally rigid and those that are relatively flexible and less structured in solution.

## CHAPTER 2

### MATERIALS AND METHODS

1,5-IAEDANS, 5-((((2-Iodoacetyl)amino)ethyl)amino)naphthalene-1-sulfonic acid (IAEDANS) was obtained from Invitrogen (Molecular Probes, Eugene, OR), Formic Acid, tris(2-carboxyethyl)phosphine hydrochloride (TCEP) from Sigma-Aldrich (St. Louis, MO), Acetonitrile from Fisher (Waltham, MA), Deuterium oxide (99.999 atom % D) from Aldrich Chemical Co (St. Louis, MO), Acquity UPLC BEH C18 1.7  $\mu$ m analytical column, Guanidine Hydrochloride (GdnHCl), Immobilized pepsin cartridge from Applied Biosystems (Eugene, OR), and Immobilized pepsin from Thermo (Rockford, IL).

#### HDX/MS Experiments

ApoE3 protein stock (4 mg/ml in 10 mM sodium phosphate buffer pH 7.4) was first diluted with the same buffer to obtain a final analytical concentration of 0.4 mg/ml and equilibrated at 0<sup>o</sup>C for 30 min. HDX was started by diluting the protein 1:10 into D<sub>2</sub>O buffer (10 mM sodium phosphate buffer, pD 7.4, 25<sup>o</sup>C). Labeling of the protein was allowed to continue for varying lengths of time: 0.5, 1, 5, 10, 15, 30, 60, and 120 min. The exchange-in reaction was arrested with cold quenching solution (10 mM phosphate buffer at pH 2.5, 50 mM TCEP) then flash frozen with liquid nitrogen until direct injection into the LC-MS. The quenched samples were injected into an online pepsin-digestion column length (2.1 mm x 30 mm) Porosyme Immobilized Pepsin

Cartridge (Applied Biosystems) containing immobilized pepsin. A nanoAcquity UPLC system (Waters, Milford, MA) operated at 50  $\mu$ L/s for 3 min was used for the online pepsin digestion. The UPLC system was coupled to a Synapt G1 electrospray ionization mass spectrometer (Waters, Milford, MA). After passing through the pepsin column, the peptic fragments were captured on a C18 guard column (1.7  $\mu$ m, 2.1 mm x 5mm, Milford, MA). Elution from the trap column was followed by injection onto a C18 analytical column (UPLC BEH C18, 1.7 $\mu$ m, 1mm x 100mm, Milford, MA) for separation of the peptide mixture using a set gradient. The gradient used for elution was set at 40 $\mu$ L/min flow rate using solvent A (LC-MS grade water, 0.1% formic acid) and solvent B (acetonitrile, 0.1% formic acid). Gradient settings were 8%-40% solvent B in 6 min, 40%-85% solvent B at 7 min, isocratic flow of 85% solvent B for 2 min and then returned to 8% solvent B in 1 min. Peptide level HDX was acquired on a Synapt G1 Waters electrospray ionization quadrupole time-of-flight (Q-TOF) mass spectrometer (Waters, Milford, MA).

#### Design of Single Cysteine Constructs

Extrinsic fluorescence experiments use thiol-reactive probes which require Cys at specified locations. Fluorophores are covalently attached to the free sulfhydryls of Cys. Single cysteine constructs were designed on the full-length apoE3(1-299), NT-domain (1-191), and CT-domain (201-299) of apoE3. This was done by examining the X-ray crystal structure of apoE3 (1-191) (PDB 1NFN) and the NMR structure of the apoE3 (1-299) monomeric mutant (PDB 2L7B).

### Site-Directed Mutagenesis

Mutations were introduced into the cDNA of apoE3 using the QuikChange II site-directed mutagenesis kit (Agilent Technology, Stratagene, La Jolla, CA). Primers were designed and synthesized by Eurofins MWG OPERON (Huntsville, AL). WT apoE3 (both full length (1-299) and isolated NT domain (1-191)) has a single endogenous Cys at position 112, which was replaced by serine with no change in function or secondary structure. All the mutant constructs with the apoEC112S mutation are designated simply as apoE, not apoE3, throughout the manuscript. In order to refer to a specific mutant construct we use the following notation: apoE followed by C112S and (1-191) or (201-299) to refer to isolated NT or CT domain, respectively. Single Cys substitution was generated on the following 8 sites: A29C, A62C, A102C and V161C for the NT domain A209C, S223C, E255C, and A277C for the CT domain.

### Expression, Isolation, and Purification of apoE Constructs

ApoE3 was overexpressed in *E. coli* BL21-Gold (DE3 )pLysS Competent Cells using pET22b expression vector containing ampicillin resistance that encodes the WT or single Cys apoE, with hexa-His tag at the N-terminal end, as described previously (65). After expression, the cells were resuspended in 10 mM sodium (or potassium) phosphate pH 7.4 containing 150 mM NaCl (phosphate buffer saline, PBS) and lysed using a microfluidizer (Microfluidics, Newton, MA). The recombinant proteins were purified using Ni<sup>2+</sup>- affinity matrix (Hi-Trap chelating column, GE Healthcare, Piscataway, NJ). Protein purity was assessed using 4-20% SDS-polyacrylamide gel electrophoresis (PAGE) under reducing conditions in the presence of 2-Mercaptoethanol or non-reducing conditions using. Protein concentration was determined in a Nano-Drop 2000/2000c

spectrophotometer (Thermo Fisher Scientific, Wilmington, DE) using the molar extinction coefficient at 280 nm of 27,960 and 16,500 M<sup>-1</sup>cm<sup>-1</sup> for apoE3(1-191) and apoE(201-299), respectively.

#### IAEDANS Labeling

Single Cys apoE variants (5 mg in 10 mM ammonium bicarbonate, pH 7.4) were initially pre-incubated with a two-fold molar excess of TCEP and a fifty-fold molar excess GdnHCl for 30 min at 24°C to reduce any disulfide bonds. After reduction, two-fold molar excess of fluorescent probe (IAEDANS) dissolved in 10 mM Tris, 150 mM sodium chloride, pH 8.0 (Tris buffered saline, TBS) was added to the protein and incubated at 37°C for 2 hrs. All purified AEDANS-labeled proteins were dialyzed extensively against TBS pH 7.4. The degree of labeling was calculated using equation 1.

$$\frac{A_{\max}}{\epsilon \times \text{protein concentration (M)}} \times \text{dilution factor} = \frac{\text{moles of dye}}{\text{mole of protein}}$$

$\epsilon$ : molar extinction coefficient of fluorescent dye;  $A_{\max}$ : absorbance maximum at 280 nm; M: protein concentration. Molar extinction coefficient of IAEDANS  $\epsilon_{340} = 5,700 \text{ M}^{-1} \text{ cm}^{-1}$ .

#### Circular Dichroism (CD) Spectroscopy

CD measurements were performed on a Jasco 810 spectropolarimeter at 24°C. Far-UV CD scans were recorded between 185 nm and 260 nm in 10 mM ammonium bicarbonate buffer, pH 7.4 using a protein concentration of 0.2 mg/ml in a 0.1 cm path length circular cuvette. The labeled and unlabeled proteins were pre-incubated with 2-fold molar excess of TCEP, pH 7.4 for 30 min at 24°C prior to measurements to reduce any disulfide bonds and unreacted Cys groups in labeled proteins. CD profiles were the

average of four scans that were recorded, with a response time 2 sec and bandwidth of 1 nm. The molar ellipticity ( $[\theta]$ ) in  $\text{deg. cm}^2 \text{ dmol}^{-1}$  at 222 nm was obtained using the equation:

$$[\theta]_{222} = (\text{MRW} \cdot \theta) / (10 \cdot l \cdot c)$$

Where MRW is the mean residue weight calculated to be 115.7 for apoE3(1-191) and 97.8 for apoE(201-299);  $\theta$  is the measured ellipticity in degrees at 222 nm;  $l$  is the cuvette path-length (in cm); and  $c$  is concentration (g/ml). The percent  $\alpha$ -helix content was calculated as described earlier (65):

$$\% \alpha\text{-helix} = 100 \cdot (3000 - [\theta]_{222}) / 39000$$

#### GdnHCl-Induced Unfolding

Denaturation curves for the apoE constructs were used to measure global protein stability and ensure that mutations did not influence their overall domain structures. Changes in molar ellipticity at 222 nm were measured as a function of increasing amounts of GdnHCl as described previously (32). Each sample was treated with GdnHCl in the presence of 2x molar excess of TCEP in 10 mM ammonium bicarbonate, pH 7.4 for 30 min at 24°C. The % maximal change was calculated from ellipticity values at  $\theta_{222}$  nm.  $[\text{GdnHCl}]_{1/2}$  is the GdnHCl concentration required to cause a 50% decrease in molar ellipticity from initial value and was calculated by the following equation.

$$\% \text{ Maximal Change} = (\theta_N - \theta) / (\theta_N - \theta_D) * 100$$

$\theta$  is the molar ellipticity at different GdnHCl concentrations,  $\theta_N$  is the molar ellipticity of the native globular domain,  $\theta_D$  is the molar ellipticity of the fully denatured domain. Free energy of stabilization of the two domains in apoE was calculated from the relationship

$$\Delta G = \Delta G^{H_2O} - RT \ln(1 + k\alpha)$$

where  $\Delta G$  is the free energy of the denaturation at each GdnHCl concentration,  $\Delta G^{H_2O}$  is the free energy of denaturation in the absence of GdnHCl,  $R$  is the gas constant ( $0.001987 \text{ kcal K}^{-1} \text{ mol}^{-1}$ ),  $T$  is the temperature (298K),  $\ln$  is the natural logarithm,  $k$  is the denaturation constant (0.8), and  $\alpha$  is the molarity of GdnHCl.  $\Delta G_D$  is calculated from the relationship

$$\Delta G = -RT \ln(K_d)$$

where  $K_d$  is the equilibrium constant for protein denaturation at each GdnHCl.  $K_d$  was obtained from the relationship

$$K_d = (\theta_N - \theta) / (\theta_N - \theta_D)$$

In order to obtain free energy values a plot was generated  $\Delta G$  vs  $\ln(1+k\alpha)$  (Figure 3) that gave a linear negative slope where the y-intercept value was the  $\Delta G$  value in the absence of GdnHCl (16).

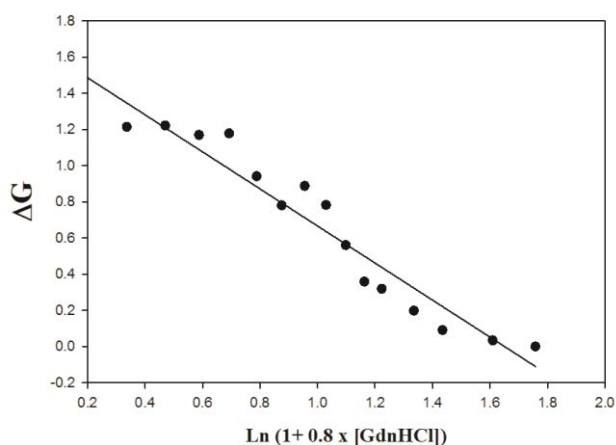


FIGURE 3. Free energy of stabilization ( $\Delta G$ ) as a function of  $[\text{GdnHCl}]$ .  $\Delta G$  at each GdnHCl concentration was calculated using  $-RT \ln(K_d)$ .

### Fluorescence Spectroscopy

The fluorescence emission characteristics of each AEDANS-labeled apoE NT and CT variant site evaluated in a Perkin-Elmer LS55B fluorometer (Perkin Elmer, Massachusetts). A quartz microsquare fluorometer cell with a maximal capacity of 450  $\mu\text{l}$  and a 4 mm path length (Starna cells, Inc., Atascadero, CA) was used for all fluorescence experiments. The solvents used were Milli-Q water, 10 mM ammonium bicarbonate, pH 7.4, 95% ethanol, and iso-propanol. The samples were excited at 340 nm and the fluorescence emission monitored from 400 - 600 nm (100 nm/min scan rate, 4.0 nm excitation and emission slit widths with 4 accumulations). All data were saved as ACSII file for subsequent plotting by Sigma Plot (ver.11.0). All the parameters for fluorescence measurements were identical to those used for polarization. The concentrations of AEDANS-labeled variants were 0.11  $\mu\text{g}/\mu\text{L}$ .

### Fluorescence Polarization

Fluorescence polarization spectroscopic measurements were made using a FluoroMax-2 spectrometer (Horiba scientific, Edison, NJ) with the following parameters with sample concentration  $\sim 0.11 \mu\text{g}/\mu\text{L}$ . The sample volume was 450  $\mu\text{L}$ , a 3mm square cuvette was used and the experiment type was set to polarizer mode. The excitation and emission wavelength were set to 340 nm and 480 nm respectively with an integration time of 0.1 s and 5 nm slit width.

### Statistical Analysis

Data are represented as mean  $\pm$  SD from three independent experiments.

Statistical analysis was performed using the Microsoft Excel Student's t test;  $P < 0.05$  was considered to be statistically significant.

## CHAPTER 3

### RESULTS

#### Objective 1: Order of Helical Unfolding of the apoE NT and CT Domains

The objective of the present study was to utilize steady-state fluorescence spectroscopy to understand the thermodynamics of: (i) unfolding of the NT domain helix bundle opening, and (ii) unfolding of the CT domain during GdnHCl induced denaturation. The high-resolution structure of apoE3 NT domain served as a structural guide to substitute single Cys at specific sites for labeling with IAEDANS. The extent of tertiary contacts (H-bonding, hydrophobic, Van der Waals forces and electrostatic interactions) between helices H1, H2, H3, and H4 (Figure 4) vary at different helical interfaces, which serves as basis for developing our hypothesis about helix bundle stability and can potentially explain the mechanism of helix-bundle opening. The rationale to this approach is that regions with more inter- and intra-helical interactions would be harder to disrupt (i.e. would require higher concentrations of GdnHCl (denaturant)) and remain in close contact due to a greater extent of tertiary contacts, while those with fewer contacts would be easier to disrupt and require lower GdnHCl concentration to unfold. Based on the contact map one would predict that H3 and H4 would be harder to disrupt compared to H1 and H2 where the distances between residues are greater (Figure 4). Less distance between residues would contribute to stronger overall interactions leading to stabilization of helices.

In previous studies, CD spectroscopy was used to follow GdnHCl-induced helix bundle unfolding; this would show loss in helical content and the overall unfolding pattern (21). However, an alternative approach of placing probes at desired locations and following unfolding to monitor changes in fluorescence polarization, would offer additional information about localized changes in mobility at specified locations, an important aspect to address from a mechanistic perspective. In order to test the hinge mediated unfolding hypothesis, we propose that the NT domain helix bundle opens via a single hinge located between H2 and H3 (“one-hinge model i.e. opening like a book”) by which the protein can potentially open to release the helices from the bundle state, such that the H1/H2 pair moves away from the H3/H4 pair. Such a movement would expose the hydrophobic interior allowing the NT domain to subsequently bind to lipid substrate. Increasing denaturant concentration is expected to disrupt tertiary interactions followed by loss in rigid helix structures ultimately adopting random coil structures. Segments encompassing limited tertiary contacts will thus unfold at lower GdnHCl concentration and allow us to monitor differences in flexibility or mobility of probes located on specific helices within the helix bundle through polarization experiments.

With regard to the CT domain, we employed a similar approach to monitor order of helical unfolding. Of the three available high resolution structures of apoE, only one, the NMR structure of apoE(1-299) (PDB 2L7B) shows the organization of the residues 201-299 in the CT domain in a monomeric state. Since the monomeric protein was obtained by substituting several hydrophobic residues with polar residues, it is not known if the domain organization noted in the NMR structure of the monomeric protein

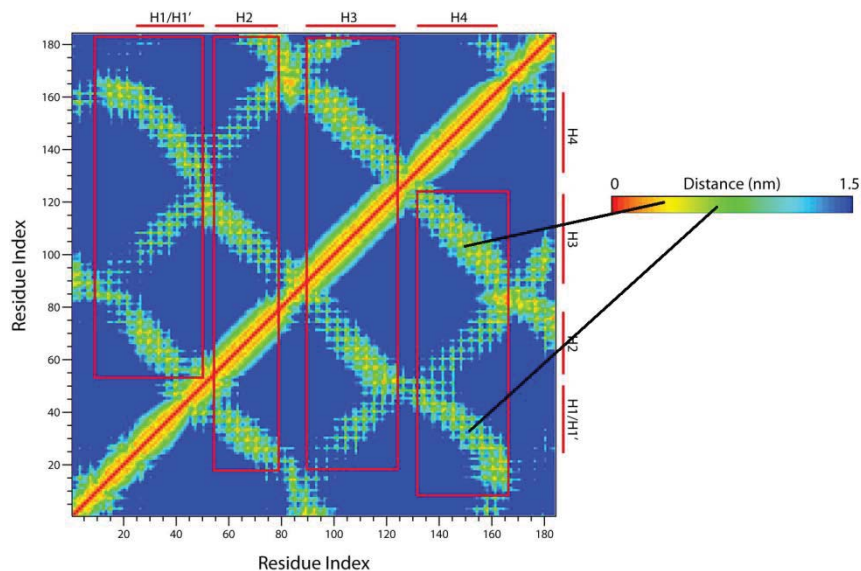


FIGURE 4. Contact map of apoE3 NT domain showing residue distances between helices. The contact map is based on the NMR structure of apoE3(1-183) (PDB 2KC3) (47). The red boxes indicate the residue span of each helix. Helix-helix contacts can be gauged using color coded Residue Index to reflect the distances of intra-helical residues in the NT domain. Black lines draw attention to regions making extensive contact (yellow-red) versus medium contacts (yellow-green). Top line: Extensive contacts, Bottom line: Minimum contacts.

represents that in the monomeric unit of native tetrameric apoE3. To follow the order of helical unfolding in the CT domain, we employed: (i) isolated apoE CT domain encompassing residues 201-299 (but retained the residue number of the intact protein for the sake of simplicity), and (ii) the model developed previously in our lab for isolated CT domain molecular organization based on fluorescence spectroscopy (32), wherein we proposed that the *entire CT domain* from four apoE molecules (not merely the terminal segment of the CT domain as previously proposed by Westerlund and Wesigraber (18) come together to form an *inter-molecular* 4-helix bundle. To monitor the order of helix

unfolding induced by GdnHCl, we sampled different segments in the CT domain. Implicit in this process is the dissociation of the tetrameric protein to monomeric form and the unfolding of the individual segments. These two processes (dissociation and unfolding) may occur simultaneously or sequentially. Our current approach is unable to distinguish between these two possibilities.

#### Design of Single Cys Constructs

To determine the order of helical unfolding of apoE NT domain, single Cys mutants were engineered to attach a fluorescent probe to monitor each helix (H1-H4) present on the 4-helix bundle. The probe of choice was IAEDANS (66), an environmentally sensitive fluorophore that has been used extensively to monitor protein dynamics (67). The X-ray crystal structure of apoE (1-191) (22) was examined by using the free online Chimera software developed by UCSF (Figure 5). Residues in helices H1, H2, H3 and H4 that were exposed to aqueous environment were selected for substitution with Cys (Table 1). Cys was the amino acid of choice for substitution as it allowed us to exploit the reactivity of the –SH group to act as a nucleophile and attack the iodoacetamide group of IAEDANS for targeted covalent attachment. The selected sites faced away from the helix bundle interior reducing overall conformational interference with neighboring helices, resulting in minimum steric hindrance (Figure 5). The expectations was that these exposed locations would not affect helix bundle stability. It would also allow for efficient tagging of Cys residues facing outwards.

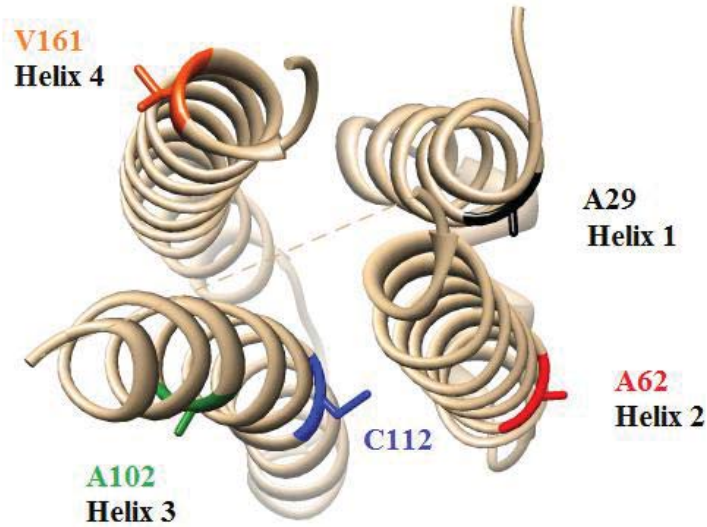


FIGURE 5. Structure guided design for single Cys constructs of apoE3 NT domain. The X-ray crystal structure of apoE3 (residues 1-191) (PDB ID 1NFN) was modeled using Chimera. Residues A29, A62, A102 or V161 shown in ball and stick model were selected for site-directed mutagenesis for substitution by Cys. Endogenous Cys at position 112 was substituted by serine in each construct.

Prior to generating the single Cys constructs, the endogenous Cys at position 112 was substituted by serine (C112S). The selected sites for cysteine substitution on apoE NT were: apoEC112S/A29C(1-191), apoEC112S/A62C(1-191), apoEC112S/A102C(1-191), and apoEC112S/V161C(1-191) (Table 1). WT apoE3 NT (bearing Cys112) was used as a control. The selected sites for cysteine substitution on apoE CT were: apoEA209C(201-299), apoES223C(201-299), apoEE255C(201-299), and apoEA277C(201-299). WT apoE(201-299) (with no endogenous or substituted Cys) was used as control where relevant. The rationale for apoE CT Cys substitution was based on the NMR structure of full length apoE (24).

TABLE 1. ApoE NT and CT Single Cys Constructs.

ApoE NT helix	Substitution	ApoE CT helix	Substitution
Helix 1 (H1)	apoEC112S/A29C(1-191)	Helix C1	apoEA209C(201-299)
Helix 2 (H2)	apoEC112S/A62C(1-191)	Helix C1	apoES223C(201-299)
Helix 3 (H3)	apoEC112S/A102C(1-191)	Helix C2	apoEE255C(201-299)
Helix 4 (H4)	apoEC112S/V161C(1-191)	Helix C3	apoEA277C(201-299)

### SDS-PAGE Analysis of ApoE NT and CT Variants

Single-Cys apoE variants with hexa-His tag at the N-terminal end were over-expressed in BL21-Gold (DE3) *E. coli* competent cells, isolated, and purified using a HiTrap Nickel column as described previously (30, 57). The purified proteins were dialyzed against 10 mM ammonium bicarbonate, pH 7.4, lyophilized and stored at -20°C. The yield of protein was ~16 mg/L culture. SDS-PAGE analysis of the purified apoE NT (Figure 6A) and apoE CT (Figure 6B) variants was carried out to assess the molecular mass and purity of the preparations. Figure 6A shows apoE NT variants under reducing (Lanes 1-4) and non-reducing (Lanes 5-7) conditions. The calculated molecular masses of the His-tag proteins using the online tool ExPasy (<http://www.expasy.org/>) and the measured mass from SDS-PAGE analysis are shown in Table 2. The calculated masses of WT apoE3 NT and apoE CT domains are 24,076.2 Da and 13,342.9 Da, respectively. The corresponding measured masses are: ~28.3 kDa and ~13.5 kDa. All single Cys apoE NT variants show a single band under reducing conditions, Lanes 1-4. All migrate as a single band with molecular mass ~ 24 kDa under non-reducing conditions (Lanes 5-7), with the exception of apoEC112S/A62C, Lane 6 (Figure 6A), which shows an additional band with mass ~ 48 kDa corresponding to a dimer. Figure 6B shows CT variants under

reducing (Lanes 1-5) and non-reducing (Lanes 6-9). WT apoE CT and single Cys variants show a major band corresponding to ~13 kDa under reducing conditions, Lanes 1-5 (Figure 6B). The single Cys variants show an additional band at ~24 kDa, corresponding to a dimer (Lanes 2-9) with molecular masses of ~26,667.9. The dimeric band is significant in the case of apoES223C(201-299), apoEE255C(201-299), and apoEA277C(201-299) (Figure 6B).

TABLE 2. Calculated and Measured Molecular Masses of Single Cys apoE Variants

ApoE Constructs <sup>1</sup>	Calculated <sup>2</sup> (Da)	Measured <sup>3</sup> (from SDS-PAGE) (kDa)
WT apoE3(1-191)	24076.2	28.3
ApoEC112S(1-191)	24060.1	28.3
ApoEC112S/A29C(1-191)	24092.2	28.3
ApoEC112S/A62C(1-191)	24092.2	28.3
ApoEC112S/A102C(1-191)	24092.2	28.3
ApoEC112S/V161C(1-191)	24032.1	28.3
WT apoE(201-299)	13342.9	13.5
ApoEA209C(201-299)	13375.0	13.5
ApoES223C(201-299)	13359.0	13.5
ApoEE255C(201-299)	13317.0	13.5
ApoEA277C(201-299)	13375.0	13.5

<sup>1</sup>All masses with His-tag; 208 aa in total (including His-tag) for apoE(1-191) and 116 aa for apoE(201-299)

<sup>2</sup>Molecular mass calculated based on amino acid sequence (<http://www.expasy.org/>)

<sup>3</sup>Molecular mass measured from SDS-PAGE under reducing conditions by plotting log MW of marker proteins versus relative migration.

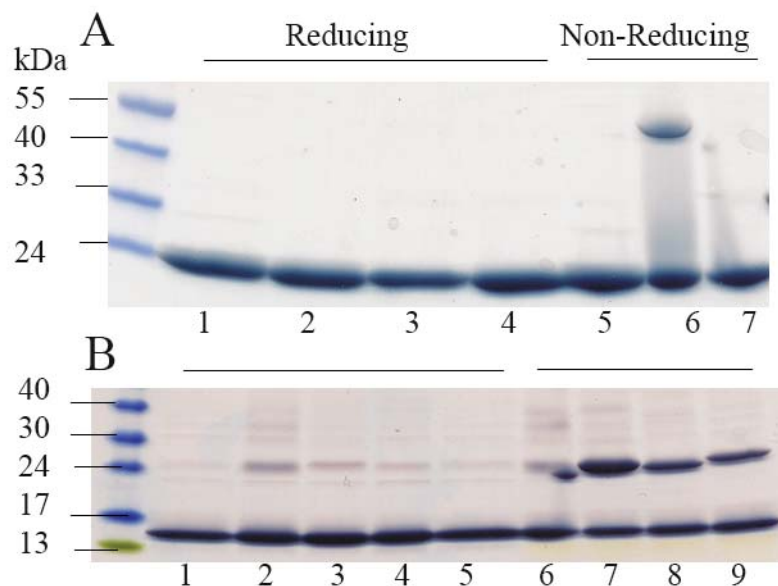


FIGURE 6. SDS-PAGE of unlabeled single cysteine apoE NT and CT variants. (A) About 10  $\mu$ g of purified apoE(1-191) NT variants were electrophoresed on a 4-20% acrylamide gradient gel under reducing conditions in the presence of 2-Mercaptoethanol ( $\beta$ -Me) (Lanes 1-4) or non-reducing conditions in the absence of  $\beta$ -Me (Lane 5-7). Lanes 1 and 5: A29C; Lanes 2 and 6: A62C; Lanes 3 and 7: V161C; Lane 4: WT. (B) About 10  $\mu$ g of purified apoE(201-299) CT variants were electrophoresed as in A, under reducing conditions (Lanes 1-5) and non-reducing conditions in the absence of  $\beta$ -Me (Lanes 6-9). Lane 1: WT; Lanes 2 and 6: A209C; Lane 3 and 7: S223C; Lanes 4 and 8: E255C; Lanes 5 and 9: A277C.

## IAEDANS Labeling and Stoichiometry of Labeling

Protein labeling under reduced conditions made it possible for efficient Cys nucleophilic attack on the iodoacetamide group of the IAEDANS molecule (Figure 7). Covalent attachment occurred with the elimination of iodine as the leaving group and subsequent Cys-AEDANS bond and HI formation.

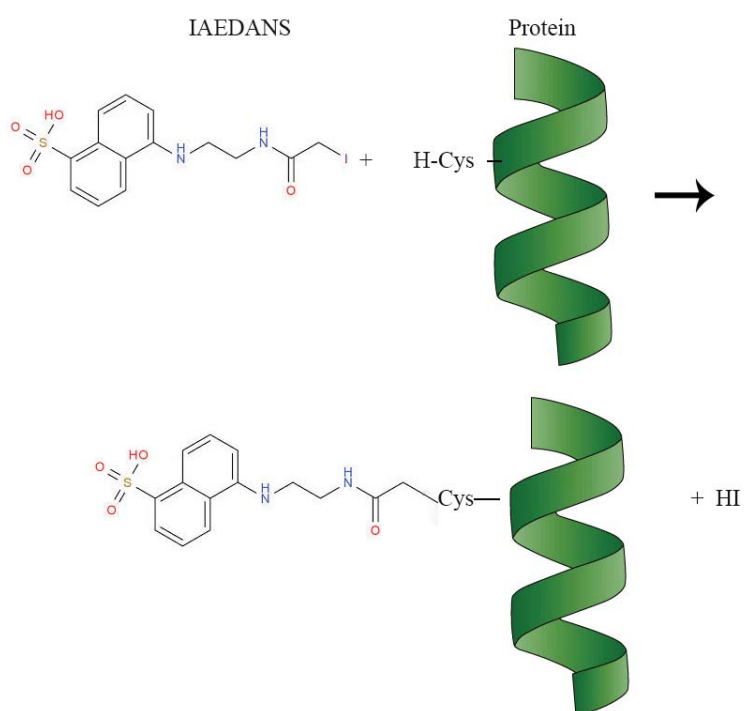


FIGURE 7. Chemical reaction of IAEDANS with free sulfhydryl group on proteins. The reactive iodoacetamide group on the naphthalene derivative binds covalently to sulfhydryl groups of Cys residue.

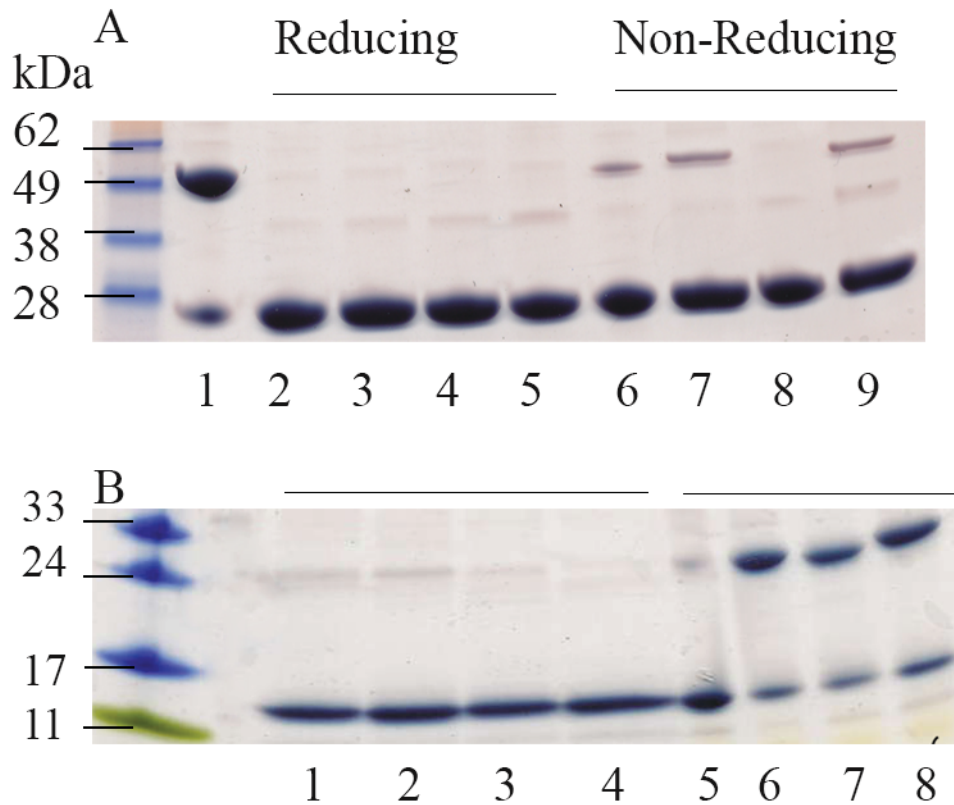


FIGURE 8. SDS-PAGE of AEDANS-labeled apoE NT and CT variants. A. About 10  $\mu\text{g}$  of AEDANS-labeled apoE C112S NT variants were electrophoresed on a 4-20% acrylamide gradient gel under reducing conditions in the presence of  $\beta\text{-Me}$  (Lanes 2-5) or non-reducing conditions in the absence of  $\beta\text{-Me}$  (Lanes 1, and 6-9). Lane 1: non-reduced apoE3 C112 WT; Lane 2: A29C reduced; Lane 3: A62C reduced; Lane 4: A102C reduced; Lane 5: V161C reduced; Lane 6: A29C non-reduced; Lane 7: A62C non-reduced; Lane 8: A102C non-reduced; Lane 9: V161C non-reduced. B. About 10  $\mu\text{g}$  of AEDANS-labeled apoE(201-299) CT variants were electrophoresed as in A, under reducing conditions in the presence of  $\beta\text{-Me}$  (Lanes 1-4) or non-reducing conditions in the absence of  $\beta\text{-Me}$  (Lanes 5-8). Lane 1: A209C reduced; Lane 2: S223C reduced; Lane 3: E255C reduced; Lane 4: A277C reduced; Lane 5: A209C non-reduced; Lane 6: S223C non-reduced; Lane 7: E255C non-reduced; Lane 8: A277C nonreduced.

All the single Cys variants were initially reduced with TCEP and then labeled with IAEDANS. To assess the extent of labeling and to check if the reduction was complete, AEDANS-labeled apoE NT and CT variants were examined by SDS-PAGE on a 4-20% acrylamide gradient under reducing and non-reducing conditions (Figure 8). Under reducing conditions, a ~24 kDa band was noted in all AEDANS-labeled apoE NT variants (Figure 8A, Lanes 2-5). Under non-reducing conditions the 24 kDa band was the major band in all variants as well; in the case of AEDANS-labeled A29C, A62C, and V161C apoE NT variants, a minor 48 kDa was also present (Lanes 6, 7, and 9 respectively): this corresponds to a dimer, which can be explained by the presence of intermolecular disulfide bonds possibly due to incomplete reduction.

All AEDANS labeled apoE CT variants migrated as a single band corresponding to ~ 13 kDa under reducing conditions, Figure 8B, Lanes 1-4. Under non-reducing conditions, while a 13 kDa band was present in all cases, a band at ~26 kDa was predominant for S223C, E255C and A277C. This is due to  $\ll$  100% AEDANS labeling. This observation also suggests that S223, E255 and A277 have lower accessibility to labeling, likely due to their location at apoE tetramerization sites.

Subsequently, the stoichiometry of labeling was calculated from the UV-Vis absorption spectrum of the labeled proteins using molar extinction coefficient of IAEDANS ( $5,700 \text{ M}^{-1} \text{ cm}^{-1}$ ) at 340 nm, as shown by equation 1 on page 20. Table 3 shows a sample calculation of a 1.277 mg/ml solution AEDANS-apoEC112S/A29C protein.

TABLE 3. Sample Calculation for Stoichiometry of Labeling

A340 nm	$\epsilon_{340}$	MW	mg/ml	Ratio
0.189	$5700 \text{ M}^{-1} \text{ cm}^{-1}$	24,000	1.277	1.01

TABLE 4. Stoichiometry of Labeling of AEDANS Labeled Single Cys apoE Variants

Labeled apoE variant	Stoichiometry of Labeling
AEDANS- ApoEC112S/A29C(1-191)	0.92
AEDANS- ApoEC112S/A62C(1-191)	0.94
AEDANS- ApoEC112S/A102C(1-191)	0.90
AEDANS-C112(1-191) WT	0.6
AEDANS- ApoEC112S/V161C(1-191)	1.2
AEDANS-ApoEA209C(201-299)	0.97
AEDANS-ApoES223C(201-299)	1.1
AEDANS-ApoEE255C(201-299)	0.97
AEDANS-ApoEA277C(201-299)	0.49

The stoichiometry of labeling was calculated to be  $\sim 1.0$  for all variants, indicative of near complete labeling (Table 4) with the exception of AEDANS-C112(1-191) WT and AEDANS-apoE A277C (201-299). This result is at variance with SDS-PAGE data that shows significant presence of unlabeled (i.e. dimers) species especially for AEDANS-apoE CT S223C, E255C, and A277C. The reason for this discrepancy is not known at this time.

#### Secondary Structural Analysis of AEDANS-Labeled Single Cys ApoEC112S NT and ApoE CT Variants

Far-UV CD analysis was performed to monitor the secondary structure of AEDANS-labeled apoE NT variants and compared to that of WT protein (Figure 9A). A typical  $\alpha$ -helical profile characterized by troughs at 208 and 222 nm was observed for all the variants. The  $\alpha$ -helical contents were determined to be 50.6-57.2% as determined

from their molar ellipticities at 222 nm (-10000 to -20000 deg. cm<sup>2</sup> mol<sup>-1</sup>) (Table 5). The  $\alpha$ -helical content of the AEDANS-labeled apoE CT variants was found to be 60.3 – 74.1%, whereas that of the unlabeled WT apoE(201-299) was 59.4%, Figure 9 and Table 5. Statistical analysis by Student’s t test shows there was no significant difference between the  $\alpha$ -helical content of variants and their corresponding WT (P > 0.05) . Overall, CD analysis showed that introduction of cysteines followed by AEDANS labeling did not alter the overall secondary structure of all the labeled variants and that they share similar helical content to reported values of corresponding unlabeled WT apoE variants (21).

TABLE 5.  $\alpha$ -helical Content of AEDANS-Labeled ApoE NT and CT Variants.

AEDANS-labeled apoE variants	$\alpha$ -helical content Mean $\pm$ SD
ApoEC112S/A29C(1-191)	50.6 $\pm$ 7.2%
ApoEC112S/A62C(1-191)	52.0 $\pm$ 7.7%
ApoEC112S/A102C(1-191)	56.7 $\pm$ 2.0%
ApoEC112S/V161C(1-191)	57.2 $\pm$ 6.9%
ApoEC112(1-191) WT	55.8 $\pm$ 1.9%
ApoEA209C(201-299)	74.1 $\pm$ 4.3%
ApoES223C(201-299)	68.4 $\pm$ 0.8%
ApoEE255C(201-299)	67.3 $\pm$ 10%
ApoEA277C(201-299)	60.3 $\pm$ 12%
ApoE(201-299) WT	59.4 $\pm$ 7.8%

#### Chemical Denaturation of AEDANS-Labeled Single Cys apoEC112S NT and CT Variants

The initial objective was to determine the thermodynamic parameters of GdnHCl-induced unfolding of apoE and to understand the extent of tertiary contact. Our aims were directed at monitoring protein dynamics, flexibility, localized changes in mobility

by following the spectroscopic behavior of fluorescent probe AEDANS. To achieve this, we adopted three-pronged experimental strategy: (i) determine if the presence of AEDANS at different sites altered the secondary structure and overall global fold of apoE NT and CT domains by monitoring GdnHCl-induced changes in secondary structure by CD analysis; (ii) evaluate GdnHCl-induced changes in the polarity of the probe's (and therefore each individual helix's) microenvironment by monitoring change in fluorescence emission intensity and in wavelength of maximal fluorescence emission ( $\lambda_{\max}$ ), and, (iii) identify GdnHCl-induced changes in probe's (and therefore each individual helix's) mobility and dynamics as an indicator of change in localized structure by monitoring change in FP.

#### GdnHCl-Induced Denaturation of AEDANS-Labeled apoE Variants followed by CD

Unfolding studies were conducted for the AEDANS-labeled single Cys apoEC112S NT variants (0.2 mg/ml) using increasing concentrations of GdnHCl. The samples were treated with TCEP to reduce any residual S-S bonds prior to analysis. Raw data was obtained by measuring ellipticity at 222 nm ( $\theta_{222\text{nm}}$ ) and converting it into molar ellipticity to account for protein molecular weight and concentration. Molar ellipticity was plotted against [GdnHCl] (0-6 M) to obtain denaturation curves and total loss in secondary structure (Figure 10A). The same data was plotted as % maximal change from 0 M GdnHCl as a function of [GdnHCl] (Figure 10B). The denaturation profiles were monophasic for the variants with the mid-point of denaturation ( $D_{1/2}$ )  $\sim$  2.5 M (Table 6).

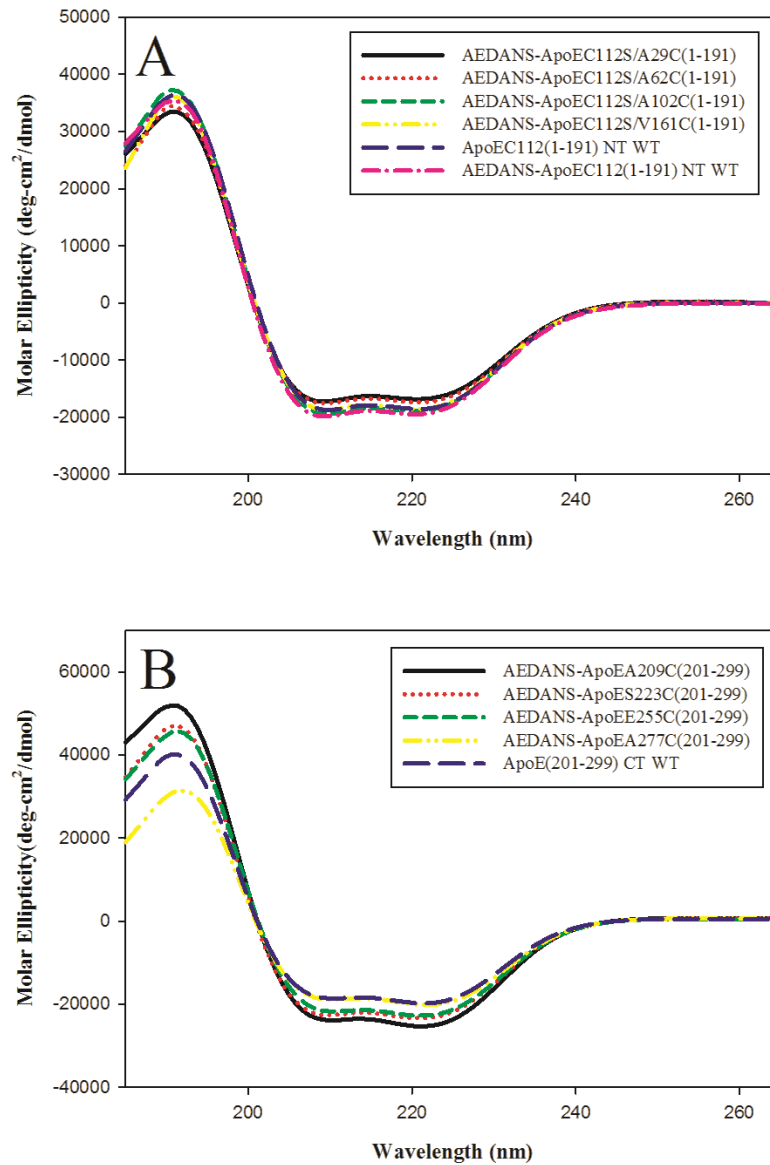


FIGURE 9. Far-UV CD spectra of AEDANS labeled single Cys apoEC112S NT and CT variants. A. AEDANS labeled NT variants. B. AEDANS labeled CT variants. Secondary structural analysis was performed with 0.2 mg/mL of all labeled variants in 10 mM ammonium bicarbonate buffer, pH 7.4, in the presence of two-fold molar excess TCEP (1mm path length cuvette). An average of 4 scans were recorded, scan speed of 20 nm/min, and response time of 1 s.

These values were comparable to that of unlabeled WT apoE3 NT ( $D_{1/2} \sim 2.77 \pm 0.05$  M), which is in agreement with prior reports from our lab (65) and other groups (62). The difference between WT and variants was attributed to experimental variations. The free energy of unfolding ( $\Delta G$ ) for the AEDANS-labeled NT variants ranged from 1.9 to 2.2 kcal/mol, which is not significantly lower than that of WT apoE3 ( $P > 0.26$ ). These results indicate that with the exception of 112, covalent attachment of the AEDANS probe at the other selected sites (29, 62, 102 or 161) in the NT domain did not significantly alter the overall fold of the protein. GdnHCl-induced unfolding studies were performed with 0.2 mg/ml AEDANS-labeled single Cys apoE CT variants as described above, (Figure 11, Panels A and B). The denaturation profiles were monophasic for the AEDANS-labeled CT variants as well with  $D_{1/2}$  between 1.4 and 1.7 M (Table 6). The free energy of unfolding for the AEDANS-labeled apoE CT variants ranged from 1.7 -1.9 kcal/mol. These values are comparable to that for unlabeled apoE(201-299) CT WT with  $D_{1/2}$  and  $\Delta G$  of 1.5 M and 1.7 kcal/mol, respectively. This suggests that covalent attachment of the AEDANS probe at the Cys substituted locations at 209, 223, 255 and 277 did not significantly alter the overall fold and thermodynamic stability of the CT domain.

#### GdnHCl-Induced Denaturation of AEDANS-Labeled apoE Variants Followed by Changes in Fluorescence Emission Intensity and $\lambda_{\max}$

Several lines of evidence indicate that apoE undergoes a large conformational change during transition from lipid-free to lipid-bound state to adopt a conformation that is able to recognize and interact with the LDLr. This change involves dissociation of the tetramer at the CT domain, movement of the two domains away from each other, and

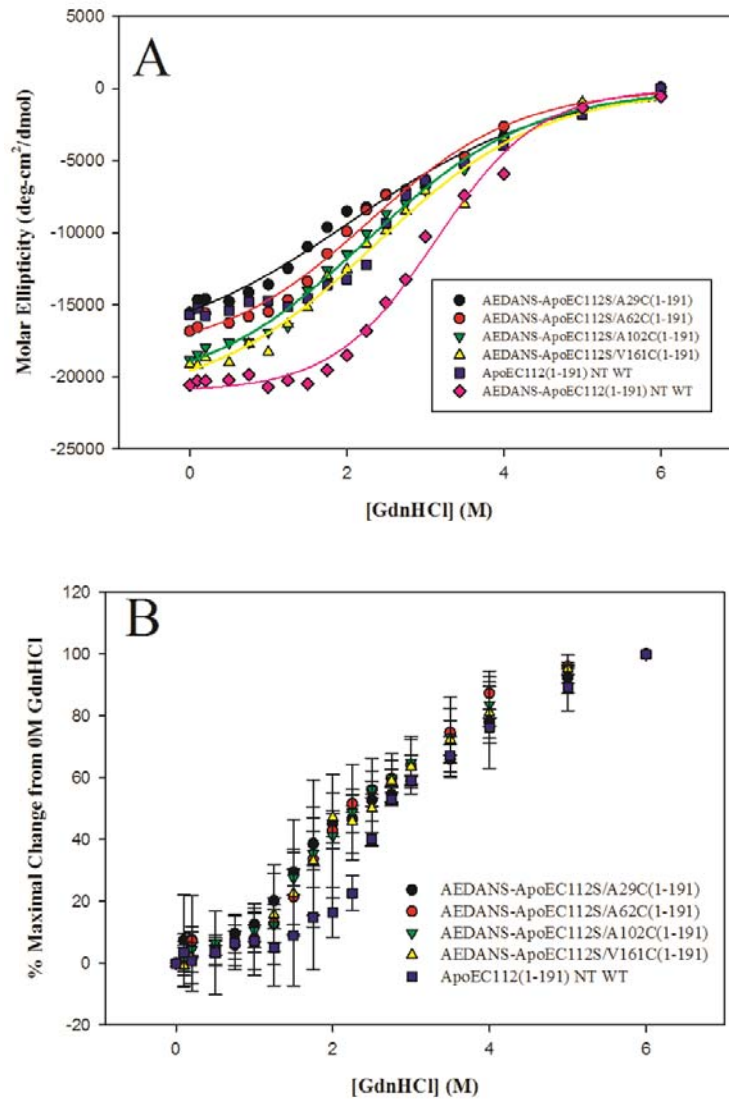


FIGURE 10. GdnHCl-induced unfolding of AEDANS labeled apoE NT variants as measured by CD spectroscopy. A. Plot of molar ellipticity versus [GdnHCl]. Changes in secondary structure were monitored as changes in molar ellipticity at 222nm. B. Plot of % maximal change from 0M GdnHCl of variants (0.2 mg/ml) versus [GdnHCl]. This plot allows us to easily derive mid-point of denaturation. Curve fitting was performed in Sigma Plot using best-fit dynamic curve fitting.

TABLE 6. Midpoint of Denaturation and Change in Gibbs Free Energy of GdnHCl-Induced Unfolding of AEDANS-Labeled apoE NT and CT Constructs Measured by CD Spectroscopy

AEDANS-labeled apoE variants	D <sub>1/2</sub> (M) Mean ± SD	ΔG kcal/mol Mean ± SD	n <sup>1</sup>
AEDANS-labeled apoE NT variants			
ApoEC112S/A29C(1-191)	2.48 ± 0.13	1.9 ± 0.4	3
ApoEC112S/A62C(1-191)	2.43 ± 0.12	2.2 ± 0.4	3
ApoEC112S/A102C(1-191)	2.42 ± 0.45	2.0 ± 0.1	3
ApoEC112S/V161C(1-191)	2.53 ± 0.48	2.1 ± 0.4	3
ApoEC112(1-191) NT WT	3.11	3.21	1
AEDANS-labeled apoE CT variants			
ApoEA209C(201-299)	1.7	1.7	1
ApoES223C(201-299)	1.6	1.8	1
ApoEE255C(201-299)	1.6	1.9	1
ApoEA277C(201-299)	1.4	1.8	1
Unlabeled ApoE Variants			
<sup>2</sup> ApoEC112(1-191) NT WT	2.77 ± 0.05	2.1 ± 0.6	3
<sup>2</sup> ApoE(201-299) CT WT	1.5	1.7	1

<sup>1</sup>number of measurements

<sup>2</sup>thermodynamic parameters for unfolding of unlabeled apoE(201-299) shown for comparison

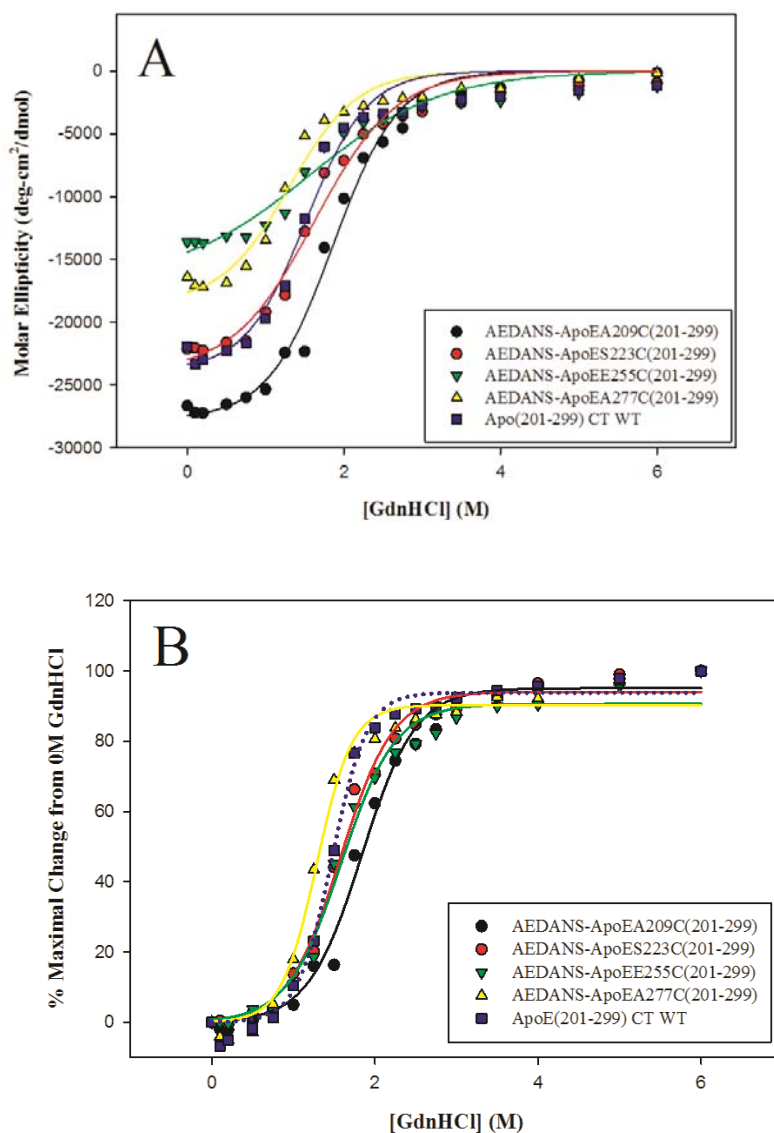


FIGURE 11. GdnHCl-induced unfolding of AEDANS labeled apoE CT variants as measured by CD spectroscopy. A. Plot of molar ellipticity versus [GdnHCl]. Changes in secondary structure of variants (0.2 mg/ml) were monitored as changes in molar ellipticity at 222 nm. B. Plot of % maximal change from 0 M GdnHCl versus [GdnHCl]. Curve fitting was performed in Sigma Plot using best-fit dynamic curve fitting.

opening of the NT domain helix bundle. During this process, we expect different sites to undergo changes in polarity of their microenvironment, an aspect that is reflected in the fluorescence emission behavior of environmentally-sensitive probes such as AEDANS. Specifically, the probe undergoes changes in fluorescence emission intensity and/or spectral shift in  $\lambda_{\text{max}}$  depending on the extent of exposure to the aqueous environment: a decrease in fluorescence emission intensity and/or a shift in  $\lambda_{\text{max}}$  towards longer wavelengths (red-shift) is typically indicative of relocation of the probe to a more polar microenvironment. The decrease in emission intensity during unfolding is generally attributed to quenching by water as the probe is exposed to the aqueous environment, while the red-shift is attributed to solvent relaxation effect in the excited state. Conversely, an increase in intensity and/or shift to shorter wavelengths (blue-shift) is indicative of a more non-polar environment. An additional advantage of AEDANS is its relatively long fluorescence lifetime (10-15 ns), which makes it ideal for FP analysis (66), an aspect that is exploited in the next section.

The fluorescence emission spectra of the various AEDANS-labeled single Cys apoE NT and CT variants are shown in Figure 12, Panels A and B, respectively. Table 8 lists the shift in  $\lambda_{\text{max}}$ . Among the NT variants, those bearing AEDANS at position 29 or 161 had a lower  $\lambda_{\text{max}}$  indicative of a relatively non-polar environment for the probe in the native state of the protein. The largest shift was seen in AEDANS-labeled apoEC112S/V161C, with a change of 21 nm (Table 8). Although our initial design took into account exposure of defined residues to aqueous environment (Figure 5), the difference in  $\lambda_{\text{max}}$  between the variants is attributed to differences in polarity in the localized microenvironment. Nonetheless, it has no bearing on our overall

experimental design. Figure 12B the fluorescence emission spectra of apoEA277C(201-299) shows a lower intensity due to its 50% AEDANS labeling. CT variant A209C has a blue-shifted spectra when excited at 340nm (Figure 12B).

In an attempt to gather direct experimental evidence for opening of the NT domain helix bundle and dissociation of the CT domain, we followed the changes in fluorescence emission intensity and  $\lambda_{\max}$  of AEDANS attached to different helices in the single Cys apoE variants Figure 13 shows the emission spectra for AEDANS-labeled apoEC112S/A29C. There was an overall decrease in quantum yield and red-shift in  $\lambda_{\max}$  with increasing GdnHCl. An overall 50% decrease in emission intensity was noted with increasing [GdnHCl] for all the NT variants (Figure 14A). AEDANS-labeled apoEC112(1-191) WT apoE was not followed due to the probe facing the interior of the helix bundle. V161C shows higher emission intensity at 0 M GdnHCl compared to others because it may be experiencing a non-polar environment and thus decreasing its quenching effects by the solvent.

In addition, the  $\lambda_{\max}$  increased by 9-20 nm with increasing [GdnHCl] for all variants, Figure 14B and Table 8. Figure 14C shows the percentage maximal change in emission intensity from 0 M GdnHCl for all apoEC112S NT variants. Table 6 shows  $D_{1/2}$  and  $\Delta G$  values for all NT and CT variants.

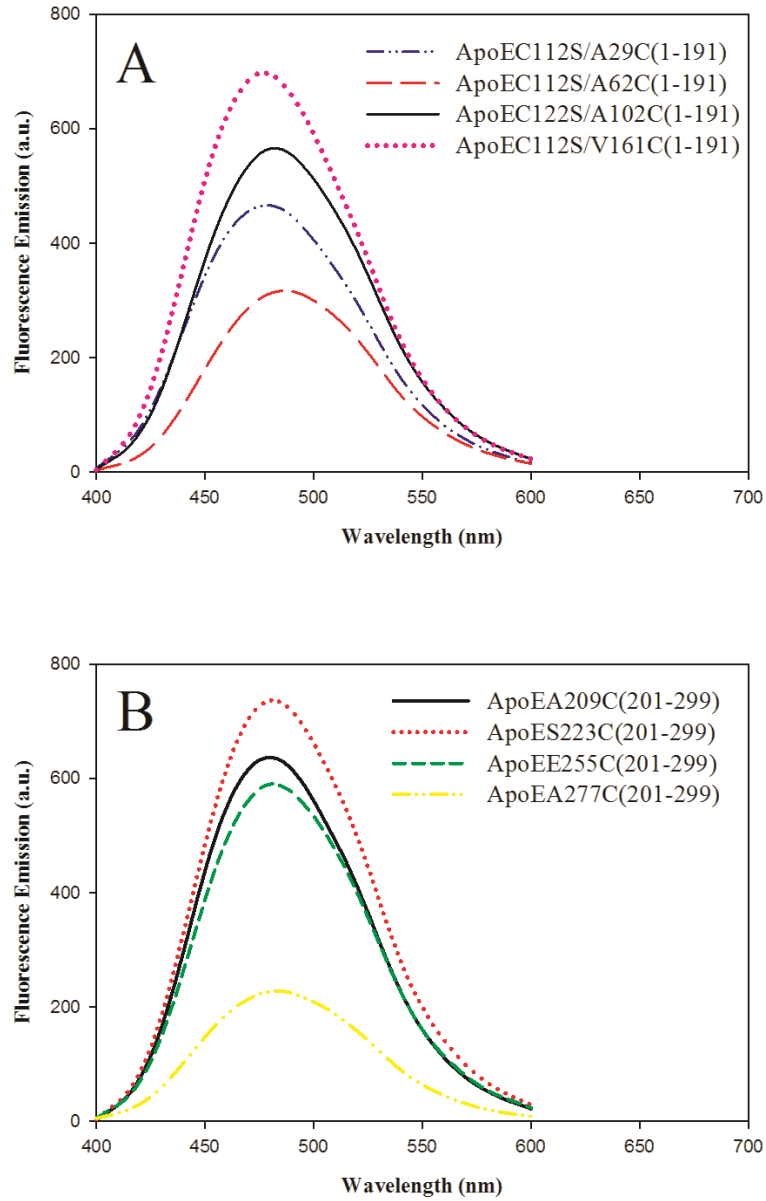


FIGURE 12. Fluorescence emission spectra of AEDANS-labeled apoE NT and CT variants. The emission spectra of 0.05 mg/ml AEDANS-labeled NT (Panel A) and CT (Panel B) variants in 10 mM ammonium bicarbonate buffer pH 7.0 were recorded following excitation at 340 nm.

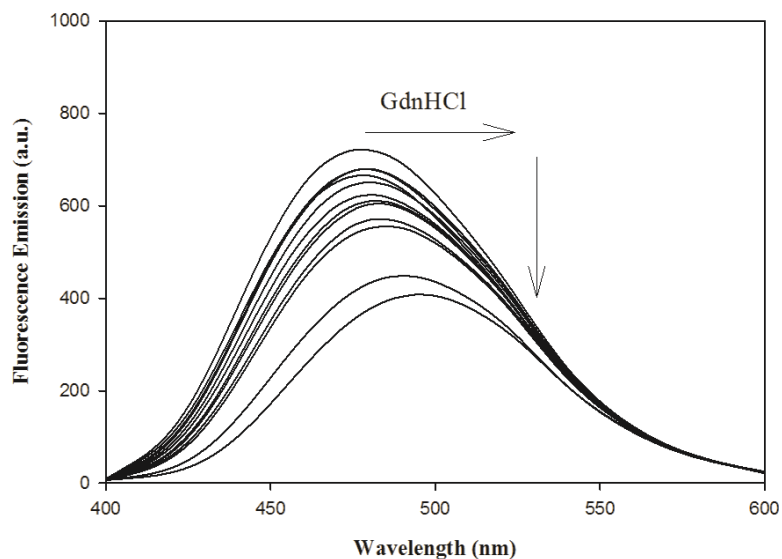


FIGURE 13. Fluorescence emission spectra of AEDANS-labeled apoEC112S/A29C at various GdnHCl concentrations. The spectra of 0.05 mg/ml sample in 10 mM ammonium bicarbonate pH 7.4, 1 mM TCEP were recorded at the following [GdnHCl]: 0, 0.2, 0.75, 1.0, 1.25, 1.5, 2.0, 2.25, 2.75, 3.0, 4.0, and 6.0 M, following excitation at 340 nm. The concentration of GdnHCl increases in the direction of the black arrow.

The changes in fluorescence emission intensity and  $\lambda_{\max}$  as a function of increasing GdnHCl in the different AEDANS-labeled single Cys variants of apoE(201-299) are shown in Figure 15, Panels A and B, respectively. Panel C shows the percent maximal change in emission intensity from 0 M GdnHCl. The  $D_{1/2}$  and  $\Delta G$  values for each variant are shown on Table 7. A similar general trend as that noted for the NT variants was seen for all CT variants, with an overall 50% decrease in fluorescence emission intensity as function of increasing [GdnHCl], accompanied by a 10-20 nm red-shift in  $\lambda_{\max}$  (Table 8). The A277C variant is ~50% labeled with AEDANS resulting in overall lower fluorescence intensity compared to the other CT variants.

TABLE 7. Denaturation of AEDANS-Labeled ApoE Variants Followed by Changes in Fluorescence Intensity

NT	D <sub>1/2</sub> (M)	ΔG kcal/mol	CT	D <sub>1/2</sub> (M)	ΔG kcal/mol
A29C	3.1	3.0	A209C	1.46	1.39
A62C	2.7	0.97	S223C	1.17	1.41
A102C	1.5	0.91	E255C	1.33	0.91
V161C	2.1	1.8	A277C	0.67	1.04

Note: D<sub>1/2</sub>: mid-point of denaturation. ΔG: free energy of unfolding

TABLE 8. Changes in λ<sub>max</sub> by GdnHCl in AEDANS-Labeled apoE NT Variants and CT Variants

ApoE single Cys variants	λ <sub>max</sub> in 0 M GdnHCl (nm)	λ <sub>max</sub> in 6 M GdnHCl (nm)	Shift (nm)
AEDANS-labeled apoE NT variants			
ApoEC112S/A29C(1-191)	481	496	15
ApoEC112S/A62C(1-191)	488	497	9
ApoEC112S/A102C(1-191)	481	494	13
ApoEC112S/V161C(1-191)	475	496	21
AEDANS-labeled apoE CT variants			
ApoEA209C(201-299)	479	497	18
ApoES223C(201-299)	478	498	20
ApoEE255C(201-299)	481	497	16
ApoEA277C(201-299)	486	496	10

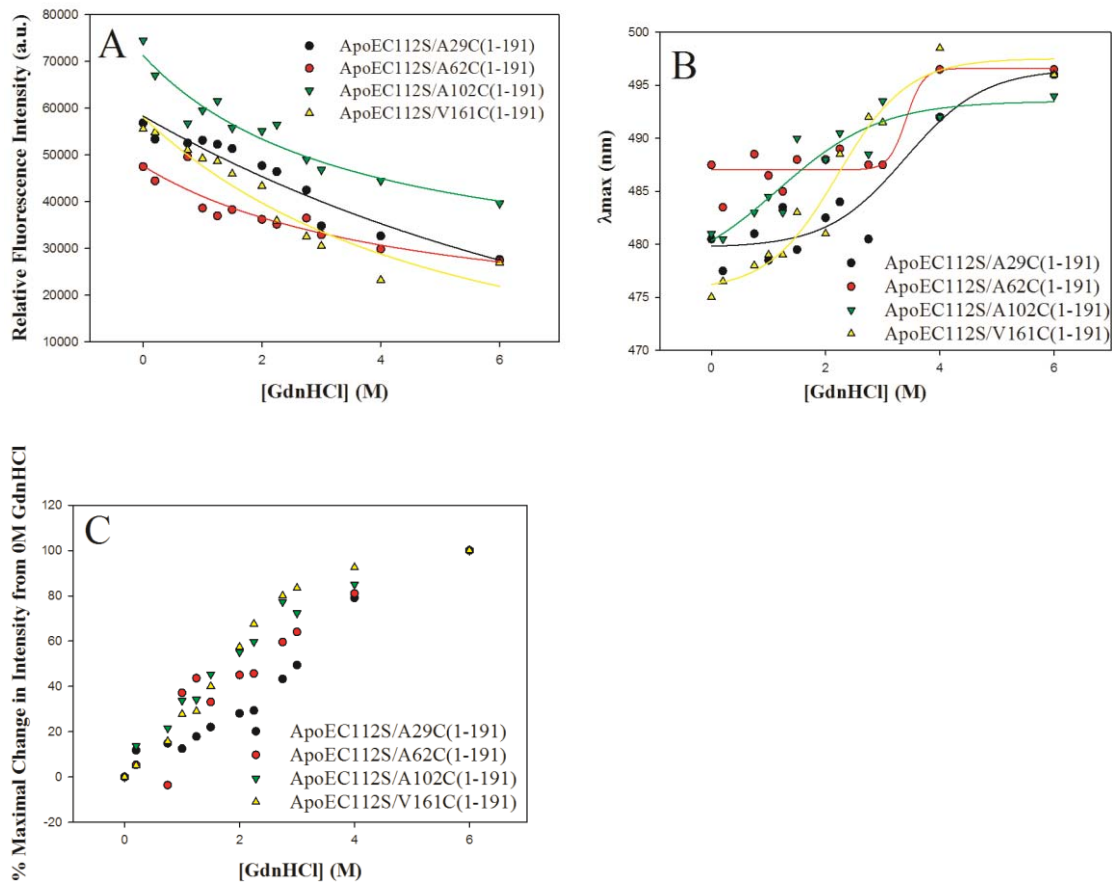


FIGURE 14. GdnHCl-induced changes in fluorescence emission characteristics of AEDANS-labeled apoE NT variants. A. Fluorescence emission spectra of 0.05 mg/ml AEDANS-labeled apoEC112S(1-191) 10 mM ammonium bicarbonate, pH 7.4, 1 mM TCEP were recorded at different concentrations of GdnHCl (as described in Figure 13). The spectra were integrated between 400 and 600 nm. The integration value, which represents the relative fluorescence intensity, was plotted as a function of [GdnHCl]. B. GdnHCl-induced change in  $\lambda_{max}$  for AEDANS-labeled NT variants. The  $\lambda_{max}$  at each concentration of GdnHCl used in Panel A was plotted versus [GdnHCl]. C. % maximal change in relative fluorescence intensity.

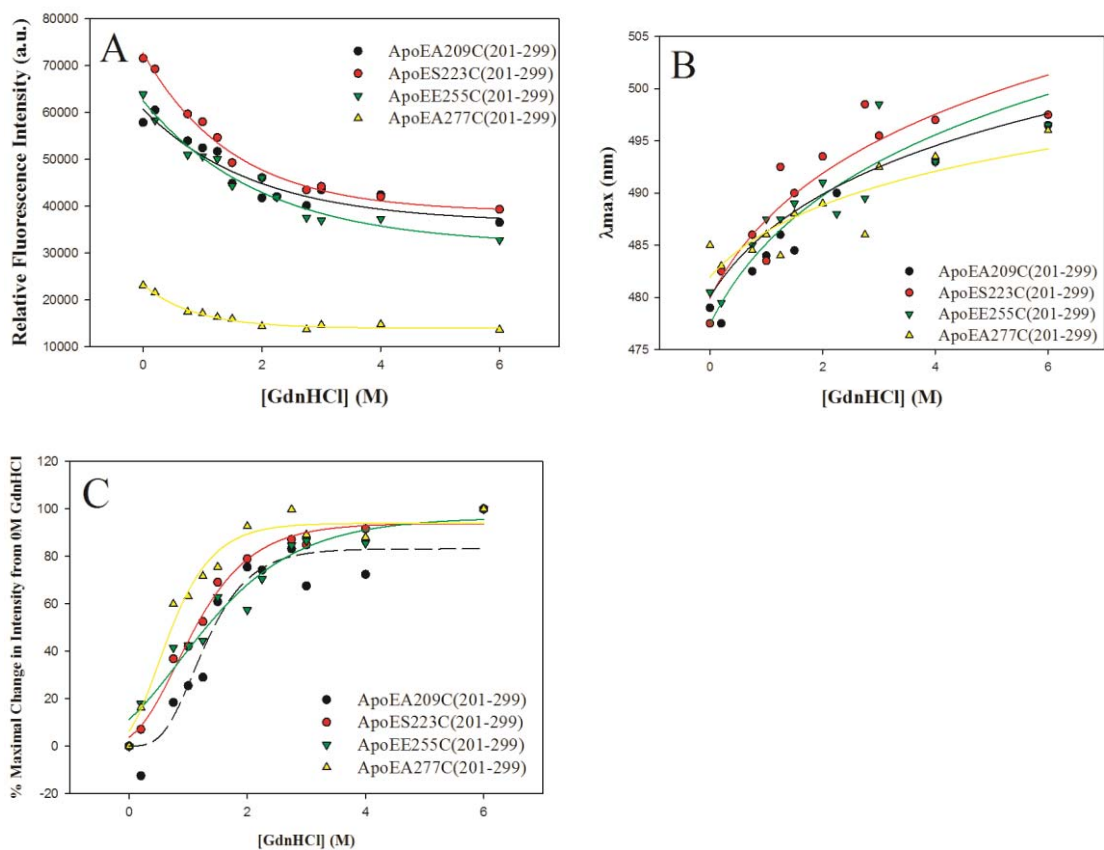


FIGURE 15. GdnHCl-induced changes in fluorescence emission characteristics of AEDANS-labeled apoE CT variants. A. Fluorescence emission spectra of 0.05 mg/ml AEDANS-labeled apoE (201-299) CT variants in ammonium bicarbonate, pH 7.4, 1 mM TCEP were recorded at different concentrations of GdnHCl and integrated between 400 and 600 nm. The integration value, which represents the relative fluorescence intensity, was plotted as a function of [GdnHCl]. B. GdnHCl-induced change in  $\lambda_{\max}$  for AEDANS-labeled CT variants. The  $\lambda_{\max}$  at each concentration of GdnHCl used in Panel A was plotted versus [GdnHCl]. C. % maximal change in relative fluorescence intensity.

## GdnHCl-Induced Denaturation of AEDANS-Labeled apoE Variants Followed by Changes in FP

FP measurements are used to study the molecular dynamics (orientation and mobility) of proteins, wherein linearly polarized light excites the covalently attached fluorescent probe; upon excitation the amount of polarized emission can be quantified and is reflective of molecular rotation and tumbling in solution of the fluorescent probe (68, 69). The population of fluorescent molecules that are photoselected are those with absorption dipole parallel to the electric field vector component of the polarized light. Polarized emission will depend on the rate of rotation that the probe underwent during its excited state lifetime. Perrin (70) first described the theory of polarization using the following equation:  $(1/P - 1/3) = (1/P_0 - 1/3) (1 + \tau/\Phi)$ , where  $P_0$  is the fundamental polarization which is close to the theoretical maximum of 0.5,  $\tau$  is the excited state lifetime of the probe and  $\Phi$  is the rotational correlation time of the probe or probe conjugated to the protein. The polarization value of a molecule is proportional to the molecules rotational relaxation time (time it takes to rotate through an angle of  $68.5^\circ$ ). Rotational relaxation time is related to hydrodynamic sphere such as proteins, rotational correlation time, where  $\eta$  is solvent viscosity,  $T$  = temperature,  $R$  = gas constant and  $V$  = molecular volume of the probe attached to the protein,  $\Phi = 3\eta V/RT$ . Thus FP is a measure of the mobility of the fluorophore and the processes that modulate them such as rotation, viscosity and molecular weight (69, 71). The magnitude of FP is dependent on the hydrated volume of the probe or probe conjugated to protein. Implicit in this process is the concept that segments with defined secondary structure such as  $\alpha$ -helix or  $\beta$ -strand would be relatively more rigid,

while unstructured flexible segments would be less rigid and more mobile (72). Therefore, when GdnHCl is added in incremental amounts, segments that bear fewer tertiary contacts and are less structured would undergo localized melting at lower [GdnHCl] compared to those segments with more tertiary contacts and more rigid structures. Although theoretical values of FP can range from -0.33 to 0.5, the measured values range from 0.01 to 0.3, with precise and reliable values obtainable with high confidence ( $FP \pm 0.002$ ). In our studies, steady-state FP measurements were carried out to assess the changes in mobility of AEDANS upon denaturation, with the rationale that unwinding of helical segments to random coil state would lead to decreases in the FP value at selected sites. AEDANS attached to different single Cys sites on apoE variants would monitor mobility of selected  $\alpha$ -helical segments of apoE NT and CT domains.

#### Unfolding of AEDANS-Labeled Single Cys apoEC112S(1-191) NT Domain Variants

Figure 16 Panel A shows the denaturation profile obtained by following GdnHCl-induced changes in FP values in the different AEDANS-labeled single Cys variants of apoEC112S(1-191) monitoring H1-H4, including the labeled WT protein apoEC112(1-191). The same data was plotted as % maximal change from 0 M GdnHCl as a function of [GdnHCl] (Figure 16, Panel B). Table 9 lists the initial FP values at 0 M GdnHCl,  $D_{1/2}$  and  $\Delta G$  values for all the NT variants. We made several interesting observations from this set of data: (i) AEDANS-labeled apoEC112S/A29C(1-191) displays a higher FP value ( $0.127 \pm 0.012$ ) at 0 M GdnHCl compared to other variants reflecting a relatively restricted mobility of H1; (ii) the variants apoEC112S/A102C and apoEC112S/V161C monitoring H3 and H4, respectively, displayed significantly lower  $D_{1/2}$  values,  $2.38 \pm$

0.43 and  $2.14 \pm 0.27$  M, respectively, compared to either apoEC112S/A29C or apoEC112S/A62C bearing probes on H1 and H2, respectively, the  $D_{1/2}$  values for which were  $3.92 \pm 0.13$  and  $3.32 \pm 0.19$  M respectively; (iii) the  $\Delta G$  value for AEDANS-labeled apoEC112S/A29C(1-191) was  $3.3 \pm 1.2$  kcal/mol, compared to A62C, A102C and V161C  $\Delta G$  values, Students two-tailed t test did not reach significance ( $P = 0.08$ ); and, lastly, (iv) whereas the  $D_{1/2}$  values obtained by monitoring the loss in overall secondary structure by CD was  $\sim 2.4$  M regardless of the location of the probe, that obtained by monitoring changes in mobility by FP spectroscopy varied depending on the location of the probe,  $P < 0.05$  (Table 9).

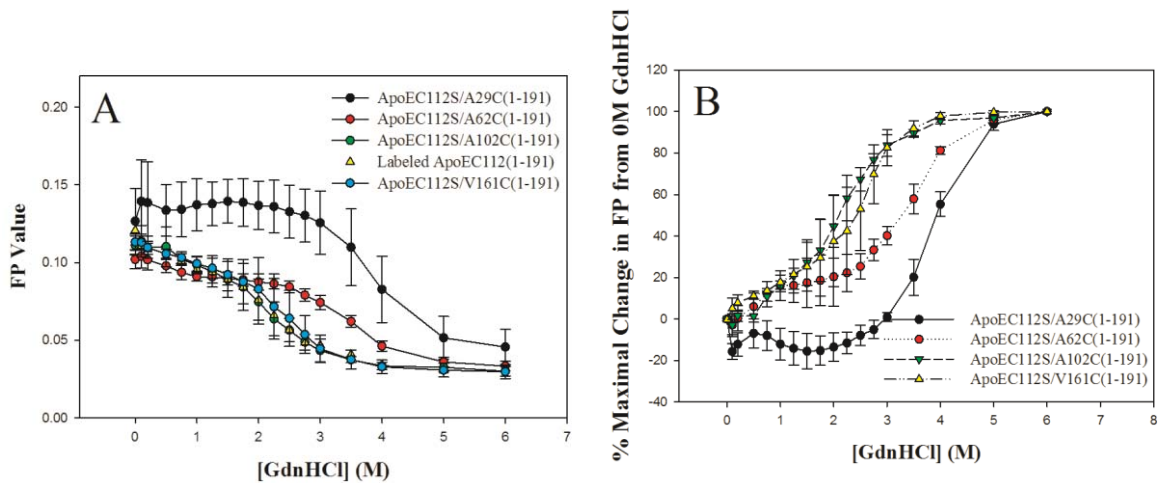


FIGURE 16. GdnHCl-induced denaturation of AEDANS-labeled apoE NT variants as monitored by change in FP values. A. FP values were recorded at 480 nm following excitation at 340 nm AEDANS-labeled NT variants (0.11 mg/ml) in ammonium bicarbonate, pH 7.4, 1 mM TCEP at different concentrations of GdnHCl. B. Plot of % maximal change in FP values versus [GdnHCl]. The data shown in Figure 16A is plotted as % maximal change in FP from 0 M GdnHCl as a function of [GdnHCl].

TABLE 9. Midpoint of Denaturation and Change in  $\Delta G$  for GdnHCl-Induced Unfolding of AEDANS-Labeled ApoE NT Constructs Measured by FP Spectroscopy

AEDANS-labeled apoE NT variants	FP values Mean $\pm$ SD (n=3)	$[D]_{1/2}$ (M) Mean $\pm$ SD (n=3)	$\Delta G$ kcal/mol Mean $\pm$ SD (n=3)
ApoEC112S/A29C(1-191)	0.127 $\pm$ 0.012 <sup>a</sup>	3.92 $\pm$ 0.13 <sup>a</sup>	3.3 $\pm$ 1.2
ApoEC112S/A62C(1-191)	0.100 $\pm$ 0.006	3.32 $\pm$ 0.19	1.8 $\pm$ 0.4
ApoEC112S/A102C(1-191)	0.111 $\pm$ 0.006	2.38 $\pm$ 0.43	1.7 $\pm$ 0.4
ApoEC112S/V161C(1-191)	0.113 $\pm$ 0.005	2.14 $\pm$ 0.27	1.8 $\pm$ 0.4
ApoEC112(1-191)WT*	0.120	2.90	1.2

<sup>a</sup>test for significance using Students two-tailed t test, significance  $P < 0.05$

\*Labeled ApoE3C112(1-191), n=1

Significantly different from A62C, A102C, V161C and WT

#### Unfolding of AEDANS-Labeled Single Cys apoE(201-299) CT Domain Variants

Figure 17 panel A shows the denaturation profile obtained by following GdnHCl-induced changes in FP values in the different AEDANS-labeled single Cys variants of apoE(201-299) CT domain. The variants monitor sites located within or in close proximity to helices C1, C2 and C3 in the CT domain, Figure 4. The same data was plotted as % maximal change from 0 M GdnHCl as a function of [GdnHCl] (Figure 17, Panel B). Table 9 lists the initial FP values at 0 M GdnHCl,  $D_{1/2}$  and  $\Delta G$  values for all the variants. The major observations with these constructs are as follows: (i) In general, all CT variants displayed a higher FP value than that elicited by NT domain constructs; this is perhaps due to the tendency of the CT domain to facilitate apoE tetramerization via helix-helix interaction. Such an interaction would yield tetramers with molecular mass

~52 kDa, which is about 2-fold higher than the 24- kDa NT domain. The isolated NT domain remains a monomer even at concentrations as high as 15 mg/ml (29). (ii) Among the CT constructs, AEDANS-labeled apoEA277C(201-299) displays a higher FP value (0.246) at 0 M GdnHCl compared to other variants reflecting a relatively restricted mobility in the segment around helix C3. Earlier studies from other lab suggest that residues 266-299 mediate apoE tetramerization (18), while previous studies from our lab indicate that the entire CT domain involving residues 201-299 mediate dimerization, with the terminal segment involving 266-299 facilitating further dimerization of the dimers (30). These studies offer support for our current observation and would explain the restricted mobility of A277. (iii) The  $D_{1/2}$  values for AEDANS-labeled A209C, S223C and E255C were 0.89 M, while that for A277C was about 2.5 fold higher, 2.45 M, suggesting that the terminal segment makes stronger tertiary contacts than the rest of the CT domain. (iv) Interestingly, the  $D_{1/2}$  values for AEDANS-labeled A209C, S223C and E255C obtained by following changes in molar ellipticity and  $\alpha$ -helical content was ~ 2-fold higher than that obtained by following change in FP values, which is an indicator of probe mobility and extent of tertiary contacts. This observation suggests GdnHCl-induced loss of tertiary contacts precedes loss of secondary structure, likely reflecting dissociation of tetramers and loss of inter-molecular helix-helix contacts prior to loss of helical structure.

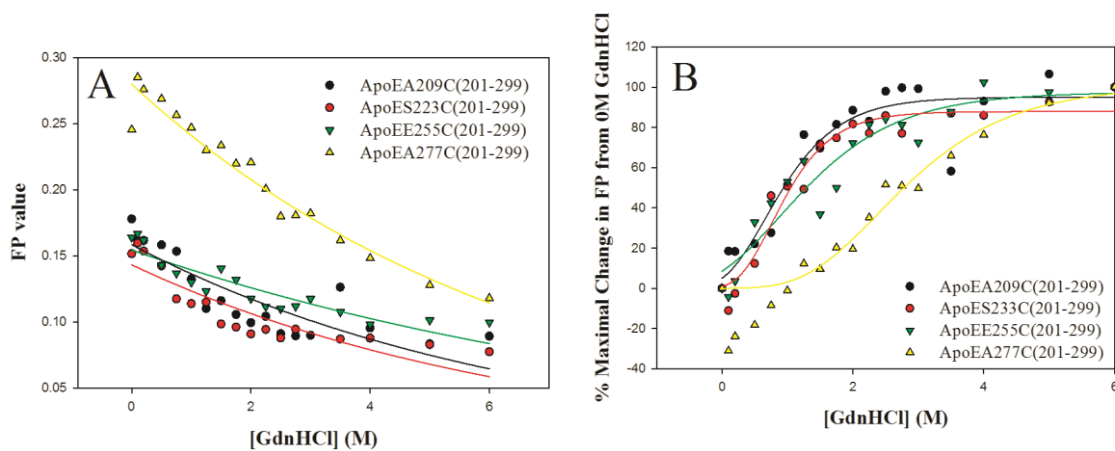


FIGURE 17. GdnHCl-induced denaturation of AEDANS-labeled apoE CT variants as monitored by change in FP values. A. FP values were recorded at 480 nm following excitation at 340 nm AEDANS-labeled CT variants (0.11 mg/ml) in ammonium bicarbonate, pH 7.4, 1 mM TCEP at different concentrations of GdnHCl. B. Plot of % maximal change in FP values versus [GdnHCl] for AEDANS-labeled apoE CT variants.

TABLE 10. Midpoint of Denaturation and Change in  $\Delta G$  for GdnHCl-Induced Unfolding of AEDANS-Labeled ApoE CT Constructs Measured by FP Spectroscopy

AEDANS-labeled apoE CT variants	FP values (n=1)	$D_{1/2}$ (M) (n=1)	$\Delta G$ kcal/mol (n=1)
ApoEA209C(201-299)	0.178	0.89	1.2
ApoES223C(201-299)	0.152	0.89	1.2
ApoEE255C(201-299)	0.164	0.89	1.4
ApoEA277C(201-299)	0.246	2.45	1.5

## Objective 2: Determine Backbone Dynamics and Solvent Accessibility with HDX coupled to MS on apoE3 NT and apoE CT domains

MS has emerged as a powerful tool in proteomics research due to its interface with gentle modes of ionization of biological samples using electrospray ionization (ESI) to convert proteins into their gas phase ions (73–76). The objective of this study was to use MS coupled to HDX to understand the amide backbone dynamics and flexibility of the NT and CT domains of apoE. Structural information can be inferred due to peptide level resolution and uptake of deuterium. It is expected that deuterium incorporation will be inversely proportional to secondary structure integrity and that it would reflect the structural rigidity or flexibility in that region. Thus, the rate of amide hydrogen exchange with deuterium will be slower with stable H-bonds in contrast to weak or transient H-bonds. Residues that are buried and inaccessible to solvent will undergo slow deuterium exchange, or minimal deuterium uptake. Loop regions, exposed surface regions, and flexible disordered regions of the protein will have higher rates of deuterium incorporation due to minimum protection of amide hydrogens. Along this reasoning, a greater extent of deuterium incorporation would be expected to occur at helices with highest flexibility and solvent accessibility.

### HDX of ApoE3(1-191) NT Domain

About 0.5  $\mu$ l of 2 mg/ml solution of apoE3(1-191) was diluted into 10  $\mu$ l of deuterated 10 mM sodium phosphate buffer (pD 7.4, 25 °C) and allowed to undergo isotopic exchange for different periods of time ranging from 30 s to 120 min to achieve labeling of the polypeptide backbone. The reaction was quenched by adding an equal volume of deuterated (1:1) phosphate buffer (pD 2.5, 50 mM TCEP) and then placed in

liquid nitrogen until further use. Following deuteration, the samples were passed through an on-line pepsin column and the resulting peptide fragments were separated on a reverse-phase column using an acetonitrile gradient (see Materials and Methods). The peptides obtained following pepsin cleavage of apoE3(1-191) were identified by MS and the identified peptides were used to construct a peptide map (Figure 18). Supplement table 16 shows total D uptake of each peptide during labeling time course. Back exchange was prevented by lowering the HDX workflow to  $\sim 0^{\circ}\text{C}$  during analysis. Of the 191 residues, 173 were identified with several overlapping peptides, leading to a robust sequence coverage of 91%.

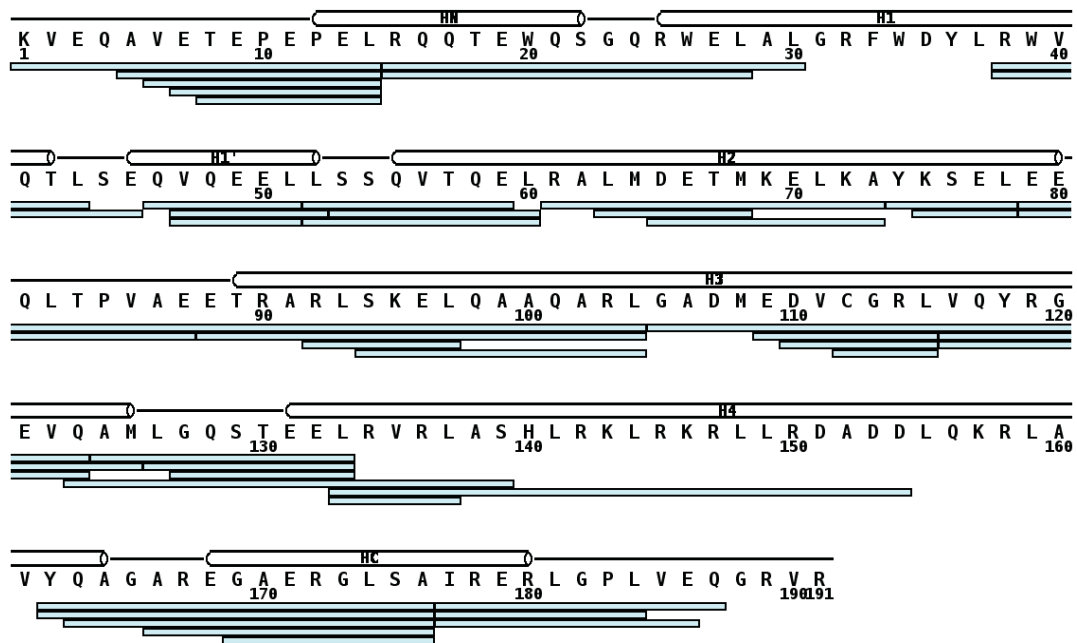


FIGURE 18. Peptide fragments obtained following on-line pepsin digestion of apoE3(1-191) at pD 2.5. The amino acid sequence of apoE3(1-191) (without the His-tag) is shown in one letter code. Each blue bar represents a peptide that was identified by MS. The secondary structure from NMR PDB 2KC3 is shown above the sequence with cylinders representing helices: HN (P12-S22), H1 (R25-T42), H1' (E45-L52), H2 (Q55-E80), H3 (T89-M125), H4 (E131-A164) and HC(E168-R180).

TABLE 11. Peptides Derived from Peptic Digestion of apoE3(1-191)

Peptide#	Amino Acid Position		Sequence	Predicted Average Mass (Da)	Peptide Length	Number of Amide hydrogens
1	1	14	KVEQAVETEPEPEL	1597.7	14	11
2	15	30	RQQTEWQSGQRWELAL	2016.1	16	15
3	46	51	QVQEEL	744.7	6	5
4	52	60	LSSQVTQEL	1004.0	9	8
5	61	73	<b>R</b> ALMDE <b>T</b> M <b>K</b> ELKA	1535.8	13	12
6	74	78	YKSEL	638.7	5	4
7	79	87	EEQLTPVAE	1015.0	9	7
8	92	97	RLSKEL	744.8	6	5
9	94	104	SKELQAAQARL	1214.3	11	10
10	105	123	GADMEDVCGRLVQYRGEVQ	2125.3	19	18
11	126	133	LGQSTEEL	875.9	8	7
12	133	137	LRVRL	655.8	5	4
13	133	154	LRVRLASHLRKLRKRLLRDADD	2701.1	22	21
14	162	176	YQAGAREGAERGLSA	1535.6	15	14
15	177	187	IRERLGPLVEQ	1309.5	11	9

Note: The sequence, length, predicted mass of undeuterated peptides are shown. Also shown is the number of exchangeable amide hydrogens; the peptides shown in this Table were used for Protection Plot analysis, Figure 19. Average isotopic mass takes into account all major isotopes of the elements. Bold letters denote sites of AEDANS attachment for fluorescence spectroscopy.

Table 11 displays peptide length and total amount of exchangeable amide hydrogens on each peptide from apoE3(1-191). The peptides covered the entire length of the NT domain. The mass of each peptide was identified using MassLynx<sup>TM</sup>, a data acquisition software used to transform data to usable results. The centroid  $m/z$  peak of each isotopic envelope taken from each mass spectra was used to calculate the peptide mass and thus deuterium uptake. We used an HDX application-specific software (DynamX) to visualize, sort, and display HDX data. After data output, user input was used to complete

analysis and to assess quality control of HDX results. The number of exchanged hydrogens ( $H_x$ ) in each peptide was calculated using the molecular mass of the undeuterated species ( $M$ ) and the measured mass of the partially deuterated species ( $M_D$ ), equation 2. Percent deuterium content (% D) incorporation of each peptide was calculated as shown by equation 3, where  $N$  is the total number of amide hydrogens on each peptide.

$$H_x = M_D - M [2]$$

$$\%D = H_x/N \times 100 [3]$$

### D Uptake Plots for apoE3(1-191)

Uptake plots (D uptake vs Log Exchange time (min)) were generated for peptides numbered 1-15 obtained from apoE3(1-191) (Figure 19, 20, 21). Empty circles ( $\circ$ ) represent the experimental peptide labeling with deuterium as a function of time. Filled circles ( $\bullet$ ) represent the reference curve indicating the summed exchange behavior expected for that peptide in the unprotected random coil state; it is calculated from published data of known rate constants of each amino acid in the uncoiled state (77). The reference curve is drawn as a stretched exponential:  $D = N(1 - e^{(-kt)^\beta})$  where  $D$  = D uptake,  $N$  = number of amide hydrogens,  $k$  = rate constant,  $t$  = time of exchange,  $\beta$  = stretching factor, since any given stretch of amino acids exchange over a range determined by neighboring amino acids,  $\beta$  modifies the exponential curve to reduce biased amino acid composition. A parameter known as protection factor (Pf) is calculated for each peptide by comparing the rate constant of each measured kinetic phase from data obtained with the reference curve for that sequence (78). Positive Log Pf values are indicative of relatively low % D uptake while negative values indicates higher

uptake (Table 12). A range from -3 to 0 was seen for all peptides except peptides 46-51 and 133-154 which show Pf values greater than zero which is indicative of high protection (or lower total D uptake).

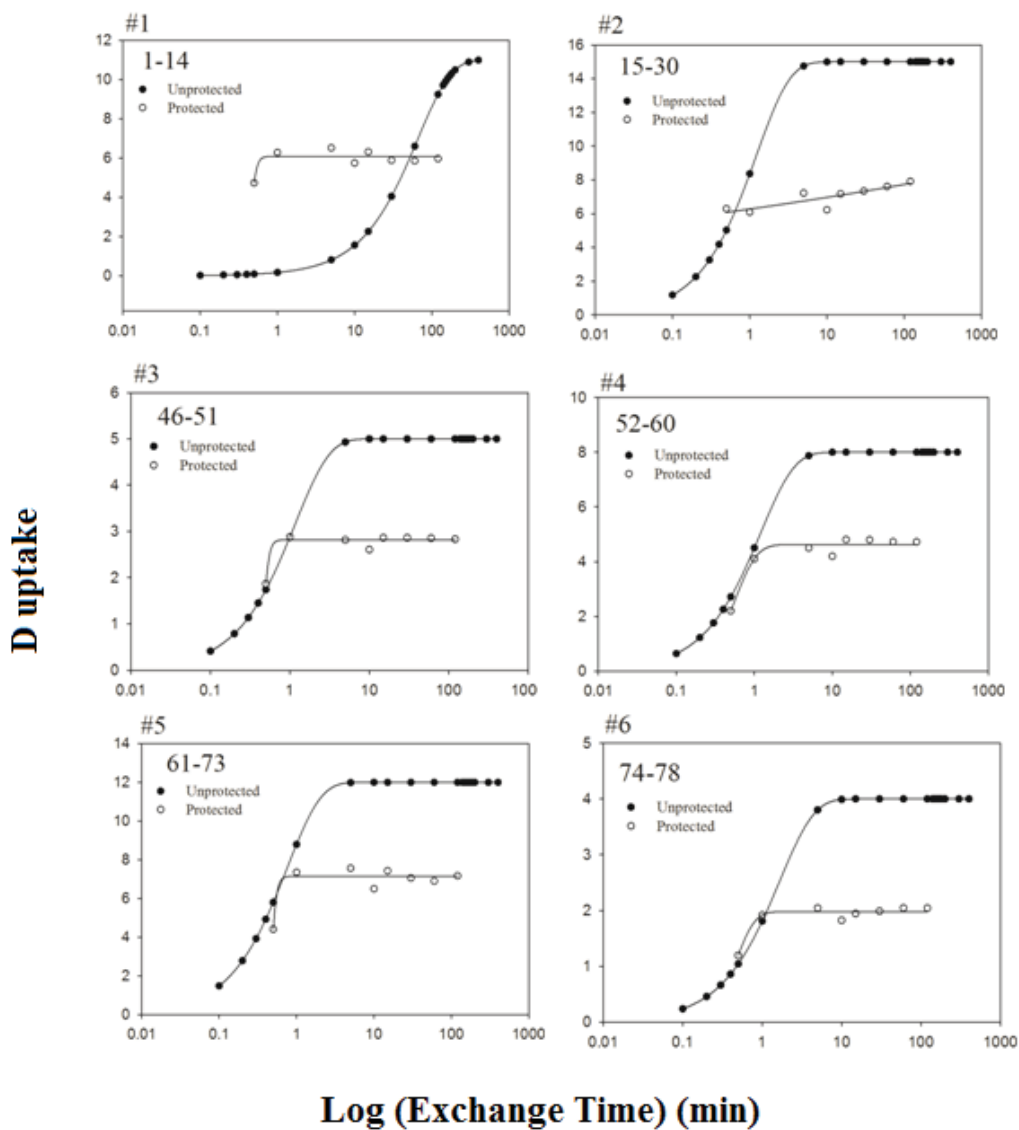


FIGURE 19. Uptake plots of apoE3(1-191) peptic digest peptides region 1-78. Deuterium incorporation was measured at 0.5, 1, 5, 10, 15, 30, 60, and 120 min for each peptide. Filled circles (●) represent the predicted uptake computed for an unprotected peptide in an unfolded random coil state. Empty circles (○) represent the experimental peptide labeling with deuterium as a function of time.

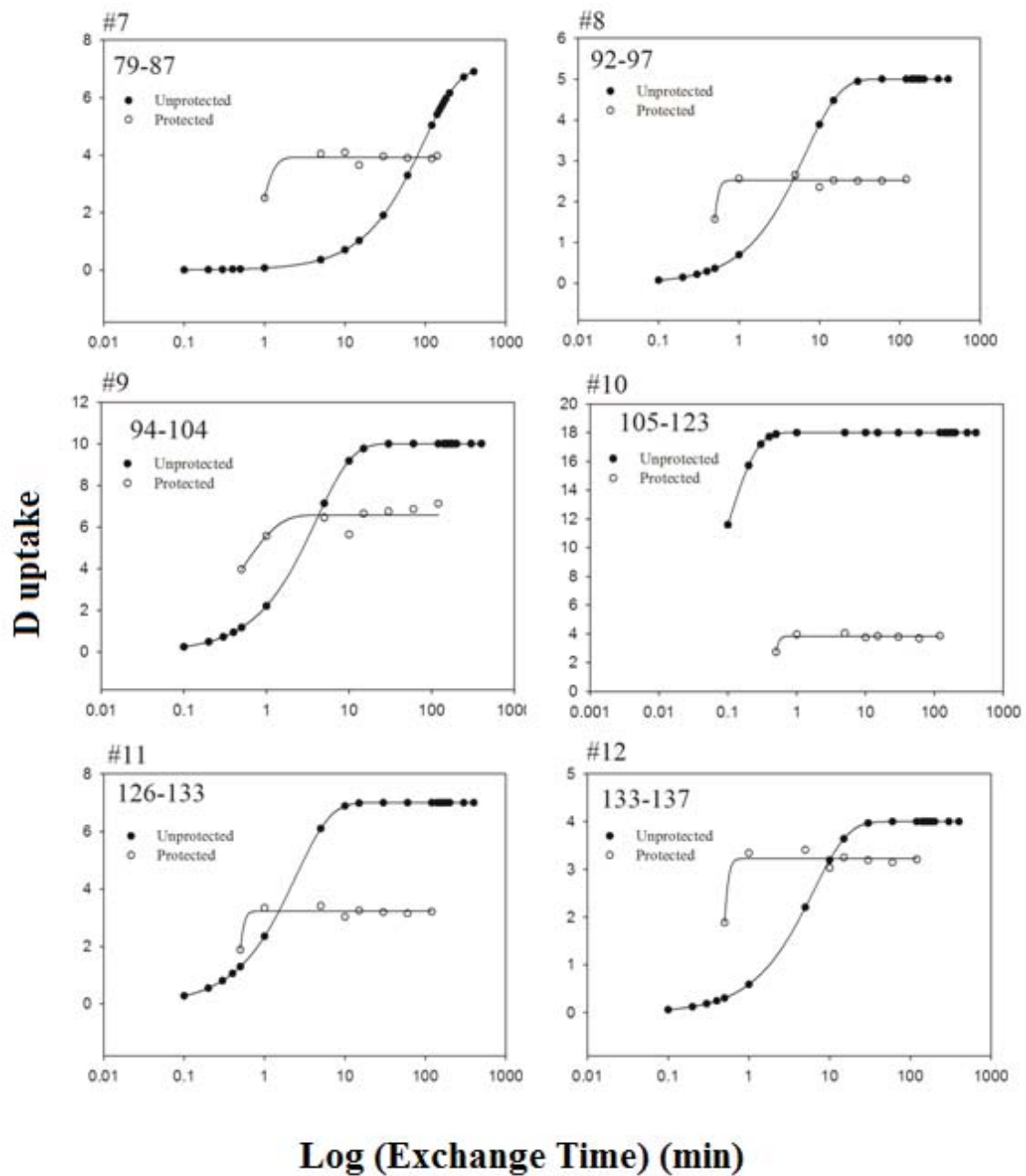


FIGURE 20. Uptake plots of apoE3(1-191) peptic digest peptides region 79-137. Deuterium incorporation was measured at 0.5, 1, 5, 10, 15, 30, 60, and 120 min for each peptide. Filled circles (●) represent the predicted uptake computed for an unprotected peptide in an unfolded random coil state. Empty circles (○) represent the experimental peptide labeling with deuterium as a function of time.

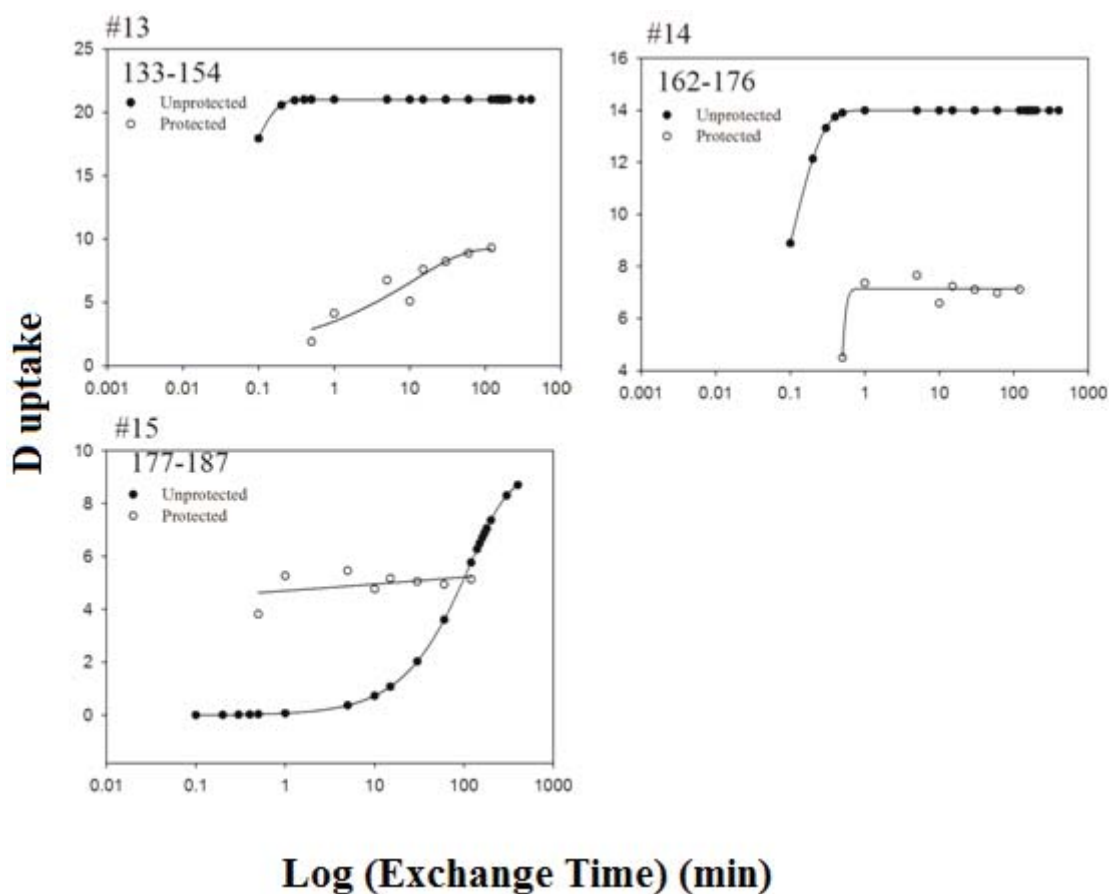


FIGURE 21. Uptake plots of apoE3(1-191) peptic digest peptides region 133-187. Deuterium incorporation was measured at 0.5, 1, 5, 10, 15, 30, 60, and 120 min for each peptide. Filled circles (●) represent the predicted uptake computed for an unprotected peptide in an unfolded random coil state. Empty circles (○) represent the experimental peptide labeling with deuterium as a function of time.

TABLE 12. Kinetic Data and Pf for HDX of apoE3(1-191) Peptides

Peptide #	Amino Acid Position		Sequence	$k_1$ (min <sup>-1</sup> )	$k_2$ (min <sup>-1</sup> )	Pf	Log (Pf)	%D range
1	1	14	KVEQAVETEPEPEL	0.019	21	0.0009095	-3.0	43-54
2	15	30	RQQTEWQSGQRWELAL	0.816	4.2x10 <sup>-9</sup>	1.9x10 <sup>8</sup>	8.3	42-53
3	46	51	QVQEEL	0.86	0.22	3.9	0.59	37-57
4	52	60	LSSQVTQEL	0.83	3.5	0.24	-0.63	28-59
5	61	73	RALMDETMKELKA	1.6	22	0.08	-1.12	37-60
6	74	78	YKSEL	0.60	5.3	0.11	-0.95	30-51
7	79	87	EEQLTPVAE	0.011	4.4	0.00	-2.62	36-57
8	92	97	RLSKEL	0.11	0.19	0.56	-0.25	31-51
9	94	104	SKELQAAQARL	1.3	1.9	0.69	-0.16	40-71
10	105	123	GADMEDVCGRLVQYRGEVQ	10	4	2.58	0.41	15-21
11	126	133	LGQSTEEL	0.41	0.51	0.80	-0.10	27-46
12	133	137	LRVRL	0.16	0.20	0.80	-0.10	47-62
13	133	154	LRVRLASHLRKLRKRLLRDADD	19	0.037	522	2.72	9-44
14	162	176	YQAGAREGAERGLSA	10	22	0.45	-0.34	32-51
15	177	187	IRERLGPLVEQ	0.011	22	0.00051	-3.3	43-57

$k_1$ : predicted rate constant for the random coil state

$k_2$ : rate constant for the experimental D uptake

Pf: protection factor  $k_1/k_2$

% D range: percent D at initial and last time point

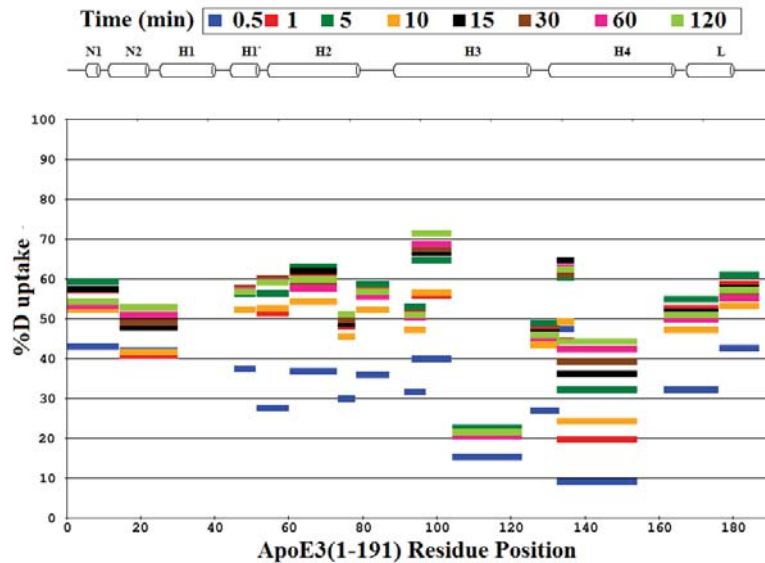


FIGURE 22. Protection plot of apoE3(1-191) peptide fragments. %D uptake of each peptide is shown as a function of time is shown for all peptides. Each time-point is color coded as shown on top. Amino acid position is shown along the X-axis. A schematic representation of secondary structure of apoE3(1-183) derived from NMR structure (PDB 2KC3) is shown on top.

### Protection Plot of apoE3(1-191) Peptide Fragments

HDX data was compiled and analyzed using on-line software MSTools (79), the % D uptake was compared for all peptide fragments using a protection plot (Figure 22) where the X-axis covers the residue position in the protein and the Y-axis is the %D uptake. Peptides are color coded with respect to each time point and presented as horizontal bars. Figure 22 also shows the helix boundaries of apoE3(1-183) based on the NMR structure, depicting helices H1-H4. On the protection plot peptides spanning residues 1-100 and 162-187 show an increase in % D uptake in the initial 30 s (blue bar), and reaches equilibrium with 50-60% incorporation after 1-2 h (pink and light green bars, respectively). Peptides spanning 105-154 had the lowest average amount of % D uptake suggesting protection from solvent. Figure 23 represents HDX information that is

superimposed on the NMR structure of apoE3(1-183) (PDB 2KC3). Residues corresponding 1-100 are encompassed in helices HN, H1, H2 and a portion of H3 are shown as green helices. Residues 105-154 encompass parts of H3 and H4 and are colored blue on Figure 23. It is seen that there is a large variability in the susceptibility to HDX between helices in the helix bundle and within each helix. Differences in %D incorporation could be attributed to fluctuations and flexibility within the helices as well as solvent accessible sites.

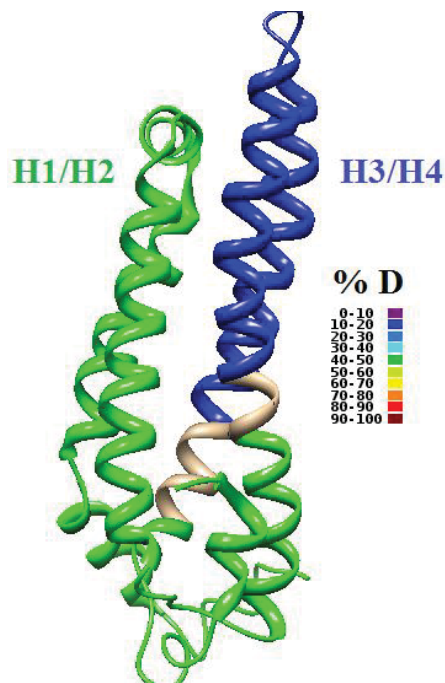


FIGURE 23. % D incorporation superimposed on the NMR structure of apoE3(1-183) (PDB 2KC3). The protein model is shaded according to %D at 10 min of labeling. Helices are shown in ribbon form. Royal blue represents 10-20% incorporation while light green represents 50-60% incorporation. Grey represents segments for which there is no data.

## HDX of apoE(201-299) CT Domain

HDX analysis for apoE(201-299) CT domain was carried out using the same methodology as described above for apoE3(1-191) NT domain. A master list of peptides produced upon pepsin digestion of apoE(201-299) is shown in Figure 24. From this list, we chose 19 peptides that would cover most of the CT domain and remain an accurate reflection of HDX/MS dynamics (Table 12). We obtained MS information on 84 of the 99 residues of apoE(201-299), yielding 85% linear sequence coverage with several overlapping peptides. Table 12 shows each peptide with the predicted average mass, amino acid length and total amount of exchangeable amide-hydrogens.

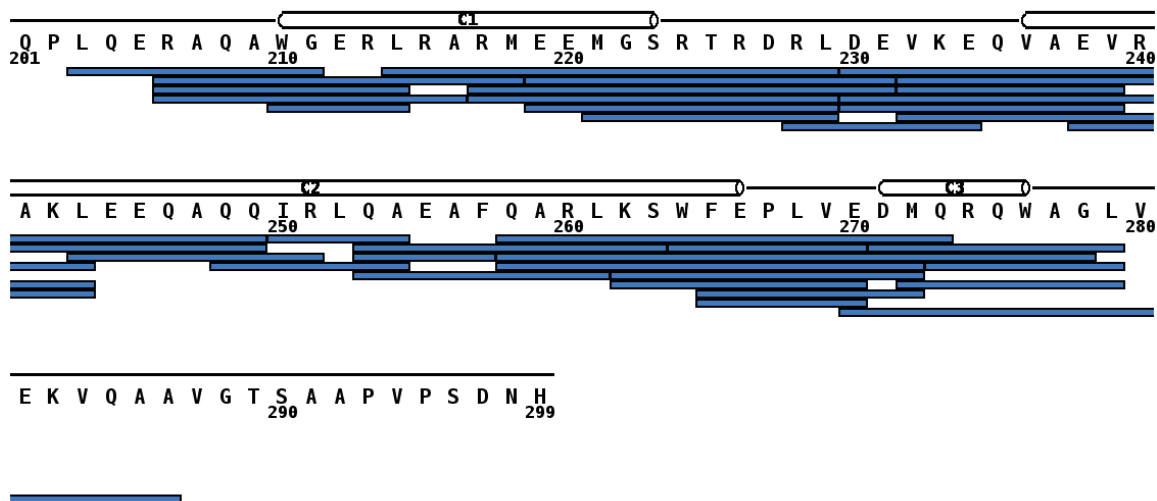


FIGURE 24. Peptide fragments obtained following on-line pepsin digestion of apoE(201-299) at pD 2.5. The amino acid sequence of apoE(201-299) (without the His-tag) is shown in one letter code. Each blue bar represents a peptide that was identified by MS. The secondary structure from NMR structure of monomeric apoE3(1-299) (PDB 27LB) is shown above the sequence with cylinders representing helices. The helices are numbered C1 (W210-S223); C2 (V236-E266) and C3 (D271-W276). Of the 99 residues, 84 were identified, leading to sequence coverage of 85%.

TABLE 12. Peptides derived from peptic digestion of apoE(201-299)

Peptide #	Amino Acid Position		Sequence	Predicted Ave Mass (Da)	Peptide Length	Amide Hydrogens
1	206	214	RAQAWGERL	1086.2	9	8
2	206	216	RAQAWGERLRA	1313.5	11	10
3	206	218	RAQAWGERLRAR	1600.8	13	12
4	217	229	RMEEMGSRTRDR	1636.9	13	12
5	217	231	RMEEMGSRTRDR	1881.1	15	14
6	219	229	EEMGSRTRDRL	1349.5	11	10
7	219	231	EEMGSRTRDRLD	1593.7	13	12
8	230	249	DEVKEQVAEVRA	2327.5	20	19
9	232	243	VKEQVAEVRACL	1369.6	12	11
10	232	249	VKEQVAEVRACL	2083.3	18	17
11	250	254	IRLQA	599.7	5	4
12	253	261	QAEAFQARL	1033.1	9	8
13	253	263	QAEAFQARLKS	1248.4	11	10
14	262	270	KSWFEPLVE	1134.3	9	7
15	262	272	KSWFEPLVEDM	1380.6	11	9
16	265	270	FEPLVE	732.8	6	4
17	265	272	FEPLVEDM	979.1	8	6
18	271	279	DMQRQWAGL	1104.2	9	8
19	272	279	MQRQWAGL	989.2	8	7

Note: The sequence, length, predicted mass of deuterated peptides are shown. Also shown is the number of exchangeable hydrogens; the peptides shown in this Table were used for Protection Plot analysis. Average mass takes into account all major isotopes of the elements. Bold letters denote sites of AEDANS attachment for fluorescence spectroscopy.

#### D Uptake Plots for apoE(201-299)

Uptake plots of representative peptides from apoE(201-299) CT domain are shown in Figure 25, 26. Each plot shows two curves representing predicted uptake for the unprotected random coil state and the actual uptake observed by experimental means. Table 13 lists the rate constants for representative CT peptides. The reference curve (●) was obtained following the same procedures for the apoE(1-191) peptides (77). The Pf

was calculated as described for apoE3(1-191) (Table 13). Empty circles (○) represent the experimental peptide labeling with deuterium as a function of time.

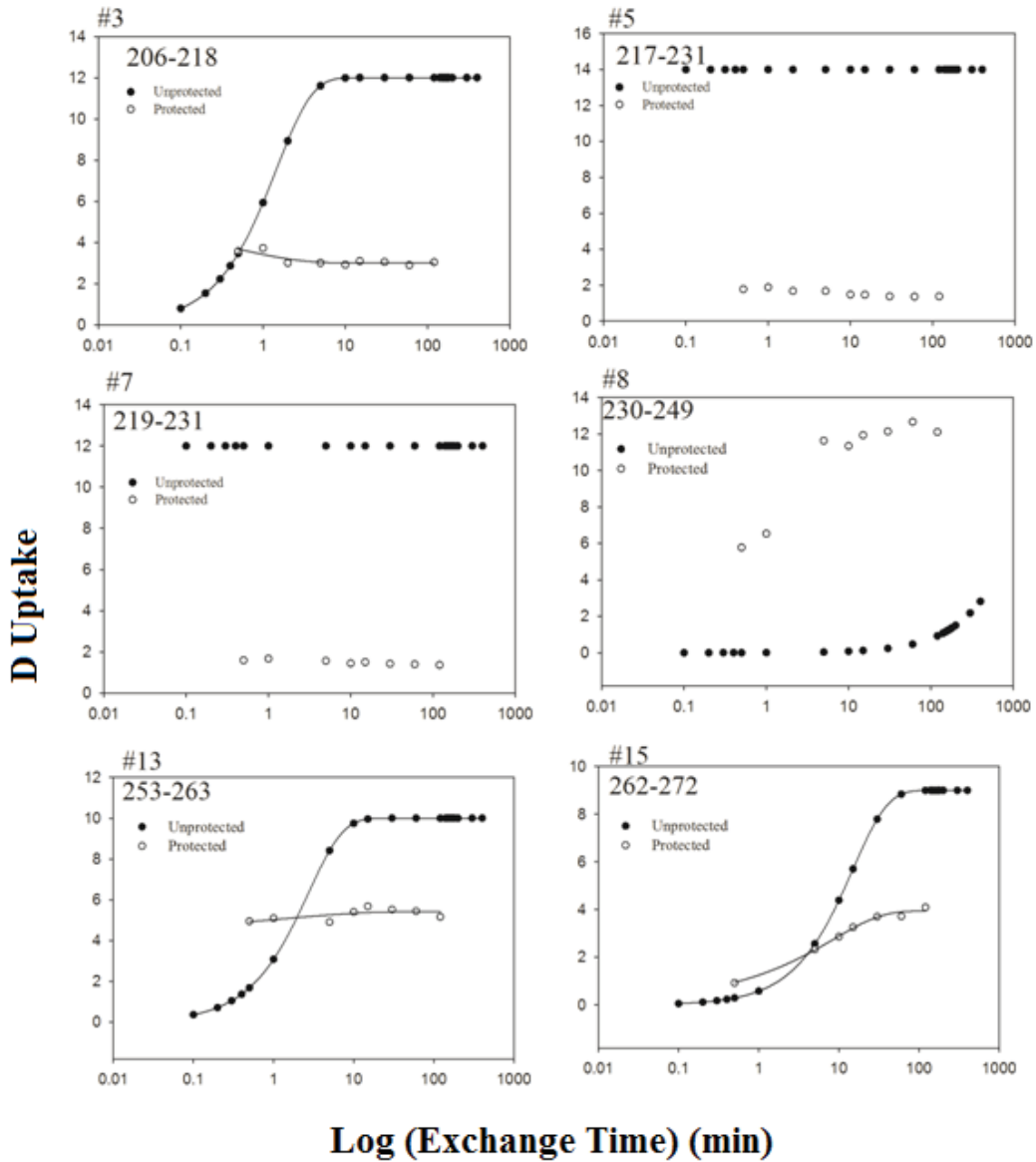


FIGURE 25. Uptake plots of apoE3(201-299) peptic digest peptides region 206-272. Deuterium incorporation was measured at 0.5, 1, 5, 10, 15, 30, 60, and 120 min for each peptide. Filled circles (●) represent the predicted uptake computed for an unprotected. Empty circles (○) represent the experimental peptide labeling with deuterium as a function of time.

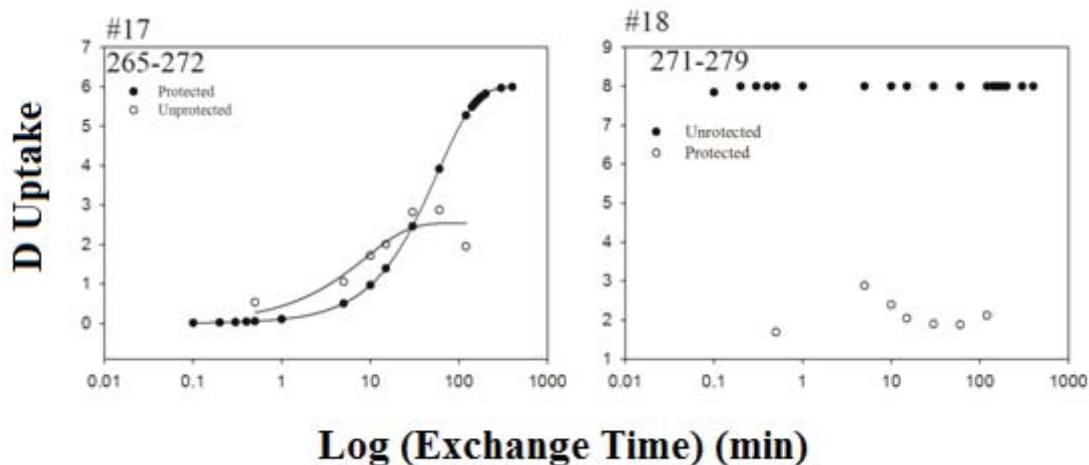


FIGURE 26. Uptake plots of apoE3(201-299) peptic digest peptides region 265-279. Deuterium incorporation was measured at 0.5, 1, 5, 10, 15, 30, 60, and 120 min for each peptide. Filled circles (●) represent the predicted uptake computed for an unprotected. Empty circles (○) represent the experimental peptide labeling with deuterium as a function of time.

TABLE 13. Kinetic Data and Protection Factor for apoE(201-299) Peptides

Peptide #	Amino Acid Position		Sequence	$k_1$ (min <sup>-1</sup> )	$k_2$ (min <sup>-1</sup> )	Pf	Log (Pf)	%D range
3	206	218	RAQAWGERLRARM	0.9	4.0	0.21	-0.67	25-31
5	217	231	RMEEMGSRTRDRLDE	417.0	2.0	208.50	2.32	10-13
7	219	231	EEMGSRTRDRLDE	1000	2	500.00	2.70	11-14
8	230	249	DEVKEQVAEVRAKLE EQAQQ	0.000 0	1.0	0.00	-5.08	48- 100
15	262	272	KSWFEPLVEDM	0.10	0.06	1.59	0.20	10-46
17	265	272	FEPLVEDM	0.027	0.09	0.29	-0.53	9-32
18	271	279	DMQRQWAGL	0.492	2.00	0.25	2.70	21-27

$k_1$ : predicted rate constant in random coil state

$k_2$ : rate constant for the experimental D uptake

Pf: protection factor  $k_1/k_2$

% D range: percent uptake at initial and ending labeling times

For peptides 5, 7, 15, and 17 the rate constants are lower than the predicted rate constant ( $k_1$ ) of the uncoiled state. This suggests that the peptide backbone is likely to adopt a rigid  $\alpha$ -helical structure; however, for peptides 3, 8, and 18 the calculated rate constants ( $k_2$ ) are much higher than  $k_1$  for the uncoiled state which likely adopts a flexible  $\alpha$ -helical structure.

#### Protection Plot of apoE(201-299) Peptide Fragments

The HDX data for all the apoE(201-299) CT domain peptides were compiled and the %D uptake shown as a protection plot as a function of time in Figure 27. Peptides are color coded with respect to each time point and presented as horizontal bars. Figure 29 also shows the helix boundaries of apoE(201-299) based on the apoE3(1-299) NMR structure, depicting helices C1, C2, and C3. Residues 203-230 can be seen as having ~10-30% D uptake after 2 h and can be regarded as being protected from solvent. A lower extent of protection is evident in residues 230-260 with ~40-60% D uptake compared to the rest of the sequence, indicative of increased solvent accessibility. Interestingly residues 260-277 showed high % D uptake initially suggesting a dynamic structure for this segment and shifted to lower %D at later time points. This observation is agreement with previous studies from other labs (80) and our lab (32) which suggest that the terminal region of the CT domain is likely to be flexible in order to achieve large rearrangements and accommodate new conformations when oligomerization of the protein takes place.

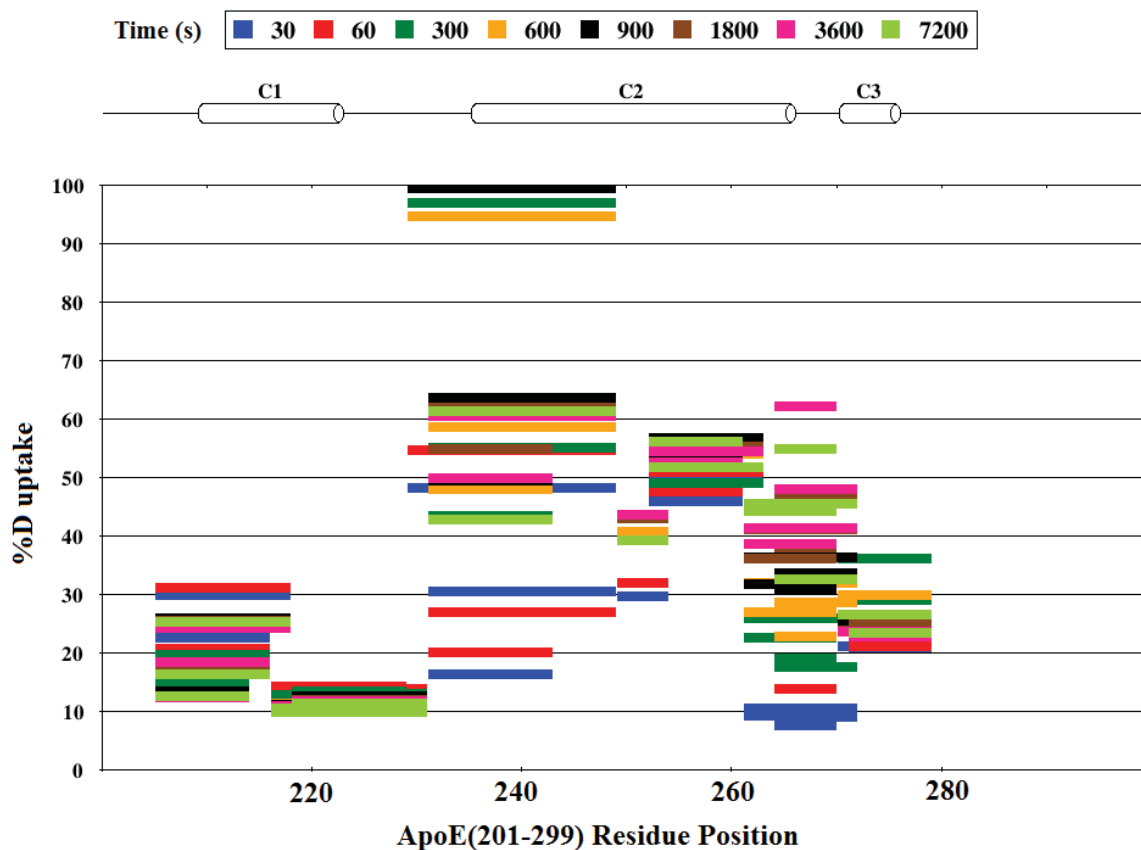


FIGURE 27. Protection plot of apoE(201-299). %D uptake of each peptide as a function of time for all peptides. Each time-point is color coded as shown on top. Amino acid position is shown along the X-axis. A schematic representation of secondary structure of apoE(201-299) derived from the NMR structure of apoE(1-299) (PDB 2L7B) is shown on top. It is important to bear in mind that the NMR structure was solved using a monomeric form of apoE wherein 5 residues were substituted to prevent oligomerization (W264R, F257A, V269A, L279Q, V287E).

## CHAPTER 4

### DISCUSSION

The primary objective of this study was to examine the mechanism of unfolding of the N-terminal and C-terminal domain of apoE3, with the long-term goal of understanding the conformational reorganization that occurs during lipid interaction. The availability of high-resolution structural information of apoE3 NT domain by X-ray crystallography and NMR spectroscopy, and of the monomeric unit of apoE3 by NMR spectroscopy allowed us to develop testable hypothesis using a combination of HDX/MS and fluorescence spectroscopy. ApoE3 has been extensively studied in its lipid-free and lipid-bound form (25, 58, 81, 82) with several lines of evidence indicating that the protein undergoes lipid-induced helix bundle opening of the NT domain and conformational reorganization of the CT domain. However, we currently lack understanding of the precise mechanism of these conformational alterations. The data obtained from the present study seek to fill this gap in knowledge by offering fine details regarding the thermodynamics of unfolding of isolated apoE3 domains.

Previous studies from our lab and other labs set the stage for the current study with regard to the NT domain of apoE3:

(i) It is highly stable, with a  $[GdnHCl]_{1/2}$  of 2.5 M,  $\Delta G = \sim 8-9$  kcal/mol, as established by CD spectroscopy (16); this approach gives a global picture during unfolding following loss in overall secondary structure. Table 16 displays exchangeable

reversible lipid binding proteins and their stabilities. ApoE in humans and rat have higher  $D_{1/2}$  and  $\Delta G$  compared apoA and apoC. Insect apolipoprotein III share an overall topology and structure to apoE however, these proteins have five helices and have much lower global stabilities (Table 15).

TABLE 15. Free Energy of Unfolding of Exchangeable Apolipoproteins

Protein	$D_{1/2}$ (M)	$\Delta G$ kcal/mol	Reference
human ApoA-IV	0.4	0.02	(83)
human ApoA-II	0.6	1.0	(84)
human ApoE CT	0.7	3.9	(16)
human ApoA-I	1.0	4.2	(85)
human ApoC-II	1.1	2.8	(86)
human ApoE3 NT	2.5	8.0	(21)
human ApoE2	2.7	8.5	(21)
human ApoE3	2.5	10.5	(16)
human ApoE4	1.6	3.5	(21)
rat apoE	2.5	8.0	(56)
Insect apoLpIII			
<i>Manduca sexta</i>	0.4	1.3	(87)
<i>Galleria mellonella</i>	0.3	2.4	(88)
<i>Bombyx mori</i>	0.3	2.5	(89)
<i>Locusta migratoria</i>	0.6	2.4	(90)

(ii) It is composed of a helix bundle made up of 4 long amphipathic  $\alpha$ -helices (H1 – H4) whose hydrophobic side faces the protein interior making stable helix-helix contacts, while the polar sides face the aqueous environment as seen by X-ray crystallography and NMR spectroscopy; additionally there is a short helix (H1') (linking H1 and H2) that is almost perpendicular to the helix bundle axis. Further, NMR studies indicate the presence of additional flexible helices not noted by X-ray analysis, likely due to their flexibility, such as helix N spanning residues 12-22, helix C, residues 168-180

which are believed to make extensive contacts with the helix bundle (residues 24-164) (47).

(iii) It is monomeric as noted by sedimentation equilibrium and gel filtration studies (5, 16)

(iv) It is stabilized by a hydrophobic core, which drives bundle formation along with buried H-bonds and salt bridges (Table 16).

TABLE 16. Buried H-bonds, Salt Bridges, and Leucine Zipper Residues found in ApoE3 (1-183) NT Domain from PDB 2KC3

Helices	H2	H3
H1	*W26 <sup>b</sup> -E70 <sup>s</sup> ; *R25 <sup>b</sup> -E70 <sup>s</sup> #L30 <sup>b</sup> -T67; #Y36-E59	N/A
H4	N/A	*L144 <sup>b</sup> -D107 <sup>s</sup> ; *D107 <sup>s</sup> -R147 <sup>s</sup> ; *D107 <sup>s</sup> -L148 <sup>b</sup> ; *S94 <sup>s</sup> -E179 <sup>s</sup> ; #D151-A100 <sup>b</sup> ; #D151-L104 <sup>b</sup> ; #R158-E96
Leucine zipper		
helix 4	<sup>a</sup> 130-TEELRVRLASHLRKLRKRLLRDADDLQKRLAVYQ-163	
helix 3	<sup>a</sup> 89-TRARLSKELQAAQARLGADMEDVCGRLVQYRGEVQAML-126	

<sup>#</sup> Salt-bridges (24)

<sup>\*</sup> H-bonds (47)

<sup>b</sup> backbone atom

<sup>s</sup> side chain atom

<sup>a</sup>abcdef: a and e are Leucine

(v) Competition binding assays for the LDLr revealed that the apoE3 NT domain, which harbors the LDLr binding site, is able to compete effectively with the intact protein for binding to the LDLr (52). The protein is required to bind to lipids enabling precise presentation of ligand to the LDLr (17). Lipid binding involves opening of the helix

bundle to reveal hydrophobic interior that facilitates lipid interaction as revealed by engineered disulfide bridge pairing of helices that prevent lipid binding as measured by turbidimetric lipid clearing assays (62). Further, FRET analysis indicates that H4 moves away from H1 and H2 upon GdnHCl induced denaturation. Together these studies indicate that the NT domain opens via disruption of helix-helix interactions.

(vi) Upon interaction with DMPC vesicles, apoE3 NT domain transforms the vesicular bilayer structure to form discoidal complexes as revealed by electron microscopy (62). The complexes form a belt-like structure. In this lipid-bound state, the helical axis appears to be oriented perpendicular to the plane of the bilayer, as inferred by attenuated total reflection-Fourier transformed infrared (FTIR-ATR) spectroscopy and the hydrophobic interior faces the fatty acyl chains of the phospholipids (61).

Thus, with regard to the NT domain, it is not known how such a stable helix bundle structure opens, and, further, what is the order of opening? Is it like an umbrella opening- i.e., all helices abruptly become separated in space or like peeling a banana – i.e. one helix at a time or like opening book, with H1/H2 moving away from H3/H4 (Figure 28).

Much less is known with regard to the CT domain. Information about the oligomeric properties of apoE CT domain was obtained from truncation studies where it was

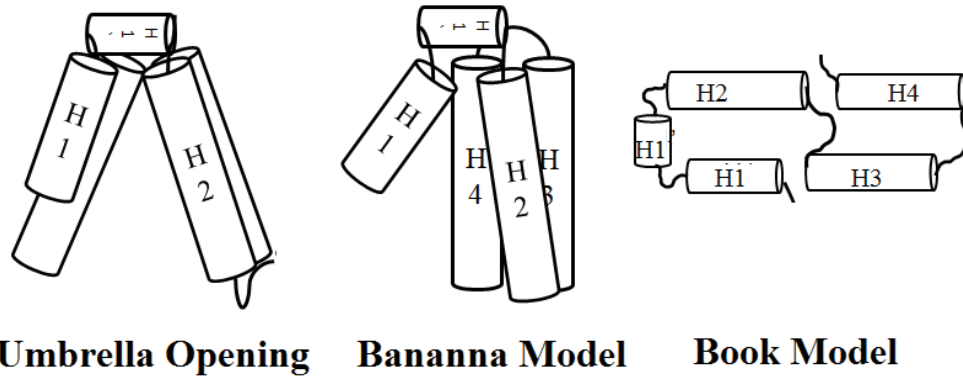


FIGURE 28. ApoE3 (1-191) ordered helix unfolding models.

determined that deleting residues 244-299 will prevent apoE from forming tetramers. ApoE CT truncated proteins were shown to partially bind VLDL thus giving functional evidence for the role of residues 244-280 not only in oligomerization but also in lipoprotein binding (43). It was soon determined that five key residues (F257, W264, V269, L279, V287) were needed for self-association; substitutions of these residues to polar amino acids allowed the C-terminal domain to form monomeric species (31). Previous fluorescence spectroscopic studies from our lab indicated that the entire CT domain makes inter-molecular contact with CT domain residues from a neighboring molecule, which lead to a model wherein two apoE molecules form a dimer and further dimerize via the terminal residues (266-299) to form a tetramer (80). Furthermore, early studies established that in contrast to the highly stable NT domain, the unfolding parameters of apoE CT domain are in the range observed for other exchangeable apolipoproteins, exhibiting  $[GdnHCl]_{1/2}$  values of  $\leq 1.0$  M, and  $\Delta G = 3.9$  kcal/mol (Table 16). Nevertheless, what is not known is the order of helix-helix unfolding of the CT

domain and mechanistic details, which are important pieces of information required to understand its role in initiation of lipid binding.

To address this, we determined the ease of helix destabilization by calculating the  $\Delta G$  of GdnHCl-induced unfolding. Rather than relying on CD alone which only yields global information about overall helical content, we employed fluorescence spectroscopy, specifically FP. Using known high resolution X-ray and NMR structures of apoE, Cys substitutions were made to introduce probes at specific sites to monitor the flexibility and rotational tumbling of localized segments in the protein. In a complementary approach, we determined the solvent accessibility of specified sites by performing HDX/MS as determined by incorporation of deuterium as a function of time. The ease of incorporation especially in the protein interior is reflective of ease of solvent penetration and therefore ease of breaking amide-hydrogen H-bonding (78). We used apoE3(1-191) and apoE(201-299) since these segments are folded as independent NT and CT domains, respectively. In intact apoE3, a protease-sensitive segment (residues 192-201) link the two domains. Individually the isolated domains recapitulate their corresponding structural and functional features in the intact protein.

#### Fluorescent Tagging of NT and CT Domain

The 4 main helices in the NT domain helix-bundle and the 3 helices of the CT domain were probed with AEDANS, a fluorescent probe which has been used extensively to monitor the polarity of the micro environment at site of attachment giving information on conformational changes (60, 67, 91). Recombinant apoE3 bearing a Hexa-His tag was over-expressed in *E. coli*, isolated and purified by Ni<sup>2+</sup>-affinity chromatography. In addition to the Hexa-His, the 17-residue tag (numbered -1 to -17)

also encompasses a protease cleavage site that was engineered to facilitate cleavage if required. However, from previous studies, we have established that the presence of the Hexa-His tag does not perturb the overall secondary or global tertiary structure (27, 65) of apoE. Therefore, it is present in all our studies, but typically ignored in our analysis. For MS studies, only the isolated domains of the WT apoE3 were utilized. All proteins were > 95% pure as assessed by SDS-PAGE (Figure 8). After confirming the size and purity of the isolated domains, the proteins were labeled with AEDANS.

AEDANS was utilized due to its relatively long fluorescent lifetime (10-15 ns), making it suitable for polarization spectroscopy (66). IAEDANS is a thiol reactive fluorophore, which upon covalent attachment to Cys can serve as an efficient reporter of the polarity of the microenvironment. 10 ns molecular dynamics study using GROMACS 3.3.1 computer simulations showed that AEDANS is neither hindered by lipids nor neighboring amino acids, a useful property often exploited for membrane proteins (67). In addition AEDANS can move freely in polar and lipid environment due to its low dipole moment (67). For our experiments, we took advantage of the fluorescent properties of AEDANS as a faithful reporter of intensity and polarization changes upon GdnHCl-induced denaturation. AEDANS labeling was performed under reducing conditions using TCEP, to reduce inter-molecular disulfide bonds and in the presence of GdnHCl to obtain complete and equitable access to Cys. Excess TCEP, GdnHCl and unconjugated IAEDANS were removed by extensive dialysis. The stoichiometry of labeling was found to be between ~ 0.9 to ~ 1.2 for all the NT and CT single cysteine variants (Table 4).

### Unfolding of apoE3 NT Domain

GdnHCl-induced denaturation followed by secondary structural analysis using CD spectroscopy confirmed that neither substitution by a Cys nor the presence of the fluorophore affected the overall global fold of the single Cys apoE NT or CT domains (Figure 10 and 11). The  $D_{1/2}$  was  $2.4 \pm 0.4$  M GdnHCl, which is in the range typically noted for unlabeled apoE3(1-191) NT domain (2.5 M). Thus, the CD spectroscopic data demonstrated that the presence of AEDANS does not significantly alter helix-helix interactions in the NT domain.

GdnHCl-induced unfolding was also followed by monitoring changes in fluorescence intensity of each AEDANS-labeled NT variant. As expected, a decrease in emission intensity was noted, accompanied by a red shift in the  $\lambda_{\max}$  of each labeled variant, demonstrating a conformational change and exposure of AEDANS to a more polar environment (Table 7, Figure 13). The  $D_{1/2}$  as followed by changes in fluorescence intensity and  $\lambda_{\max}$  of each labeled variant was  $3.1 \pm 0.3$  M,  $2.7 \pm 0.1$  M,  $1.5 \pm 0.3$  M,  $2.1 \pm 0.4$  M GdnHCl for H1, H2, H3, and H4 respectively. Thus, from changes in the fluorescence emission characteristics, we infer that the probe, which was already solvent exposed and located in a polar microenvironment (by design) elicited changes in environment with a range of 9-21 nm in  $\lambda_{\max}$  depending on AEDANS position (Table 7).

Lastly, we utilized FP spectroscopy to assess GdnHCl-induced changes in mobility of the probe attached to different helices on the NT domain. It offered alternative information that fluorescence intensity measurements were unable to provide. Previous studies have used FP to obtain dynamic information by real-time analysis of macromolecular interactions (71). For example FP was used to monitor transcriptional

regulation of coactivator binding by following rotational motion of fluorescein-labeled estrogen receptor element (ERE) following interaction with the estrogen receptors (ER). The ligand-bound ER forms a transcription complex that binds ERE. FP was used to monitor the binding of steroid receptor coactivator thus forming ERE-ER-coactivator complex. Slow rotation was observed, indicative of complex formation compared to ERE alone (92). We used the same principle to monitor AEDANS-labeled NT and CT domains and monitor mobility of individual helices upon GdnHCl denaturation.

Interestingly, the  $D_{1/2}$  ranged from 2.1 to 3.9 M GdnHCl, depending on the probe location. The  $D_{1/2}$  for H1 was  $3.9 \pm 0.08$  M GdnHCl a relatively higher midpoint compared to that of other helices, especially H3 and H4. Helices H3 and H4 displayed a significantly lower  $D_{1/2}$  ( $2.1 \pm 0.3$  and  $2.2 \pm 0.4$ , respectively \* $P < 0.05$ ). This suggests that H3/H4 may experience a less stable environment, while H1/H2 may be in a more stable environment. The  $\Delta G$  of unfolding for H1 was  $2.9 \pm 1.6$  kcal/mol, which is reflective of a relatively stable environment for AEDANS near position 29. In the vicinity of position 29 there are four Trp residues at positions 20, 26, 34 and 39. Computational studies using a straight  $\alpha$ -helical M13 major coat protein suggest there may be a small degree of stacking between the AEDANS moiety and Trp residues, however they did not find a systematic effect on conformation space and interaction between neighboring Trp side-chains (67). With this in mind, it is still possible that a similar stacking interaction can occur between AEDANS at position 29 and Trp at 20, 26, 24 or 39.

### Unfolding of apoE CT domain

In our analysis of chemical denaturation of the AEDANS-labeled CT variants, the aim was to understand global unfolding and change in overall secondary structure as measured by CD spectroscopy. The  $D_{1/2}$  values obtained for the CT variants were in the range 1.3 -1.9 M GdnHCl, which is similar to that noted for WT apoE CT domain (~ 1.5 M) (reported values range from 0.7-1.1M). As expected, in general, the  $D_{1/2}$  values for AEDANS-labeled CT variants were lower than that for the NT variants. The free energy of unfolding for the AEDANS-labeled CT variants ranged from 1.7-1.9 kcal/mol, which was in agreement with that seen for the WT protein (1.7 kcal/mol) suggesting that the presence of AEDANS did not significantly alter the overall secondary structure.

GdnHCl-induced unfolding was also followed by monitoring changes in fluorescence intensity of each AEDANS-labeled CT variant. All CT variants display a red-shift in  $\lambda_{\max}$  demonstrating a conformational change and exposure of AEDANS to a more polar environment. Although the total integrated fluorescence for AEDANS-apoEA277C(201-299) was the lowest, due to ~50% labeling efficiency, it showed a similar red-shift in  $\lambda_{\max}$  as other CT variants ending at ~497nm. Lastly, FP spectroscopy was utilized to assess GdnHCl-induced changes in mobility of the probe attached to different helices on the CT domain. These results are preliminary (n=1) and need to be confirmed with more data sets; nevertheless the trend indicates that AEDANS-apoEA277C(201-299) had the highest FP value ~0.246, which is higher compared to A209C, S223C, and E255C (Table 10). The  $D_{1/2}$  value for A277C was relatively higher, 2.8 M GdnHCl, compared to ~1.0 M GdnHCl for the other CT variants. This information

suggests that the segment around position 277 is more rigid and less susceptible to denaturation, which is likely due to the involvement of residues 266-299 in protein-protein interaction (18) with corresponding sites on a neighboring apoE CT molecule leading to apoE tetramerization.

#### Accessibility of Amide Backbone of apoE3 NT from HDX/MS

From our HDX/MS data we derived information about solvent accessibility at the peptide level, from which we made inferences regarding the secondary structural organization of the NT and CT domain of apoE3. The availability of high resolution structure of apoE3(1-191) from X-ray analysis at 2.1 Å and apoE3(1-183) from NMR spectroscopy at 1.22 Å allowed us to validate our inference. This strategy also allowed us to establish confidence in the inference for apoE CT, for which high-resolution structural information is not available in the tetrameric state. The protection plot of apoE3 NT peptides shows that peptides 105-123 (H3) and 133-154 (H4) have positive Log Pf values of 0.41 and 2.72 respectively. % D uptake in these two regions were 15-21% and 9-44% respectively (Table 11). Since the level of exchange of amide-hydrogen is inversely proportional to the stability of hydrogen-bonding network within the secondary structure (93), the relatively low extent of D incorporation could be explained by low solvent accessibility and high degree of protection of these sites roughly corresponding to helices H3 and H4 in the native protein. Furthermore, H3/H4 had similar FP values at 0 M GdnHCl ~0.111, indicating the range of mobility under native conditions. The similar extent of % D uptake of H3/H4 can be explained by the inter-helical residue proximity leading to a strong interaction. This observation derives support from the NMR structure of apoE3(1-183) (PDB 2KC3) and X-ray structure of apoE3(1-191) (PDB 1NFN), which

show that the H3/H4 interface is stabilized by hydrophobic interactions involving Leu zippers, buried H-bonds, and salt-bridges as seen in Figure 29, Table 16. In contrast, H1/H2 interface has fewer hydrophobic interactions. Figure 29 demonstrates stabilization of helices in apoE3 NT making it thermodynamically stable; although H3 and H4 remain in close association as helices in the native conformation they can be triggered to dissociate upon denaturation as seen in the FP studies. At the H3/H4 interface NMR studies revealed the H3 and H4 bears six polar hydrophilic residues (24): Asp-107, Arg-114, Tyr-118, Asp-151, Arg-158, and Try-162 in the protein's interior (Figure 30).

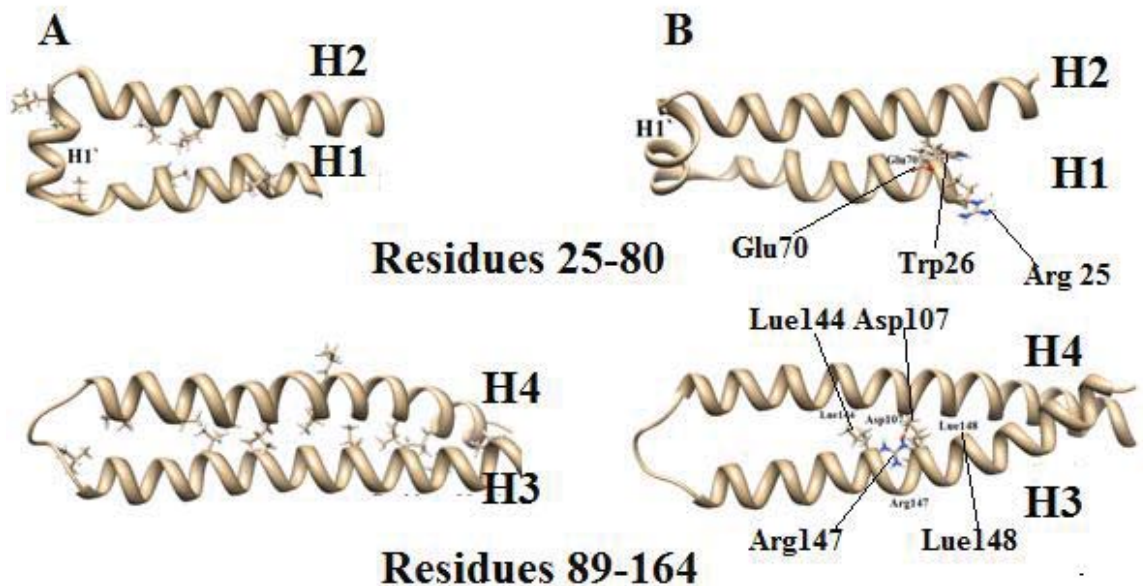


FIGURE 29. Leu zippers and H-bonds in H1/H2 and H3/H4 of apoE3(1-191). A. WT H1/H2 and H3/H4 leucine zipper interfaces in apoE3(1-183) a close-up version of residues 89-164 and 25-80 from NMR structure of apoE3(1-183) is shown, leu residues part of zipper shown on Table 16. B. Buried H-bonds between the interface of H1/H2 and H3/H4, detail interactions on Table 16.

The authors proposed that the presence of the polar residues likely destabilize the hydrophobic core. FP data suggest that H3/H4 become easily mobile with  $\Delta G \sim 1.7$  kcal/mol suggesting helix dissociation caused by destabilizing buried hydrophilic residues. In comparison the  $\Delta G$  for H1 was  $\sim 2.9$  kcal/mol requiring higher denaturant concentrations to facilitate unfolding. It also has the highest value for unfolding as well as the highest FP value (Table 10). H2 has an intermediate value falling between H1 and H3/H4; interestingly denaturation unfolding curves for H2 shows the slope of H2 being markedly different from all helices. This observation in FP data best describes the helical-interface between helices 3 and 4 likely to be disrupted with low [GdnHCl] resulting in a more flexible and mobile region followed by helix dissociation of H1/H2.

The hinge between H2 and H3 (residues 77-89, ELEEQLTPVAEE) named the 80's loop residues is thought to initiate lipid interaction due to the presence of acidic residues that could interact with the positively charged phosphatidylcholine head groups (20). Such an interaction could lead to helix bundle opening via the 80's loop with H1/H2 moving away from H3/H4 (Figure 31). In conclusion, FP data show sites of increased mobility suggesting and validating our hypothesis of initial helix bundle opening comparable to a book model (Figure 28), where helix pairs H1/H2 and H3/H4 unfold via 80's loop. This along with HDX/MS reflecting solvent accessible sites and highest protection (lower % D) will shed light into the initial moments of helix bundle opening.

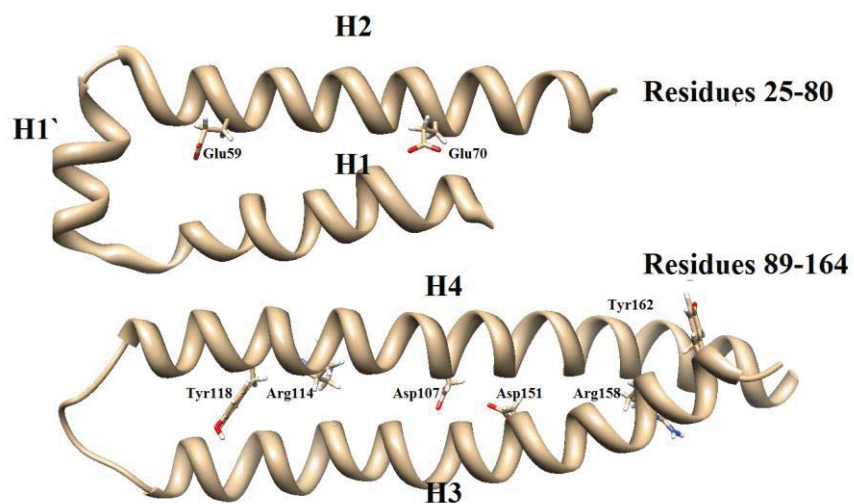


FIGURE 30. Buried hydrophilic residues in apoE3(1-183) H1/H2 (residues 25-80) has fewer buried hydrophilic residues at the helix-helix interface than H3/H4 (89-164).

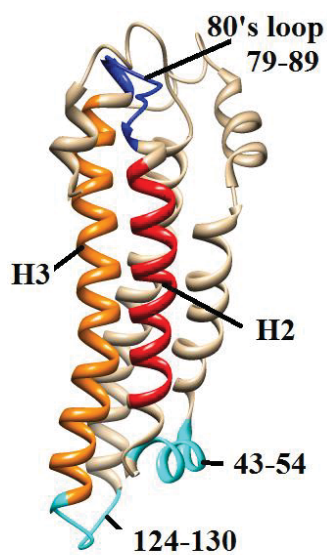


FIGURE 31. 80's loop is the hinge for helix bundle opening of ApoE3 (1-191). NT domain 1-hinge unfolding hypothesis uses 80's loop (residues 79-89) colored blue. In contrast the 2-hinge model would involve opening via 43-54 and 124-130, colored cyan.

### ApoE CT HDX/MS

Our current knowledge of the CT domain of apoE emphasizes its role in protein self association and interaction with lipoproteins (18). Truncations of apoE3 at positions 266, 244, 223, and 191 yielded monomers instead of tetramers compared to native apoE3. The truncated mutants of the CT domain were not able to associate with VLDL, which underscores the structural role and functional importance. Further studies with mutagenesis showed that replacing five bulky, nonpolar residues (F257, W264, V269, L279, V287) with polar residues prevented apoE tetramerization but still retained its ability to bind to lipids (31). Earlier studies from our lab showed that the entire CT domain of one apoE(201-299) molecule makes extensive contact with a neighboring molecule yielding a dimer, which likely dimerize further to yield a tetramer. Lastly, other researchers show that specified residues (and segments) in the CT domain are in close proximity to the NT domain; with the degree of proximity varying in an isoform specific manner. Our current study is based on the original premise wherein residues 201-299 was designated as a domain since it was capable of existing as an independently folded structural and functional unit. The sequence of apoE(201-299) bearing a His-tag at its N-terminal end is shown in Figure 34. We attempted to address possible modes of unfolding of the CT domain induced by chemical denaturation as followed by fluorescence spectroscopy and had determined solvent accessibility by HDX/MS.

Our results from polarization spectroscopy show that AEDANS-labeled variants A209C, S223C, and E255C had  $\Delta G \sim 1.2$ , 1.2 and 1.4 kcal/mol respectively (Table 10). While A277C had  $\Delta G = 1.5$  kcal/mol; the high FP value for the latter is an indicator of a relatively more stable and rigid segment towards the C-terminal end of the protein. The FP value for AEDANS-A277C in the absence of GdnHCl was 0.246 compared to FP = 0.89 of CT variants A209C, S223C, and E255C (Table 10), which is significantly higher than 0.89 observed for other variants.

MHHHHHHGLVPRGSIDPQPLQERAQAWGERLRARMEEMGSRTRDRLDEVKEQ  
VAEVRAKLEEQAQQIRLQAEAFQARLKSWEPLVEDMQRQWAGLVEKVQAAV  
 GTSAAPVPSDNH

FIGURE 32. Wild type Human ApoE CT (201-299) bearing a His-tag. Underlined portion represents the His-tag while double lines represent helices C1, C2, and C3.

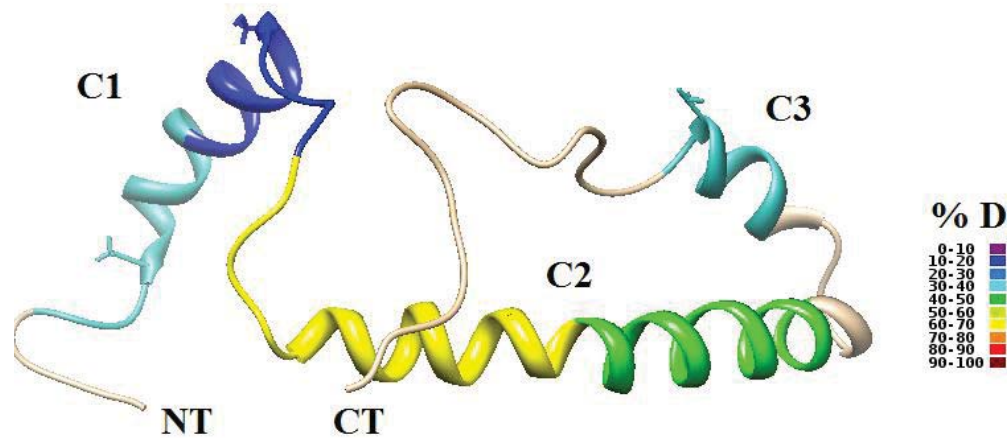


FIGURE 33. % D incorporation on CT helices C1, C2 and C3 superimposed on the NMR structure of apoE3(1-299) (PDB 2L7B). The protein model is shaded according to %D at end of labeling. Helices are shown in ribbon form. Color shading represents amount of D uptake by segment. Grey represents segments for which there is no data.

Interestingly our HDX data with FP data tells us dynamic information regarding the CT domain under our experimental conditions employed in our lab. The information we gathered from HDX seems to indicate that regions 230-270 undergoes high % D exchange which coincides with the self-association domain and the lipid binding domain. Regions that underwent low % D were the N-terminal and C-terminal regions of the domain which could suggest regions of inter-molecular interactions (Figure 33). FP data revealed that segments encompassing positions 209, 223, and 255 underwent greater mobilization which could explain the % D uptake in those regions. Together these results can be used to describe a possible mode of unfolding in the greater context of initiation in lipid binding.

#### Summary and Perspectives

Our research findings were aimed at understanding the order of helix bundle opening in the isolated NT and CT domains of apoE. HDX/MS experiments gave us peptide level information regarding the protein's solvent accessible sites and dynamic flexible regions. Figure 33 gives the % D of the isolated CT domain mapped onto the NMR PDB 2L7B of the apoE monomeric mutant. Helices C2 has highest % D compared to C1 and C3 with overall lower % D uptake. This data would lead to suggest that H-bonding stability in the  $\alpha$ -helical region C2 is most susceptible to exchange with solvent D and thus more dynamic. FP data is a measure of the rigidity or rotation of the fluorophore during the GdnHCl-induced denaturation of the CT domain, thus giving information about flexible regions. Figure 17 shows that A277C CT variant was the most rigid of all the positions with an FP value of 0.246. This piece of data corresponds to the % D uptake in that region of the CT domain suggesting that upon denaturation, A277 is a

region that will resist denaturing. Since the CT domain is a tetramer in solution, our fluorescence intensity data indicates that tertiary inter-molecular interactions are broken prior to secondary structure loss as assessed by thermodynamic free energy of unfolding  $\Delta G$  values lower in comparison to CD spectroscopy values (Table 6). Thus, our model for the CT domain unfolding mechanism describes a model whereby dissociation of dimer-dimer occurs first then the C-terminal end unfolds releasing C3 followed by C2/C1.

We initially used the NT domain contact map (Figure 4) based off the NMR structure PDB 2KC3 that displays residue distances between H1/H2 and H3/H4 as a guide to propose possible modes of unfolding of the NT 4-helix bundle. HDX/MS studies help to understand the sites of D uptake and thus better understand dynamic regions within the helices of apoE3(1-191). Figure 23 shows % D data on the NMR structure of the NT domain serving as a visual guide to show that H3/H4 were regions which underwent limited deuteration. In contrast, H1/H2 regions incorporated 50-60 % D and considered exposed helical segments susceptible to exchange. This data reflects physicochemical properties between the helices as well as their solvent penetration. Upon addition of GdnHCl denaturation of the NT domain the measure of polarization was measured to give insight into the rotational movement of the AEDANS moiety attached to specific helices to monitor mobility. Figure 16 suggest that A29 position on the helix 1 shows a rigid structure that could be interpreted to unfold after the rest of the apoE molecule has been unfurled. Figure 14 gives fluorescence intensity data that give information about the micro environment of the fluorescent probe upon denaturation. This data shows that H3/H4 show similar intensity curves and different from those of H1/H2 which could serve to describe similar unfolding mechanism between helices.

With support from our HDX/MS and FP data we propose an unfolding model named the book model where H1/H2 separate from H3/H4 via a hinge (Figure 28) 80's loop. In the helix bundle where the interface between helices play a crucial role in stabilization due to H-bonds, salt-bridges, and Van der Waals interactions, the susceptibility of destabilization could be measured by the amount of [GdnHCl] needed to disrupt these interactions. FP and intensity data reveal sites on the NT domain where the helix bundle can potentially open and unfurl helices. Also the position of buried polar residues between H3/H4 interface play a role in helix bundle stability and thus opening and unfolding. Our model cannot exclude other models at this stage of our experiments but describes to the best of our interpretation of biophysical data from state-of-the-art MS techniques and sensitive fluorescence experiments measuring polarization at defined sites along the NT and CT domains. Future work would be needed to elucidate an exact mechanism of helices as well as in the full length context of the apoE molecule. Further site-directed mutagenesis of residues near helix 1 could further substantiate A29 rotation during unfolding. In conclusion, this study gives supporting evidence for the one hinge mediated book model opening whereby H1/H2 and H3/H4 move apart and facilitate the opening of the NT helix bundle which bears significance in cardiovascular and neurodegenerative disease where protein unfolding mechanisms could play a role during pathogenesis and disease progression.

TABLE 17. D Uptake at Each Time Point ApoE (1-191)

Amino Acid Position	Time (min)	D	N	%D	
1	14	0.5	4.7	11	42.9
1	14	1	6.3	11	57.0
1	14	5	6.5	11	59.2
1	14	10	5.7	11	52.1
1	14	15	6.3	11	57.4
1	14	30	5.9	11	53.4
1	14	60	5.8	11	53.2
1	14	120	6.0	11	54.2
15	30	0.5	6.3	15	42.0
15	30	1	6.1	15	40.6
15	30	5	7.2	15	48.1
15	30	10	6.2	15	41.5
15	30	15	7.2	15	47.8
15	30	30	7.3	15	48.9
15	30	60	7.6	15	50.7
15	30	120	7.9	15	52.8
46	51	0.5	1.9	5	37.3
46	51	1	2.9	5	57.5
46	51	5	2.8	5	56.3
46	51	10	2.6	5	52.1
46	51	15	2.9	5	57.3
46	51	30	2.9	5	57.3
46	51	60	2.9	5	57.1
46	51	120	2.8	5	56.6
52	60	0.5	2.2	8	27.5
52	60	1	4.1	8	51.3
52	60	5	4.5	8	56.2

52	60	10	4.2	8	52.4
52	60	15	4.8	8	60.0
52	60	30	4.8	8	59.9
52	60	60	4.7	8	59.1

TABLE 17. Continued

Amino Acid Position		Time (min)	D	N	%D
52	60	120	4.7	8	59.0
61	73	0.5	4.4	12	36.8
61	73	1	7.3	12	61.2
61	73	5	7.6	12	63.0
61	73	10	6.5	12	54.1
61	73	15	7.4	12	61.9
61	73	30	7.1	12	58.8
61	73	60	6.9	12	57.5
61	73	120	7.2	12	59.7
74	78	0.5	1.2	4	29.8
74	78	1	1.9	4	47.8
74	78	5	2.0	4	51.1
74	78	10	1.8	4	45.5
74	78	15	1.9	4	48.5
74	78	30	2.0	4	49.7
74	78	60	2.0	4	51.1
74	78	120	2.0	4	51.0
79	87	0.5	2.5	7	35.8
79	87	1	4.0	7	57.7
79	87	5	4.1	7	58.5
79	87	10	3.7	7	52.1
79	87	15	4.0	7	56.5
79	87	30	3.9	7	55.7
79	87	60	3.9	7	55.3
79	87	120	4.0	7	56.7
92	97	0.5	1.6	5	31.4
92	97	1	2.6	5	51.2

92	97	5	2.7	5	53.0
92	97	10	2.4	5	47.1
92	97	15	2.5	5	50.4
92	97	30	2.5	5	50.1
92	97	60	2.5	5	50.2

TABLE 17. Continued

Amino Acid Position	Time (min)	D	N	%D	50.9
94	104	0.5	4.0	10	39.7
94	104	1	5.6	10	55.7
94	104	5	6.5	10	64.5
94	104	10	5.6	10	56.4
94	104	15	6.6	10	66.4
94	104	30	6.7	10	67.4
94	104	60	6.9	10	68.6
94	104	120	7.1	10	71.2
105	123	0.5	2.7	18	15.2
105	123	1	4.0	18	22.0
105	123	5	4.0	18	22.5
105	123	10	3.7	18	20.8
105	123	15	3.8	18	21.3
105	123	30	3.8	18	21.0
105	123	60	3.7	18	20.5
105	123	120	3.9	18	21.4
126	133	0.5	1.9	7	27.0
126	133	1	3.3	7	47.7
126	133	5	3.4	7	48.7
126	133	10	3.0	7	43.3
126	133	15	3.3	7	46.4
126	133	30	3.2	7	45.6
126	133	60	3.1	7	45.0
126	133	120	3.2	7	45.9
133	137	0.5	1.9	4	47.3
133	137	1	1.8	4	44.4
133	137	5	2.4	4	60.2
133	137	10	2.0	4	49.2
133	137	15	2.6	4	64.7
133	137	30	2.4	4	61.1
133	137	60	2.5	4	62.7
133	137	120	2.5	4	62.4

133	154	0.5	1.9	21	9.0
133	154	1	4.1	21	19.6
133	154	5	6.7	21	32.1
133	154	10	5.1	21	24.2
133	154	15	7.6	21	36.1

TABLE 17. Continued

Amino Acid Position	Time (min)	D	N	%D	39.1
133	154	60	8.9	21	42.2
133	154	120	9.3	21	44.2
162	176	0.5	4.5	14	32.1
162	176	1	7.4	14	52.6
162	176	5	7.7	14	54.7
162	176	10	6.6	14	47.0
162	176	15	7.2	14	51.7
162	176	30	7.1	14	50.8
162	176	60	7.0	14	49.8
162	176	120	7.1	14	50.9
177	187	0.5	3.8	9	42.5
177	187	1	5.3	9	58.6
177	187	5	5.5	9	60.7
177	187	10	4.8	9	53.1
177	187	15	5.2	9	57.6
177	187	30	5.1	9	56.2
177	187	60	5.0	9	55.1
177	187	120	5.1	9	57.1

D: deuterium uptake, N: number of amide-hydrogens that were exchangeable for that peptide

TABLE 18. D uptake at each time point during HDX analysis of apoE3(1-191)

Amino Acid Position	Time (min)	D	N	%D
206 214	0.5	1.4	8	17.4
206 214	1	1.4	8	17.2
206 214	5	1.2	8	14.6
206 214	10	1.0	8	12.5
206 214	15	1.1	8	13.2
206 214	30	1.0	8	12.2
206 214	60	1.0	8	12.2
206 214	120	1.0	8	12.5
206 216	0.5	2.2	10	22.5
206 216	1	2.1	10	20.5
206 216	5	2.0	10	19.5
206 216	10	1.8	10	17.7
206 216	15	1.8	10	18.1
206 216	30	1.7	10	16.9
206 216	60	1.8	10	18.3
206 216	120	1.6	10	16.3
206 218	0.5	3.6	12	29.7
206 218	1	3.7	12	31.0
206 218	5	3.0	12	25.0
206 218	10	2.9	12	24.3
206 218	15	3.1	12	25.8
206 218	30	3.0	12	25.4
206 218	60	2.9	12	24.1
206 218	120	3.0	12	25.3
217 229	0.5	1.7	12	14.3
217 229	1	1.7	12	14.1
217 229	5	1.5	12	12.7

217	229	10	1.4	12	11.3
217	229	15	1.3	12	11.1
217	229	30	1.2	12	10.4
217	229	60	1.3	12	10.8
217	229	120	1.2	12	10.4

TABLE 18. Continued

Amino Acid Position	Time (min)	D	N	%D	
217	231	0.5	1.8	14	12.7
217	231	1	1.9	14	13.5
217	231	5	1.7	14	12.0
217	231	10	1.5	14	10.6
217	231	15	1.5	14	10.5
217	231	30	1.4	14	9.9
217	231	60	1.4	14	9.8
217	231	120	1.4	14	9.9
219	229	0.5	1.0	10	10.0
219	229	1	1.1	10	11.4
219	229	5	1.3	10	13.4
219	229	10	1.2	10	12.2
219	229	15	1.2	10	12.1
219	229	30	1.1	10	11.3
219	229	60	1.1	10	10.6
219	229	120	1.0	10	10.2
219	231	0.5	1.6	12	13.2
219	231	1	1.7	12	13.8
219	231	5	1.6	12	12.9
219	231	10	1.4	12	11.9
219	231	15	1.5	12	12.4
219	231	30	1.4	12	11.8
219	231	60	1.4	12	11.6
219	231	120	1.4	12	11.3
230	249	0.5	5.8	12	48.1
230	249	1	6.5	12	54.5
230	249	5	11.6	12	96.9
230	249	10	11.3	12	94.5
230	249	15	11.9	12	99.5
230	249	30	12.1	12	101.1
230	249	60	12.7	12	105.6
230	249	120	12.1	12	100.9
232	243	0.5	1.8	11	16.3
232	243	1	2.2	11	20.1

232	243	5	4.8	11	43.3
232	243	10	5.3	11	47.9
232	243	15	5.4	11	49.4
232	243	30	6.0	11	54.9
232	243	60	5.5	11	49.8

TABLE 18.Continued

Amino Acid Position		Time (min)	D	N	%D
232	243	120	4.7	11	42.7
232	249	0.5	5.2	17	30.5
232	249	1	4.6	17	26.9
232	249	5	9.3	17	54.9
232	249	10	9.9	17	58.5
232	249	15	10.8	17	63.5
232	249	30	10.5	17	61.9
232	249	60	10.3	17	60.4
232	249	120	10.4	17	61.2
250	254	0.5	1.2	4	29.7
250	254	1	1.3	4	31.9
250	254	5	1.6	4	40.5
250	254	10	1.6	4	40.6
250	254	15	1.7	4	43.3
250	254	30	1.7	4	42.9
250	254	60	1.7	4	43.5
250	254	120	1.6	4	39.1
253	261	0.5	3.7	8	45.8
253	261	1	3.8	8	47.5
253	261	5	4.3	8	54.2
253	261	10	4.4	8	54.7
253	261	15	4.3	8	53.8
253	261	30	4.1	8	51.8
253	261	60	4.2	8	52.5
253	261	120	4.5	8	56.1
253	263	0.5	4.9	10	49.5
253	263	1	5.1	10	50.9
253	263	5	4.9	10	49.0
253	263	10	5.4	10	54.0
253	263	15	5.7	10	56.8
253	263	30	5.5	10	55.2
253	263	60	5.4	10	54.4
253	263	120	5.2	10	51.6

262	270	0.5	0.6	7	9.3
262	270	1	x	7	
262	270	5	1.6	7	22.5
262	270	10	1.9	7	27.0
262	270	15	2.2	7	31.7

TABLE 18. Continued

Amino Acid Position	Time (min)	D	N	%D	
262	270	30	2.5	7	36.1
262	270	60	2.7	7	38.5
262	270	120	3.1	7	44.3
262	272	0.5	0.9	9	10.3
262	272	1	x	9	
262	272	5	2.3	9	25.9
262	272	10	2.9	9	31.8
262	272	15	3.3	9	36.2
262	272	30	3.7	9	41.1
262	272	60	3.7	9	41.3
262	272	120	4.1	9	45.5
265	270	0.5	0.3	4	7.6
265	270	1	0.6	4	13.8
265	270	5	0.8	4	19.0
265	270	10	0.9	4	22.7
265	270	15	1.2	4	30.9
265	270	30	1.5	4	38.0
265	270	60	2.5	4	62.0
265	270	120	2.2	4	54.9
265	272	0.5	0.5	6	8.9
265	272	1	x	6	
265	272	5	1.1	6	17.6
265	272	10	1.7	6	28.6
265	272	15	2.0	6	33.4
265	272	30	2.8	6	47.0
265	272	60	2.9	6	47.9
265	272	120	2.0	6	32.5
271	279	0.5	1.7	8	21.1
271	279	1	x	8	
271	279	5	2.9	8	36.0
271	279	10	2.4	8	29.9
271	279	15	2.0	8	25.5
271	279	30	1.9	8	23.7

271	279	60	1.9	8	23.5
271	279	120	2.1	8	26.5
272	279	0.5	1.5	7	20.8
272	279	1	1.5	7	21.0
272	279	5	2.0	7	28.9

TABLE 18. Continued

Amino Acid Position	Time (min)	D	N	%D
272 279	10	1.7	7	24.8
272 279	15	1.7	7	23.8
272 279	30	1.8	7	25.1
272 279	60	1.6	7	22.7
272 279	120	1.6	7	23.4

D: deuterium uptake, N: number of amide-hydrogens that were exchangeable for that peptide, x: data not available.

APPENDIX

LIST OF RESEARCH PUBLICATIONS AND PRESENTATIONS

CIRM Bridges Trainee Meeting (California Institute for Regenerative Medicine), 2014, San Francisco, Ca (**Hernandez, R.**, Tian, E., Li, Wendong., Shi, Yanhong.) “Human iPSC Generation Harboring Genetic Risk Alleles Apolipoprotein E4 Analysis and Probing Astrocyte Mediated Uptake of Anti-inflammatory Lipidated Apolipoprotein E”, poster

Annual Biomedical Research Conference for Minority Students (ABRCMS), 2013, Nashville, TN (**Hernandez, R.**, Beck, W., Nguyen, P., Patel, A., Nirudodhi, S., Duong, M., Venkataraman, A., Maier, C. S., and Narayanaswami, V.) “Structural Analysis of LDLr domain and High Lipid Affinity binding domain of Apolipoprotein E using Hydrogen /Deuterium Exchange Coupled to Mass Spectrometry and Fluorescence Spectroscopy”, poster.

25<sup>th</sup> Annual CSU Program for Education and Research in Biotechnology, 2013, Anaheim CA. (**Hernandez, R.**, Beck, W., Nguyen, P., Patel, A., Nirudodhi, S., Duong, M., Venkataraman, A., Maier, C. S., and Narayanaswami, V.) “Structural Analysis of Human Apolipoprotein E3 N-terminal and C-terminal domains by Mass Spectrometry and Fluorescence Polarization Spectroscopy”, poster.

Gordon Research Conference Lipoprotein Metabolism, 2012, Waterville Valley, NH. (**Hernandez, R.**, Dwivedi, P., Beck, W., Nguyen, P., Patel, A., Nirudodhi, S., Duong, M., Venkataraman, A., Maier, C. S., and Narayanaswami, V.) “Structural Analysis of Human Apolipoprotein E3 by Fluorescence Spectroscopy and Hydrogen/Deuterium Exchange Coupled to Mass Spectrometry”, poster.

56<sup>th</sup> Annual Biophysical Society Meeting, 2012, San Diego CA. (**Hernandez, R.**, Dwivedi, P., Beck, W., Nguyen, P., Patel, A., Nirudodhi, S., Duong, M., Venkataraman, A., Maier, C. S., and Narayanaswami, V.) “Structural Analysis of Human Apolipoprotein E3 by Fluorescence Spectroscopy and Hydrogen/Deuterium Exchange Coupled to Mass Spectrometry”, poster.

1<sup>st</sup> annual Strengthening Health Sciences with Culture/*Fortaleciendo las Ciencias de la Salud con Cultura*, 2012, Long Beach, CA. (**Hernandez, R.**, Dwivedi, P., Beck, W., Nguyen, P., Patel, A., Nirudodhi, S., Duong, M., Venkataraman, A., Maier, C. S., and Narayanaswami, V.) “Structural Insight of Human Apolipoprotein E3

C-terminal and N-terminal domain by Fluorescence Spectroscopy Hydrogen/Deuterium Exchange coupled to Mass spectrometry”, poster.

24<sup>th</sup> Annual CSU Program for Education and Research in Biotechnology, 2012, Santa Clara, CA (**Hernandez, R.**, Dwivedi, P., Beck, W., Nguyen, P., Patel, A., Nirudodhi, S., Duong, M., Venkataraman, A., Maier, C. S., and Narayanaswami, V.) “Structural Insight of Human Apolipoprotein E3 by Fluorescence Spectroscopy Hydrogen/Deuterium Exchange coupled to Mass spectrometry”, poster.

CHORI Summer Student Research Program Short Term Training To Increase Diversity In Health-Related Research, 2011, Oakland, CA. (**Hernandez, R.**, Dwivedi, P., Beck, W., Nguyen, P., Patel, A., Nirudodhi, S., Duong, M., Venkataraman, A., Maier, C. S., and Narayanaswami, V.) “Structural Insight into Apolipoprotein E C-terminal domain using HDX coupled with ESI-LCMS”, poster.

College of Natural Science and Mathematics, 2011, Long Beach, CA. (**Hernandez, R.**, Dwivedi, P., Nirudodhi, S., Duong, M., Maier, C. S., and Narayanaswami, V.) “Structural Analysis of Human Apolipoprotein E3 N-terminal and C-terminal domains by Mass Spectrometry and Fluorescence Spectroscopy”, poster.

CSUSB McNair Symposium, 2010, San Bernardino, CA. (**Hernandez, R.**) “Purification of the B1 Immunoglobulin-binding Domain of Streptococcal G Protein (GB1) for use in Solid State Nuclear Magnetic Resonance”, oral presentation

## BIBLIOGRAPHY

## BIBLIOGRAPHY

1. Davignon, J., Gregg, R. E., and Sing, C. F. (1988) Apolipoprotein E polymorphism and atherosclerosis. *Arteriosclerosis Thrombosis Vascular Biology* 8, 1–21
2. Huang, Y., and Mucke, L. (2012) Alzheimer mechanisms and therapeutic strategies. *Cell* 148, 1204–1222
3. Burre, J., Sharma, M., Tsetsenis, T., Buchman, V., Etherton, M. R., and Sudhof, T. C. (2010) Synuclein promotes SNARE-complex assembly in vivo and in vitro. *Science* 329, 1663–1667
4. Assmann, G., Cullen, P., Jossa, F., Lewis, B., and Mancini, M. (1999) Coronary heart disease: reducing the risk : the scientific background to primary and secondary prevention of coronary heart disease a worldwide view. *Arteriosclerosis, Thrombosis, and Vascular Biology* 19, 1819–1824
5. Aggerbeck, L. P., Wetterau, J. R., Weisgraber, K. H., Wu, C. S., and Lindgren, F. T. (1988) Human apolipoprotein E3 in aqueous solution. II. properties of the amino- and carboxyl-terminal domains. *Journal of Biological Chemistry* 263, 6249–6258
6. Von Eckardstein, A., Nofer, J.-R., and Assmann, G. (2001) High density lipoproteins and arteriosclerosis : role of cholesterol efflux and reverse cholesterol transport. *Arteriosclerosis, Thrombosis, and Vascular Biology* 21, 13–27
7. Weisgraber, K. H., Pitas, R. E., and Mahley, R. W. (1994) Lipoproteins, neurobiology, and Alzheimer's disease: structure and function of apolipoprotein E. *Current Opinion in Structural Biology* 4, 507–515
8. Hatters, D. M., Peters-Libeu, C. A., and Weisgraber, K. H. (2006) Apolipoprotein E structure: insights into function. *Trends in Biochemical Sciences* 31, 445–454
9. Tall, A. R. (2008) Cholesterol efflux pathways and other potential mechanisms involved in the athero-protective effect of high density lipoproteins. *Journal of Internal Medicine* 263, 256–273
10. Nakashima, Y., Plump, A. S., Raines, E. W., Breslow, J. L., and Ross, R. (1994) ApoE-deficient mice develop lesions of all phases of atherosclerosis throughout the arterial tree. *Arteriosclerosis, Thrombosis, and Vascular Biology* 14, 133–140

11. Shimano, H., Ohsuga, J., Shimada, M., Namba, Y., Gotoda, T., Harada, K., Katsuki, M., Yazaki, Y., and Yamada, N. (1995) Inhibition of diet-induced atheroma formation in transgenic mice expressing apolipoprotein E in the arterial wall. *Journal of Clinical Investigation* 95, 469
12. Huang, Y. (2010) A $\beta$ -independent roles of apolipoprotein E4 in the pathogenesis of Alzheimer's disease. *Trends in Molecular Medicine* 16, 287–294
13. Holtzman, D. M., Herz, J., and Bu, G. (2012) Apolipoprotein E and apolipoprotein E receptors: normal biology and roles in alzheimer disease. *Cold Spring Harbor Perspectives in Medicine* 2, a006312–a006312
14. Breslow, J. L., McPherson, J., Nussbaum, A. L., Williams, H. W., Lofquist-Kahl, F., Karathanasis, S. K., and Zannis, V. I. (1982) Identification and DNA sequence of a human apolipoprotein E cDNA clone. *Journal of Biological Chemistry* 257, 14639–14641
15. Wernet-Hammond, M. E., Lauer, S. J., Corsini, A., Walker, D., Taylor, J. M., and Rall, S. C. (1989) Glycosylation of human apolipoprotein E. The carbohydrate attachment site is threonine 194. *Journal of Biological Chemistry* 264, 9094–9101
16. Wetterau, J. R., Aggerbeck, L. P., Rall, S. C., and Weisgraber, K. H. (1988) Human apolipoprotein E3 in aqueous solution. I. Evidence for two structural domains. *Journal of Biological Chemistry* 263, 6240–6248
17. Innerarity, T., Friedlander, E. J., Rall, S. C., Weisgraber, K. H., and Mahley, R. W. (1983) The receptor-binding domain of human apolipoprotein E binding of apolipoprotein E fragments. *Journal of Biological Chemistry* 258, 12341–12347
18. Westerlund, J. A., and Weisgraber, K. H. (1993) Discrete carboxyl-terminal segments of apolipoprotein E mediate lipoprotein association and protein oligomerization. *Journal of Biological Chemistry* 268, 15745–15750
19. Morrow, J. A., Segall, M. L., Lund-Katz, S., Phillips, M. C., Knapp, M., Rupp, B., and Weisgraber, K. H. (2000) Differences in stability among the human apolipoprotein E isoforms determined by the amino-terminal domain. *Biochemistry* 39, 11657–11666
20. Segelke, B. W., Forstner, M., Knapp, M., Trakhanov, S. D., Parkin, S., Newhouse, Y. M., Bellamy, H. D., Weisgraber, K. H., and Rupp, B. (2000) Conformational flexibility in the apolipoprotein E amino-terminal domain structure determined from three new crystal forms: Implications for lipid binding. *Protein Science* 9, 886–897

21. Morrow, J. A., Segall, M. L., Lund-Katz, S., Phillips, M. C., Knapp, M., Rupp, B., and Weisgraber, K. H. (2000) Differences in stability among the human apolipoprotein E isoforms determined by the amino-terminal domain. *Biochemistry* 39, 11657–11666
22. Wilson, C., Wardell, M., Weisgraber, K. H., Mahley, R., and Agard, D. (1991) Three-dimensional structure of the LDL receptor-binding domain of human apolipoprotein E. *Science* 252, 1817–1822
23. Barbier, A., Clément-Collin, V., Dergunov, A. D., Visvikis, A., Siest, G., and Aggerbeck, L. P. (2006) The structure of human apolipoprotein E2, E3 and E4 in solution. *Biophysical Chemistry* 119, 158–169
24. Chen, J., Li, Q., and Wang, J. (2011) Topology of human apolipoprotein E3 uniquely regulates its diverse biological functions. *Proceedings of the National Academy of Sciences* 108, 14813–14818
25. Nguyen, D., Dhanasekaran, P., Phillips, M. C., and Lund-Katz, S. (2009) Molecular mechanism of apolipoprotein E binding to lipoprotein particles. *Biochemistry* 48, 3025–3032
26. Weers, P. M. M., Abdullahi, W. E., Cabrera, J. M., and Hsu, T.-C. (2005) Role of buried polar residues in helix bundle stability and lipid binding of apolipoprotein III: destabilization by threonine 31. *Biochemistry* 44, 8810–8816
27. Narayanaswami, V., Kiss, R. S., and Weers, P. M. M. (2010) The helix bundle: a reversible lipid binding motif. *Comparative Biochemistry and Physiology-Part A: Molecular & Integrative Physiology* 155, 123–133
28. Weers, P. M. M., Abdullahi, W. E., Cabrera, J. M., and Hsu, T.-C. (2005) Role of buried polar residues in helix bundle stability and lipid binding of apolipoprotein III: destabilization by threonine 31. *Biochemistry* 44, 8810–8816
29. Shinji Yokohama, Yoshiko Kawai, Shoji Tajima, and Akira Yamamoto (1985) Behavior of human apolipoprotein E in aqueous solutions and at interfaces. *The Journal of Biological Chemistry* 260, 16375–16382
30. Patel, A. B., Khumsupan, P., and Narayanaswami, V. (2010) Pyrene fluorescence analysis offers new insights into the conformation of the lipoprotein-binding domain of human apolipoprotein E. *Biochemistry* 49, 1766–1775
31. Fan, D., Li, Q., Korando, L., Jerome, W. G., and Wang, J. (2004) A monomeric human apolipoprotein E carboxyl-terminal domain. *Biochemistry* 43, 5055–5064

32. Patel, A. B., Khumsupan, P., and Narayanaswami, V. (2010) Pyrene fluorescence analysis offers new insights into the conformation of the lipoprotein-binding domain of human apolipoprotein E. *Biochemistry* 49, 1766–1775
33. Zannis, V. I., Just, P. W., and Breslow, J. L. (1981) Human apolipoprotein E isoprotein subclasses are genetically determined. *American Journal of Human Genetics* 33, 11–24
34. Zannis, V. I., Breslow, J. L., SanGiacomo, T. R., Aden, D. P., and Knowles, B. B. (1981) Characterization of the major apolipoproteins secreted by two human hepatoma cell lines. *Biochemistry* 20, 7089–7096
35. Dong, L.-M., and Weisgraber, K. H. (1996) Human apolipoprotein E4 domain interaction. *Journal of Biological Chemistry* 271, 19053–19057
36. Hùgh, P., Oturai, A., Schreiber, K., Blinkenberg, M., Jùrgensen, O. S., Ryder, L., Paulson, O. B., Sùrensen, P. S., and Knudsen, G. M. (2000) Apolipoprotein E and multiple sclerosis: impact of the epsilon-4 allele on susceptibility, clinical type and progression rate. *Multiple Sclerosis* 6, 226–230
37. Hatters, D. M., Peters-Libeu, C. A., and Weisgraber, K. H. (2006) Apolipoprotein E structure: insights into function. *Trends in Biochemical Sciences* 31, 445–454
38. Pietrzik, C. U., and Jaeger, S. (2008) Functional role of lipoprotein receptors in alzheimers disease. *Current Alzheimer Research* 5, 15–25
39. Breslow, J. L., Zannis, V. I., SanGiacomo, T. R., Third, J. L., Tracy, T., and Glueck, C. J. (1982) Studies of familial type III hyperlipoproteinemia using as a genetic marker the apoE phenotype E2/2. *Journal of Lipid Research* 23, 1224–1235
40. Dong, L.-M., and Weisgraber, K. H. (1996) Human apolipoprotein E4 domain interaction Arginine 61 and glutamic acid 255 interact to direct the preference for very low density lipoproteins. *Journal of Biological Chemistry* 271, 19053–19057
41. Dong, J., Peters-Libeu, C. A., Weisgraber, K. H., Segelke, B. W., Rupp, B., Capila, I., Hernáiz, M. J., LeBrun, L. A., and Linhardt, R. J. (2001) Interaction of the N-terminal domain of apolipoprotein E4 with heparin. *Biochemistry* 40, 2826–2834
42. Hauser, P. S., Narayanaswami, V., and Ryan, R. O. (2011) Apolipoprotein E: from lipid transport to neurobiology. *Progress in Lipid Research* 50, 62–74
43. Sakamoto, T., Tanaka, M., Vedhachalam, C., Nickel, M., Nguyen, D., Dhanasekaran, P., Phillips, M. C., Lund-Katz, S., and Saito, H. (2008) Contributions of the carboxyl-terminal helical segment to the self-association and lipoprotein

- preferences of human apolipoprotein E3 and E4 isoforms. *Biochemistry* 47, 2968–2977
44. Elena Posse de Chaves, and Vasanthy Narayanaswami (2008) Apolipoprotein E and cholesterol and disease in the brain. *Future Lipidology* 3, 505–530
  45. Wilson, C., Wardell, M., Weisgraber, K.H., Mahley, R., Agard, D. (1991) Three-dimensional structure of the LDL receptor-binding domain of human apolipoprotein E. *Science* 252, 1817-1822
  46. Wardell, M. R., Rall, S. C., Schaefer, E. J., Kane, J. P., and Weisgraber, K. H. (1991) Two apolipoprotein E5 variants illustrate the importance of the position of additional positive charge on receptor-binding activity. *Journal of Lipid Research* 32, 521–528
  47. Sivashanmugam, A., and Wang, J. (2009) A unified scheme for initiation and conformational adaptation of human apolipoprotein E N-terminal domain upon lipoprotein binding and for receptor binding activity. *Journal of Biological Chemistry* 284, 14657–14666
  48. Chou, C.-Y., Lin, Y.L., Huang, Y.C., Sheu, S.Y., Lin, T.-H., Tsay, H.J., Chang, G.G., and Shiao, M.S. (2005) Structural variation in human apolipoprotein E3 and E4: secondary structure, tertiary structure, and size distribution. *Biophysical Journal* 88, 455–466
  49. Fan, D., Li, Q., Korando, L., Jerome, W. G., and Wang, J. (2004) A monomeric human apolipoprotein E carboxyl-terminal domain. *Biochemistry* 43, 5055–5064
  50. Zhang, Y., Vasudevan, S., Sojitrawala, R., Zhao, W., Cui, C., Xu, C., Fan, D., Newhouse, Y., Balestra, R., Jerome, W. G., Weisgraber, K., Li, Q., and Wang, J. (2007) A monomeric, biologically active, full-length human apolipoprotein E. *Biochemistry* 46, 10722–10732
  51. Huang, R. Y. C., Garai, K., Frieden, C., and Gross, M. L. (2011) Hydrogen/deuterium exchange and electron-transfer dissociation mass spectrometry determine the interface and dynamics of apolipoprotein E oligomerization. *Biochemistry* 50, 9273–9282
  52. Nguyen, D., Dhanasekaran, P., Phillips, M. C., and Lund-Katz, S. (2009) Molecular mechanism of apolipoprotein E binding to lipoprotein particles. *Biochemistry* 48, 3025–3032

53. Miyazaki, M., Tajima, Y., Ishihama, Y., Handa, T., and Nakano, M. (2013) Effect of phospholipid composition on discoidal HDL formation. *Biochimica et Biophysica Acta (BBA) Biomembranes* 1828, 1340–1346
54. Drury, J., and Narayanaswami, V. (2005) Examination of lipid-bound conformation of apolipoprotein E4 by pyrene excimer fluorescence. *Journal of Biological Chemistry* 280, 14605–14610
55. Peters-Libeu, C. A., Newhouse, Y., Hatters, D. M., and Weisgraber, K. H. (2006) Model of biologically active apolipoprotein E bound to dipalmitoylphosphatidylcholine. *Journal of Biological Chemistry* 281, 1073–1079
56. Tran, T. N., Kim, S. H., Gallo, C., Amaya, M., Kyees, J., and Narayanaswami, V. (2013) Biochemical and biophysical characterization of recombinant rat apolipoprotein E: Similarities to human apolipoprotein E3. *Archives of Biochemistry and Biophysics* 529, 18–25
57. Khumsupan, P., Ramirez, R., Khumsupan, D., and Narayanaswami, V. (2011) Apolipoprotein E LDL receptor-binding domain-containing high-density lipoprotein: A nanovehicle to transport curcumin, an antioxidant and anti-amyloid bioflavonoid. *Biochimica et Biophysica Acta (BBA)-Biomembranes* 1808, 352–359
58. Hatters, D. M., Voss, J. C., Budamagunta, M. S., Newhouse, Y. N., and Weisgraber, K. H. (2009) Insight on the molecular envelope of lipid-bound apolipoprotein E from electron paramagnetic resonance spectroscopy. *Journal of Molecular Biology* 386, 261–271
59. Schneeweis, L. A., Koppaka, V., Lund-Katz, S., Phillips, M. C., and Axelsen, P. H. (2005) Structural analysis of lipoprotein E particles. *Biochemistry* 44, 12525–12534
60. Fisher, C. A., and Ryan, R. O. (1999) Lipid binding-induced conformational changes in the N-terminal domain of human apolipoprotein E. *Journal of Lipid Research* 40, 93–99
61. Raussens, V., Fisher, C. A., Goormaghtigh, E., Ryan, R. O., and Ruyschaert, J.-M. (1998) The low density lipoprotein receptor active conformation of apolipoprotein E helix organization in n-terminal domain-phospholipid disc particles. *Journal of Biological Chemistry* 273, 25825–25830
62. Lu, B., Morrow, J. A., and Weisgraber, K. H. (2000) Conformational reorganization of the four-helix bundle of human apolipoprotein E in binding to phospholipid. *Journal of Biological Chemistry* 275, 20775–20781

63. Narayanaswami, V., Kay, C. M., Oikawa, K., and Ryan, R. O. (1994) Structural and binding characteristics of the carboxyl terminal fragment of apolipoprotein III from *Manduca sexta*. *Biochemistry* 33, 13312–13320
64. Soulages, J. L., and Arrese, E. L. (2000) Dynamics and hydration of the helices of apolipoprotein III. *Journal of Biological Chemistry* 275, 17501–17509
65. Bains, G. K., Kim, S. H., Sorin, E. J., and Narayanaswami, V. (2012) The extent of pyrene excimer fluorescence emission is a reflector of distance and flexibility: analysis of the segment linking the LDL receptor-binding and tetramerization domains of apolipoprotein E3. *Biochemistry* 51, 6207–6219
66. Johnson, I., and Spence, M.T.Z. (eds.). (2010). Chapter 2 Thiol-Reactive Probes. In *The Molecular Probes Handbook*, 11<sup>th</sup> <http://www.lifetechnologies.com/content/dam/LifeTech/global/technical-reference-library/Molecular%20Probes%20Handbook/chapter-pdfs/Ch-2-Thiol-Reactive-Probes.pdf?icid=WE216841>.
67. Vos, W. L., Schor, M., Baumgaertner, A., Tieleman, D. P., and Hemminga, M. A. (2010) Molecular dynamics simulations reveal that AEDANS is an inert fluorescent probe for the study of membrane proteins. *European Biophysics Journal* 39, 229–239
68. Mizuguchi, C., Hata, M., Dhanasekaran, P., Nickel, M., Phillips, M. C., Lund-Katz, S., and Saito, H. (2012) Fluorescence analysis of the lipid binding-induced conformational change of apolipoprotein E4. *Biochemistry* 51, 5580–5588
69. Mocz, G. (2006) Information content of fluorescence polarization and anisotropy. *Journal of Fluorescence* 16, 511–524
70. Perrin, F. (1926) Polarisation de la lumière de fluorescence. Vie moyenne des molécules dans l'état excité. *Journal of Physics Radium* 7, 390–401
71. Taraska, J. W., and Zagotta, W. N. (2010) Fluorescence applications in molecular neurobiology. *Neuron* 66, 170–189
72. Hubbell, W. L., Cafiso, D. S., and Altenbach, C. Identifying conformational changes with site-directed spin labeling. *Nature Structural Biology* 7, 735–739
73. Katta, V., and Chait, B. T. (1993) Hydrogen/deuterium exchange electrospray ionization mass spectrometry: a method for probing protein conformational changes in solution. *Journal of the American Chemical Society* 115, 6317–6321

74. Yates, J. R., Ruse, C. I., and Nakorchevsky, A. (2009) Proteomics by mass spectrometry: approaches, advances, and applications. *Annual Review of Biomedical Engineering* 11, 49–79
75. Maier, C. S., and Deinzer, M. L. (2005) Protein conformations, interactions, and H/D exchange. *Methods in Enzymology*.  
<http://linkinghub.elsevier.com/retrieve/pii/S0076687905020100>
76. Nirudodhi, S., Parsonage, D., Karplus, P. A., Poole, L. B., and Maier, C. S. (2011) Conformational studies of the robust 2-Cys peroxiredoxin Salmonella typhimurium AhpC by solution phase hydrogen/deuterium (H/D) exchange monitored by electrospray ionization mass spectrometry. *International Journal of Mass Spectrometry* 302, 93–100
77. Bai, Y., Milne, J. S., Mayne, L., and Englander, S. W. (1993) Primary structure effects on peptide group hydrogen exchange. *Proteins: Structure, Function, and Genetics* 17, 75–86
78. Chetty, P. S., Mayne, L., Lund-Katz, S., Stranz, D., Englander, S. W., and Phillips, M. C. (2009) Helical structure and stability in human apolipoprotein AI by hydrogen exchange and mass spectrometry. *Proceedings of the National Academy of Sciences* 106, 19005–19010
79. Kavan, D., and Man, P. (2011) MSTools—Web based application for visualization and presentation of HXMS data. *International Journal of Mass Spectrometry* 302, 53–58
80. Choy, N., Raussens, V., and Narayanaswami, V. (2003) Inter-molecular coiled-coil formation in human apolipoprotein E C-terminal domain. *Journal of Molecular Biology* 334, 527–539
81. Gupta, V., Narayanaswami, V., Budamagunta, M. S., Yamamoto, T., Voss, J. C., and Ryan, R. O. (2006) Lipid-induced extension of apolipoprotein E helix 4 correlates with low density lipoprotein receptor binding ability. *Journal of Biological Chemistry* 281, 39294–39299
82. Garai, K., Baban, B., and Frieden, C. (2011) Dissociation of apolipoprotein E oligomers to monomer is required for high-affinity binding to phospholipid vesicles. *Biochemistry* 50, 2550–2558
83. Weinberg, R. B., and Spector, M. S. (1985) Structural properties and lipid binding of human apolipoprotein A-IV". *Journal of Biological Chemistry* 260, 4914–4921

84. Reynolds, J. A. (1976) Conformational stability of the polypeptide components of human high density serum lipoprotein. *Journal of Biological Chemistry* 251, 6013–6015
85. Reijngoud, D. J., and Phillips, M. C. (1982) Mechanism of dissociation of human apolipoprotein AI from complexes with dimyristoylphosphatidylcholine as studied by guanidine hydrochloride denaturation. *Biochemistry* 21, 2969–2976
86. Mantulin, W. W., Rohde, M. F., Gotto, A. M., and Pownall, H. J. (1980) The conformational properties of human plasma apolipoprotein C-II. *The Journal of Biological Chemistry* 256, 8185–8191
87. Ryan, R. O., Oikawa, K., and Kay, C. M. (1993) Conformational, thermodynamic, and stability properties of *Manduca sexta* apolipoprotein III. *Journal of Biological Chemistry* 268, 1525–1530
88. Dettloff, M., Weers, P. M. M., Niere, M., Kay, C. M., Ryan, R. O., and Wiesner, A. (2001) An N-terminal three-helix fragment of the exchangeable insect apolipoprotein apolipoprotein III Conserves the lipid binding properties of wild-type Protein. *Biochemistry* 40, 3150–3157
89. Narayanaswami, V., Yamauchi, Y., Weers, P. M., Maekawa, H., Sato, R., Tsuchida, K., Oikawa, K., Kay, C. M., and Ryan, R. O. (2000) Spectroscopic characterization of the conformational adaptability of *Bombyx mori* apolipoprotein III. *European Journal of Biochemistry* 267, 728–736
90. Weers, P. M. M., Narayanaswami, V., Kay, C. M., and Ryan, R. O. (1999) Interaction of an exchangeable apolipoprotein with phospholipid vesicles and lipoprotein particles: role of leucines 32, 34, and 95 in *Locusta migratoria* Apolipoprotein III. *Journal of Biological Chemistry* 274, 21804–21810
91. Narayanaswami, V., Szeto, S. S. W., and Ryan, R. O. (2001) Lipid association-induced N- and C-terminal domain reorganization in human apolipoprotein E3. *Journal of Biological Chemistry* 276, 37853–37860
92. Wang, S., Zhang, C., Nordeen, S. K., and Shapiro, D. J. (2006) In vitro fluorescence anisotropy analysis of the interaction of full-length SRC1a with estrogen receptors and beta supports an active displacement model for coregulator utilization. *Journal of Biological Chemistry* 282, 2765–2775
93. Zhang, Z., and Smith, D. L. (1993) Determination of amide hydrogen exchange by mass spectrometry: a new tool for protein structure elucidation. *Protein Science* 2, 522–531